Report
R-19-06
May 2019

Gas release from the BHK vault – Multiphase flow modelling of the near-field

Report for the safety evaluation SE-SFL

Orlando Silva

Emilie Coene

Jorge Molinero

Marcelo Laviña

Andrés Idiart

SVENSK KÄRNBRÄNSLEHANTERING AB

SWEDISH NUCLEAR FUEL
AND WASTE MANAGEMENT CO

Box 3091, SE-169 03 Solna
Phone +46 8 459 84 00
skb.se

SVENSK KÄRNBRÄNSLEHANTERING

ISSN 1402-3091
SKB R-19-06
ID 1587210
May 2019

Gas release from the BHK vault – Multiphase flow modelling of the near-field

Report for the safety evaluation SE-SFL

Orlando Silva, Emilie Coene, Jorge Molinero,
Marcelo Laviña, Andrés Idiart

Amphos 21 Consulting S. L.

Summary

The present report describes the modelling of immiscible two-phase flow to simulate gas released from waste in the repository for long lived low and intermediate level nuclear waste (SFL). The main gas generating process involves hydrogen formation by the anoxic corrosion of steel.

A 2D model has been set up, including a cross section of the vault for metallic waste (BHK) and its surroundings. The host rock has been represented using homogeneous hydraulic properties, including a deformation zone intersecting the BHK for some simulation cases.

Different groundwater flow cases have been simulated, including hydrostatic, horizontal and vertical downward flow conditions. The overpressures in BHK caused by gas generation are similar for all groundwater flow scenarios, ranging from 1.5 to 2.5 bars. Gas generation does not significantly alter the groundwater flow or saturation conditions in the repository near-field. Nor does it influence the hydraulic behavior of the concrete barriers in BHK.

Sammanfattning

I denna rapport beskrivs modelleringen av icke-blandbart tvåfasflöde som simulerar utsläpp av gas från avfall i förvaret för långlivat låg- och medelaktivt avfall (SFL). Vätebildning genom anoxisk korrosion av stål är den huvudsakliga gasbildningsprocessen. En 2D-modell har utvecklats som inkluderar ett tvärsnitt av bergssalen för metalliskt avfall (BHK) och dess omgivande berggrund. Berget har representerats med homogena hydrauliska egenskaper, inklusive en deformationszon som i vissa simuleringsfall skär genom BHK.

Olika fall av grundvattenflöden har simulerats, inklusive hydrostatiska, horisontella och vertikalt nedåtgående flödesförhållanden. Övertrycket i BHK till följd av gasbildning är liknande för alla grundvattenflödesscenarier, från 1,5 till 2,5 bar. Gasbildning ger ingen signifikant förändring av grundvattenflödet eller mättnadsförhållandena i förvarets närområde. Den påverkar inte heller de hydrauliska egenskaperna hos betongbarriärerna i BHK.

Nomenclature

Alphanumeric

a	EOS parameter (Pa m^6/mol^2)
$\mathbf{a}$	absorption coefficient in the coefficient form of the PDE module of COMSOL
A	total surface area of steel in the waste (m^2); parameter in viscosity correlation (dimensionless)
b	EOS parameter (m^3/mol); Biot's coefficient (dimensionless)
c	concentration of a component/species (kg/m^3)
$\mathbf{c}$	diffusion coefficient in the coefficient form of the PDE module of COMSOL
C	concentration of a component/species (kg/m^3)
$\mathbf{d}$	damping coefficient in the coefficient form of the PDE module of COMSOL
$\mathbf{D}$	diffusion-dispersion tensor of a component in a phase (m^2/s)
$\mathbf{e}$	mass coefficient in the coefficient form of the PDE module of COMSOL
$\mathbf{f}$	source term in the coefficient form of the PDE module of COMSOL
g	gravity acceleration, 9.8 m/s^2
G	parameter in viscosity correlation (dimensionless)
$\mathbf{I}$	second order identity tensor (dimensionless)
$\mathbf{J}$	diffusive-dispersive mass flux vector of a component in a phase (kg/m^2 s)
k	intrinsic permeability of the rock (m^2)
$\mathbf{k}$	intrinsic permeability tensor (m^2)
K	bulk modulus (MPa)
m	van Genuchten parameter (dimensionless)
M	molecular weight of a component/species (kg/mol); mass of steel (kg)
n	van Genuchten parameter (dimensionless)
$\mathbf{n}$	unit vector normal to surface Σ
N	interface mass flux of a component between two phases (kg/m^2 s); number of components
P	pressure (Pa)
ΔP	overpressure (Pa)
q	constant water flux (m/s)
$\mathbf{q}$	specific discharge of a phase (m/s)
Q	mass sink/source term of a component in a phase (kg/m^3 s); inflow/outflow rates of gas and water from the BHK vault (m^3/year)
r	hydrogen generation rate (kg/m^3 s); steel corrosion rate (μm/year)
$\hat{r}$	molar hydrogen generation rate (mol/m^3 s)
R	universal gas constant, 8.13144621 J/mol K
S	saturation of a phase (dimensionless); surface area (m^2)
t	time (s)
T	temperature (K); transmissivity (m^2/s)
u	displacement (m)
$\mathbf{u}$	vector of unknowns in the coefficient form of the PDE module of COMSOL
V	volume (m^3)
w	iron content in the steel (dimensionless)
x, y, z	spatial coordinates (m)
Y	molar volume ratio (dimensionless)
$\mathbf{z}$	vertical position vector (dimensionless)

Greek letters

α	mass transfer coefficient (m/Pa s)
$\boldsymbol{\alpha}$	conservative flux convection coefficient in the coefficient form of the PDE module of COMSOL
$\boldsymbol{\beta}$	convection coefficient in the coefficient form of the PDE module of COMSOL
χ	EOS parameter (dimensionless)
ϕ	porosity (m^3/m^3)
$\boldsymbol{\gamma}$	conservative flux source term in the coefficient form of the PDE module of COMSOL
Γ	boundary
λ	mobility of a phase (m s/kg)
μ	dynamic viscosity of a phase (kg/m s)
v	molar volume of the gas phase (m^3/mol)
ρ	density of a phase (kg/m^3)
Σ	surface of the BHK vault or the waste compartment
θ	volumetric content of a phase (m^3/m^3)
ω	acentric factor of a component (dimensionless)
σ	principal stress (MPa)
$\boldsymbol{\sigma}$	total or effective stress tensor (MPa)
Ω	sub-domain
ξ	EOS parameter (dimensionless)

Sub- and superscripts

a	mass and damping coefficients in the coefficient form of the PDE module of COMSOL
atm	atmospheric conditions
bottom	bottom boundary
c	capillary pressure
corr	corrosion
crit	critical property
e	effective
ext	external value of a state variable or coordinate
frac	fracture
β, *i, j*	phases β, *i* and *j*
ini	initial
H2(*g*)	hydrogen gas
k	k^{th} component
l, *g*, *s*	liquid, gaseous and solid phases
left	left boundary
p	pressure; pore
r	relative; residual
rock	rock
s	saturation
S	solid
T	skeleton
RT90	reference system
w	water
waste	waste compartment

0	reference coordinates used by Vidstrand and Rhén (2011) and Joyce et al. (2019); initial
1	principal stress
*	reduced property
′	effective stress

Acronyms/abbreviations

BDF	backward differentiation formula
BHA	vault for legacy waste
BHK	vault for metallic waste
ECPM	equivalent continuous porous medium
EOS	equation of state
MDN	minor deformation zone
MUMPS	multifrontal massively parallel sparse direct solver
PARDISO	parallel direct sparse solver
PDE	partial differential equation
SFL	repository for long lived low and intermediate level nuclear waste

Contents

1 Introduction

SKB plans to dispose of long-lived low and intermediate level nuclear waste in SFL. The waste comprises waste from the operation and decommissioning of the Swedish nuclear power plants, legacy waste from the early research in the Swedish nuclear programs, and smaller amounts of waste from hospitals, industry and research. The long-lived low and intermediate level waste from the nuclear power plants consists of neutron-irradiated components and control rods. The total quantity of long-lived waste planned for SFL is estimated to approximately 16000 m^3, of which about one third originates from the nuclear power plants. The remainder comes from AB SVAFO and Studsvik Nuclear AB, who manage the legacy waste and the waste from hospitals, industry and research.

In the proposed concept (Elfwing et al. 2013), SFL is a deep geological repository with two storage vaults:

- One vault for the metallic waste from the nuclear power plants.
- One vault for legacy waste from AB SVAFO and Studsvik Nuclear AB.

The vault for the metallic waste (BHK) is designed with a concrete barrier. The waste is segmented, after which the parts are deposited in steel tanks and stabilized with grout. The steel tanks are emplaced in the repository. This section of the repository is backfilled with concrete, which acts as a barrier against groundwater flow and contributes to a low diffusion rate and high sorption of many radionuclides. The concrete in the barrier will create an alkaline environment in the repository section, reducing the corrosion rate of the steel and thus limiting the release rate of radionuclides.

The vault for the legacy waste (BHA) from AB SVAFO and Studsvik Nuclear AB is designed with a bentonite barrier. The waste is deposited in containers designed for SFL and stabilized with grout. These containers are emplaced in the repository. The section is backfilled with bentonite. The bentonite acts as a barrier by limiting the groundwater flow, thereby making diffusion the dominant transport mechanism for radionuclides through the bentonite. Bentonite clay also has the ability to efficiently filter colloids (Elfwing et al. 2013).

Figure 1-1 shows a schematic representation of the repository design, with the BHA vault in the foreground and the BHK vault in the background.

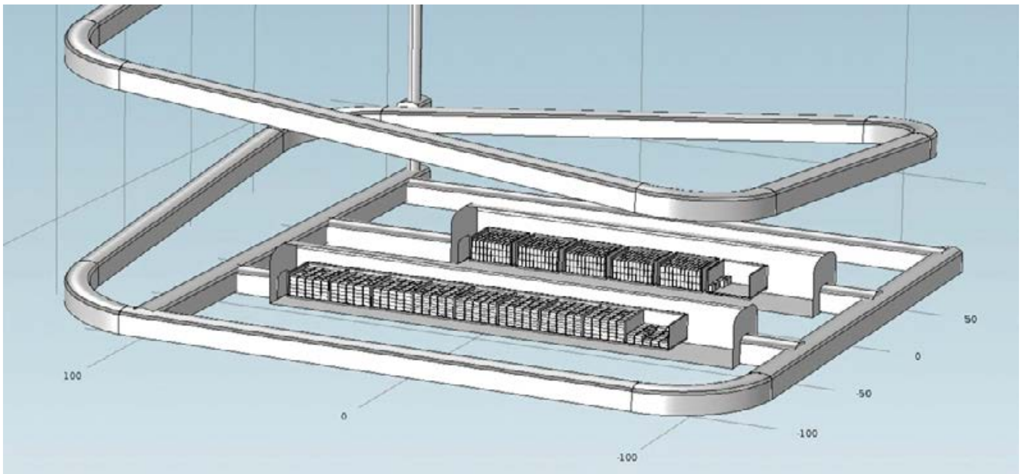

Figure 1-1. *SFL repository design with BHA vault (front) and BHK vault (back) (Abarca et al. 2019).*

With groundwater saturation of the repository, the anoxic corrosion of steel will produce hydrogen gas. This can have important implications on the repository system and the analysis of long term safety. Gas production may

- cause pressure build up potentially harmful to engineered barriers,
- affect the saturation level of the repository system,
- affect the groundwater flow in the vicinity of the repository.

The main concern of the present work is to analyze these issues for the BHK by means of multiphase flow modelling.

1.1 Objectives

The main objective of the presented work is to develop a conceptual model for immiscible two-phase flow of water and hydrogen in porous media, and to implement the corresponding numerical model. The model has been used to simulate hydrogen gas release and migration from the BHK vault, addressing the following topics:

- Pressure build-up in the concrete barrier.
- Saturation level in BHK over time and the effect on the hydraulic behavior of the concrete barriers.
- Influence on groundwater flow in the near-field.
- Effect of deformation zones on gas release and migration.

1.2 Overview of calculation cases

This work studies the effect of different factors on the gas release from BHK and subsequent gas migration through the host rock using a set of 21 simulation cases. Table 1-1 summarizes the main features of each simulation case. The motivation for each of these cases is explained below.

In the first case the system is simplified by assuming hydrostatic conditions and the same water retention curves for the waste compartment and the backfill (see fourth column of Table 1-1). The term *water retention* refers to the retention of water into a porous medium due to capillarity. Also, the host rock is considered homogeneous. Case 2 is a variation of Case 1, in which the water retention curves of the waste and the backfill are different. A comparison of Cases 1 and 2 illustrated the impact of capillarity on gas release from BHK. In addition, Cases 1 and 2 are considered as base cases for the sake of comparison with remaining cases.

The direction of the groundwater flow in the near-field can affect the gas release from the BHK vault and the gas migration through the rock. Vertical downwards water flow may act as a barrier for gas release, leading to an increase of internal pressures in the BHK vault. In contrast, horizontal groundwater flow can help to decrease the overpressures by carrying gas away from the vault. For these reasons, different cases of horizontal and vertical downwards groundwater flow were simulated considering the host rock as a homogeneous medium:

- Cases 3, 4 and 5 address horizontal water flow with the same water retention curves for the waste and backfill.
- Cases 6, 7 and 8 address horizontal water flow with different water retention curves for the waste and backfill.
- Cases 9, 10 and 11 address vertical downward water flow with the same water retention curves for the waste and backfill.
- Cases 12, 13 and 14 address vertical downward water flow with different water retention curves for the waste and backfill.

Table 1-1. Summary of simulation cases to study hydrogen generation in the BHK vault.

Case #	Rock	Groundwater flow conditions	Waste and backfill water retention curves*	Groundwater flux*, m^3/m^2 s	Fracture zone permeability, m^2
1	Homogeneous	Hydrostatic	Same**	-	-
2			Different**		
3		Low horizontal flow	Same	2.33×10^{-10}	
4		Medium horizontal flow		1.89×10^{-8}	
5		High horizontal flow		5.00×10^{-8}	
6		Low horizontal flow	Different	2.33×10^{-10}	
7		Medium horizontal flow		1.89×10^{-8}	
8		High horizontal flow		5.00×10^{-8}	
9		Low vertical*** flow	Same	2.33×10^{-10}	
10		Medium vertical flow		1.89×10^{-8}	
11		High vertical flow		5.00×10^{-8}	
12		Low vertical flow	Different	2.33×10^{-10}	
13		Medium vertical flow		1.89×10^{-8}	
14		High vertical flow		5.00×10^{-8}	
15	Including a fracture zone	Hydrostatic	Different	-	8.00×10^{-15}
16					5.00×10^{-14}
17					1.00×10^{-13}
18					9.08×10^{-13}
19					3.07×10^{-12}
20					6.18×10^{-12}
21					2.5×10^{-11}

* Porosity and water retention curve parameters of the rock and vault materials are given in Table 2-2.

** "Same" and "different" mean that the water retention curves of the waste and backfill are assumed to be the same and different, respectively.

*** Groundwater vertical flow is downwards in cases 9 to 14.

In addition, gas flow behavior also depends on the magnitude of the groundwater flux. According to the regional hydrology model (Joyce et al. 2019), it was determined that the magnitude of the water flux ranges from 5.02×10^{-18} to 1.89×10^{-8} m/s (see Section 4.1 and Table 4-1). Moreover, the model was found to be insensitive to water flow rates lower than 2.33×10^{-10} m/s. For each flow orientation and combination of water retention curves, 3 cases were simulated to quantify the effect of the water flux magnitude on gas flow. These cases are labelled in Table 1-1 as "low flow" (2.33×10^{-10} m/s), "medium flow" (1.89×10^{-8} m/s) and "high flow" (5.00×10^{-8} m/s). The comparison of the different cases shown in Table 1-1 serves to assess the relative importance of capillarity and buoyancy on gas flow.

Previous studies on the hydrogeology in the Laxemar area (Vidstrand et al. 2010, Abarca et al. 2019) revealed the presence of zones with high hydraulic conductivity. These deformation or fracture zones could constitute a preferential pathway, affecting the gas release from the BHK vault and its migration through the rock. To address this issue, a model was used that includes a fracture zone in the host rock. This model assumed hydrostatic initial conditions and different water retention curves for the waste and backfill. Cases 15 to 21 aim to evaluate the effect of varying fracture zone permeability on gas release. The fracture zone permeabilities presented in Table 1-1 were defined consistently with transmissivity measurements of minor deformation zones in Laxemar, as compiled by Rhén et al. (2008). These simulation cases were compared with the base Case 2 (homogeneous host rock).

1.3 Outline of the report

Chapter 2 describes first the governing equations and constitutive relationships considered in the model. Then, the geometry, boundary conditions, hydraulic and transport properties considered in the cases of homogeneous rock and host-rock with a fracture zone are described. The calculation of hydrogen generation rates is also explained.

Chapter 3 details the numerical implementation of the model in Comsol Multiphysics 5.2a. The spatial discretization, time stepping, and the solvers used in the homogeneous rock case and the case of a rock including a fracture are described.

Chapter 4 analyses the computed results. First, the results obtained with a homogeneous host rock are described. Fourteen cases were simulated to study the role of the water retention curve, the direction of the groundwater flow and the groundwater flow rate on gas migration. Then, the results of the rock including a fracture zone are compared to the case of homogeneous rock. Seven cases were simulated to evaluate the impact of the fracture zone permeability on gas release.

Chapter 5 summarizes the main results and conclusions of the work.

2 Model description

This chapter presents the governing equations for immiscible two-phase flow in porous media, used to model gas generation and migration in BHK. The mathematical approach is based on solving for the flow equation of the non-wetting phase and for the equation obtained by summing the flow equations of wetting and non-wetting phases. For immiscible two-phase flow, dissolution, evaporation and volatilization processes are not considered in the governing equations. Under the repository conditions (e.g., 50 bar and 15 °C), hydrogen solubility in water is about 0.06% w/w (Sander 2015). Neglecting gas dissolution in water is therefore a reasonable approximation in the present work. Moreover, hydrogen dissolution has a small effect on the water density and causes gas pressures to be lower than if miscibility is disregarded. Neglecting gas miscibility is thus a cautious assumption when investigating pressure build-up in BHK.

The geometry and parameterization of the system is also explained. This includes the estimation of hydrogen generation rates and the hydraulic and transport properties of the BHK vault and the surrounding rock in the SFL repository.

2.1 Immiscible two-phase flow: pressure-saturation approach

2.1.1 Governing equations

A multiphase system consisting of liquid (*l*), gas (*g*) and solid (*s*) phases is considered. Components that may be present within these phases are water and $N-1$ compounds. Under isothermal conditions, the mass conservation equations for a component *k*, present in the different phases, are given by (Silva and Grifoll 2007a)

$$\frac{\partial \phi S_l C_l^k}{\partial t} = -\nabla \cdot \left(\mathbf{J}_l^k + \mathbf{q}_l C_l^k\right) + a_{lg}^k N_{lg}^k - a_{ls}^k N_{ls}^k + Q_l^k \tag{2-1a}$$

$$\frac{\partial \phi S_g C_g^k}{\partial t} = -\nabla \cdot \left(\mathbf{J}_g^k + \mathbf{q}_g C_g^k\right) - a_{lg}^k N_{lg}^k - a_{gs}^k N_{gs}^k + Q_g^k \tag{2-1b}$$

$$\frac{\partial \theta_s C_s^k}{\partial t} = a_{gs}^k N_{gs}^k + a_{ls}^k N_{ls}^k \tag{2-1c}$$

Above, C_i^k (kg/m^3) is the concentration of component *k* in the phase *i* ($i = l, g, s$), S_i the saturation of phase *i*, ϕ (m^3/m^3) the soil porosity, θ_s (m^3/m^3) the volumetric fraction of the solid phase, $\mathbf{q}_i$ (m/s) the phase specific discharge or Darcy flux, Q_i^k (kg/m^3 s) a mass sink/source term of component *k* in the phase *i* (sinks are assigned with negative values of Q_i^k while the sources are positive), N_{ij}^k (kg/m^2 s) the interface mass flux of component *k* from phase *i* to phase *j*, and a_{ij}^k (m^2/m^3) the interfacial area between phases *i* and *j* by unit volume of porous matrix.

The diffusive-dispersive mass flux vector $\mathbf{J}_i^k$ (kg/m^2 s) is given by

$$\mathbf{J}_i^k = -\phi S_i \mathbf{D}_i^k \nabla C_i^k \tag{2-2}$$

where $\mathbf{D}_i^k$ (m^2/s) is the diffusion-dispersion tensor of component *k* in phase *i* (Bear and Bachmat 1990). Note that $S_i = \theta_i/\phi$, where θ_i is the volumetric content of phase *i*. The sum of the fluid phase saturations is equal to one, and the sum of all volumetric contents is equal to one as well. Therefore

$$S_l + S_g = 1 \tag{2-3a}$$

$$\theta_s = 1 - \phi \tag{2-3b}$$

The specific discharge of phase *i* ($\mathbf{q}_i$) (m/s) is given by the generalized Darcy's law (Bear and Bachmat 1990)

$$\mathbf{q}_i = -\mathbf{k}\lambda_i\left(\nabla P_i + \rho_i g \mathbf{z}\right) \tag{2-4a}$$

$$\lambda_i = \frac{k_{ri}}{\mu_i} \tag{2-4b}$$

In Equation (2-4), $\mathbf{k}$ (m^2) is the intrinsic permeability tensor of the soil, $g\mathbf{z}$ (m/s^2) the gravity vector, λ_i (m s/kg) the mobility, k_{ri} (dimensionless) the relative permeability, ρ_i (kg/m^3) the density, μ_i (kg/m s) the dynamic viscosity, and P_i (Pa) the pressure of phase i.

Equations (2-1a), (2-1b) and (2-1c) can be added by phases to give

$$\frac{\partial(\phi S_l \rho_l)}{\partial t} = -\nabla \cdot \left(\sum_{k=1}^{N} \mathbf{J}_l^k + \rho_l \mathbf{q}_l \right) + \sum_{k=1}^{N} a_{lg}^k N_{lg}^k - \sum_{k=1}^{N} a_{ls}^k N_{ls}^k + \sum_{k=1}^{N} Q_l^k \tag{2-5a}$$

$$\frac{\partial(\phi S_g \rho_g)}{\partial t} = -\nabla \cdot \left(\sum_{k=1}^{N} \mathbf{J}_g^k + \rho_g \mathbf{q}_g \right) - \sum_{k=1}^{N} a_{\mathrm{lg}}^k N_{lg}^k - \sum_{k=1}^{N} a_{gs}^k N_{gs}^k + \sum_{k=1}^{N} Q_g^k \tag{2-5b}$$

$$\frac{\partial\left(\theta_s \sum_{k=1}^{N} C_s^k \right)}{\partial t} = \sum_{k=1}^{N} a_{gs}^k N_{gs}^k + \sum_{k=1}^{N} a_{ls}^k N_{ls}^k \tag{2-5c}$$

Under equimolar flow conditions in the gas phase and the liquid phase, $\sum_{k=1}^{N} \mathbf{J}_g^k = \mathbf{0}$ and $\sum_{k=1}^{N} \mathbf{J}_l^k = \mathbf{0}$, respectively. Here, the adsorption onto the solid and the miscibility are neglected, so that $a_{is}^k N_{is}^k = 0$ and $a_{lg}^k N_{lg}^k = 0$. Thus, Equations (2-5a) and (2-5b) reduce to

$$\frac{\partial(\phi S_l \rho_l)}{\partial t} + \nabla \cdot (\rho_l \mathbf{q}_l) = \sum_{k=1}^{N} Q_l^k \tag{2-6a}$$

$$\frac{\partial(\phi S_g \rho_g)}{\partial t} + \nabla \cdot (\rho_g \mathbf{q}_g) = \sum_{k=1}^{N} Q_g^k \tag{2-6b}$$

Equation (2-6b) can be rearranged to get

$$\phi \rho_g \frac{\partial S_g}{\partial t} + \nabla \cdot (\rho_g \mathbf{q}_g) + \frac{\partial(\phi \rho_g)}{\partial t} S_g = \sum_{k=1}^{N} Q_g^k \tag{2-7}$$

After some algebra on Equation (2-6a), adding it to Equation (2-7) and using Equation (2-3a), results in the following equation

$$\phi(\rho_g - \rho_l) \frac{\partial S_g}{\partial t} + \nabla \cdot (\rho_l \mathbf{q}_l + \rho_g \mathbf{q}_g) + \frac{\partial(\phi(\rho_g - \rho_l))}{\partial t} S_g = -\frac{\partial(\phi \rho_l)}{\partial t} + \sum_{k=1}^{N} (Q_l^k + Q_g^k) \tag{2-8}$$

Equations (2-7) and (2-8) can be used to solve the multiphase flow problem. Liquid pressure and gas saturation are chosen as the state variables, which is why this formulation is called pressure-saturation (P-S) approach.

2.1.2 Equations of state and constitutive relationships

The constitutive relationships given here are required to close the system of governing equations. The system is assumed to be isothermal at 14.7 °C (Joyce et al. 2019) and consists of water and hydrogen gas.

Water retention curve

Strictly speaking, a water retention curve can not only account for the retention of water in a porous medium due to capillarity, but may capture adsorption mechanisms as well (Silva and Grifoll 2007b). However, in the present work the calculated gas saturations are relatively low, so potential water vapor adsorption onto the solid phase is negligible. Furthermore, water cannot evaporate within the rock since gas immiscibility is assumed in the model. Consequently, water vapor adsorption is not at work and capillarity is the dominant mechanism of water retention. The capillary pressure is defined as the difference between the gas and liquid pressure, and is assumed to be a function of the liquid saturation (or volumetric liquid content)

$$P_c(S_l) = P_g - P_l \tag{2-9}$$

There are several models for the water retention curve that can be applied (e.g. Brooks and Corey 1964, van Genuchten 1980, Rossi and Nimmo 1994, Silva and Grifoll 2007b). In this work, the water retention and relative permeability functions are calculated per the van Genuchten model (1980) (see Sub-Section 2.2.5).

Density and viscosity

The density of the liquid phase is assumed constant and set at 1 003 kg/m^3. This value was calculated using the expression given by Abarca et al. (2019) assuming a salinity of 0.12 %. This is the average salinity within the domain considered in the present work (see Section 2.2.1), calculated with the data taken from the regional hydrology model (Joyce et al. 2019). The liquid viscosity is also assumed constant and equal to 2×10^{-3} Pa s (Joyce et al. 2019).

The repository depth is approximately 500 m (see Section 2.2.1). Gas generation due to the steel corrosion will increase the pressures in the system above 50 bar. In addition, vertical downwards groundwater flow can cause the gas phase to migrate to deeper zones of the host-rock, where the water pressures are higher. Because of this, gas is assumed to follow a non-ideal behavior. The gas density can be computed from an equation of state (EOS). Here, the Peng-Robinson EOS (Peng and Robinson 1976) is adopted

$$P_g = \frac{RT}{v-b} - \frac{a(T)}{v(v+b)+b(v-b)} \tag{2-10}$$

Above, $R = 8.13144621$ J/mol K is the universal gas constant, T (K) is temperature, v (m^3/mol) is the molar volume of the gas phase, while a (Pa m^6/mol^2) and b (m^3/mol) are factors given by

$$a = 0.45724\xi_{H_2}\frac{R^2T^2_{crit,H_2}}{P_{crit,H_2}}, \quad b = 0.077796\frac{RT_{crit,H_2}}{P_{crit,H_2}} \tag{2-11}$$

where $T_{crit,H_2} = 33.2$ K and $P_{crit,H_2} = 13$ bar are the critical temperature and pressure of hydrogen, respectively. The EOS parameter ξ_{H_2} is given by

$$\xi_{H_2} = \left(1-\chi_{H_2}\left[1-\sqrt{T/T_{crit,H_2}}\right]\right)^2 \tag{2-12a}$$

$$\chi_{H_2} = 0.37464 + 1.5423\omega_{H_2} - 0.26992\omega^2_{H_2} \tag{2-12b}$$

and $\omega_{H_2} = -0.127$ is the acentric factor of hydrogen. The acentric factors roughly express the deviation of the shape of a molecule from a sphere (Reid et al. 1977). Given the gas pressure, the molar volume of the gas phase is obtained by solving Equation (2-10), which is a cubic equation in v (Nickalls 1993). Then, the gas density is computed as

$$\rho_g = \frac{M_{H_2}}{v} \tag{2-13}$$

where M_{H_2} (kg/mol) is the molecular weight of hydrogen. The viscosity of the gas phase is calculated using the Chung et al. (1988) correlation

$$\mu_g = \mu_\kappa + \mu_p \tag{2-14a}$$

$$\mu_\kappa = \mu_0\left(1/G_2 + A_6Y\right) \tag{2-14b}$$

$$\mu_p = 36.344\times10^{-13}\frac{\sqrt{M_{H_2}T_{crit}}}{V^{2/3}_{crit}}A_7Y^2G_2\exp\left(A_8+\frac{A_9}{T^*}+\frac{A_{10}}{T^{*2}}\right) \tag{2-14c}$$

where $\mu_0 = 7.783\times10^{-6}$ Pa s is the hydrogen gas viscosity at 14.7 °C (calculated using Equation 6 of Chung et al. 1988), $Y = V_{crit}/6v$, $T^* = 1.2593T/T_{crit}$, $G_1 = (1.0-0.5Y)/(1-Y)^3$, $G_2 = \{A_1[1-\exp(-A_4Y)]/Y + A_2G_1\exp(A_5Y) + A_3G_1\}/(A_1A_4 + A_2 + A_3)$. The constants A_i (i=1,…,10) are linear functions of the acentric factor, the reduced dipole moment and the association factor of hydrogen. They are calculated according to Equation (11) of Chung et al. (1988) and the coefficients given in Table II of their work. In practice, the pressures simulated in the present work are not so high ($Y < 10^{-3}$) to have an impact on gas viscosity. Thus, the gas viscosity is almost constant and equal to μ_0. Pressure effects could be important if the repository would be located at greater depths, steel corrosion rates were significantly higher, or the host-rock permeability was very low.

2.2 Model with homogeneous host rock

2.2.1 Geometry

A schematic representation of the SFL layout is shown in Figure 1-1 and Figure 2-1. Figure 2-2 shows a schematic cross-section of the BHK vault, which is in focus in this work. The waste is segmented, after which the parts are deposited in steel tanks and stabilized with grout. The steel tanks are emplaced in concrete compartments which are also grouted. Upon closure, the entire vault will be backfilled with concrete.

The 2D model set up in this work considers a cross-section of the BHK vault at the reference position and orientation at 500 m depth, as described by Abarca et al. (2019). The BHK system components are represented by a waste domain and a backfill domain. The surrounding rock is assumed to be homogeneous.

Figure 2-3 shows the geometry and boundary conditions assumed for the case of hydrostatic conditions (Base Case; see Section 1.2 and Table 1-1). The rock domain is a 120 m × 120 m square. Preliminary test simulations showed that, with these dimensions, the boundary conditions do not affect gas flow around the vault before the gas reaches a boundary.

The lower left corner in the model domain is set at $x = 7\,988.9$ m and $z = -500.6$ m, coinciding with the local coordinate system of Abarca et al. (2019). Comsol local coordinates are calculated as $x = x_{RT90} - x_0$, $y = y_{RT90} - y_0$, where x_{RT90} and y_{RT90} are the coordinates of the reference system RT90 and $x_0 = 1\,539\,000$ and $y_0 = 6\,360\,000$ (see Vidstrand and Rhén 2011, Table 6-8, Joyce et al. 2019). The plane intersecting the BHK vault can be assumed to be located at the y coordinate corresponding to the center of the vault (approximately $y = 7\,200$ m).

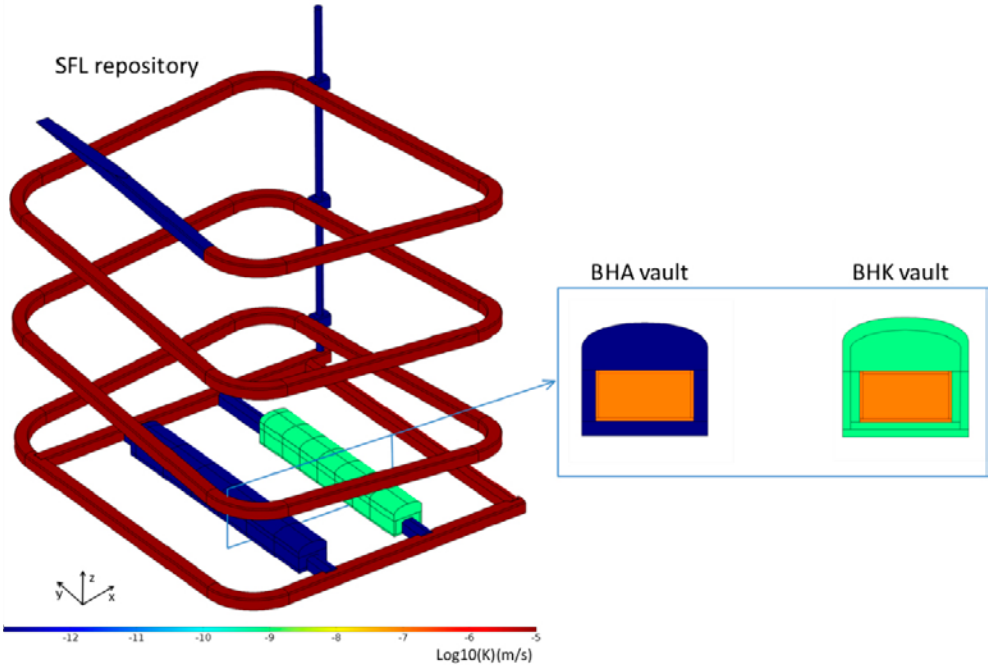

Figure 2-1. *Assignment of hydraulic conductivity to the materials in the SFL model domains (Abarca et al. 2019). The present model considers only a cross-section of the BHK vault (highlighted by the green color associated with the backfill material) and the surrounding host-rock.*

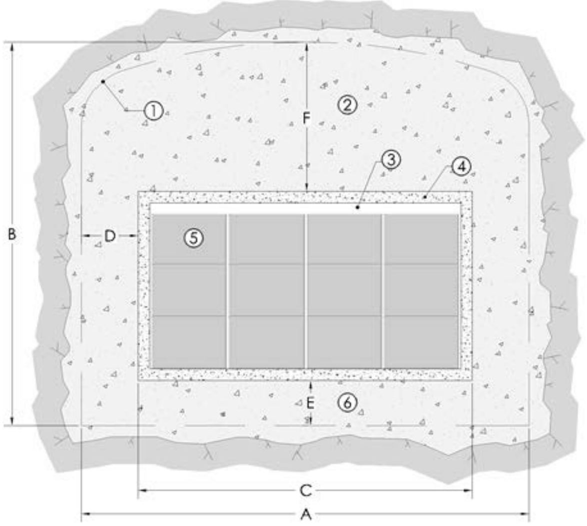

***Figure 2-2.** Schematic cross-sectional layout of the BHK vault for metallic waste (from Elfwing et al. 2013). Legend: 1.) Theoretical tunnel contour. 2) Concrete backfill. 3) Grout. 4) Concrete structure. (0.5 m). 5) Steel tanks. 6) Concrete. Approximated dimensions: A = 20.6 m, B = 19.6 m, C = 15 m, D = 2.8 m, E = 2.4 m, F = 8.8 m.*

2.2.2 Initial conditions

In the Base Case (see Figure 2-3), hydrostatic conditions are assumed initially and the water pressure field within the system is set to

$$P_{l,ini} = 101325 + \rho_l gz \tag{2-15}$$

The initial saturation of the gas phase ($S_{g,ini}$) is set at zero throughout the domain.

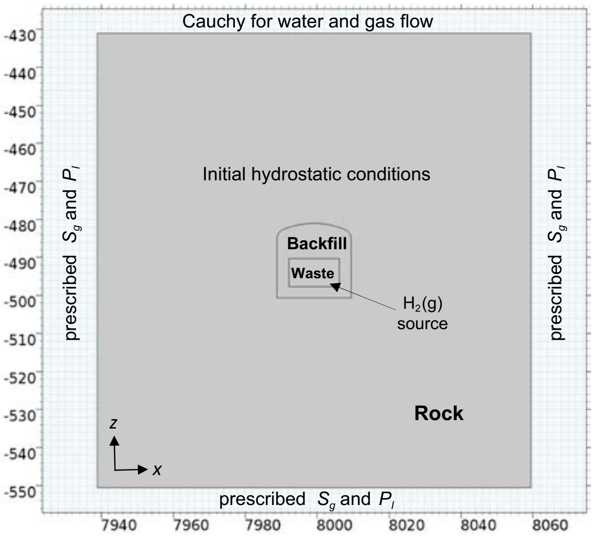

***Figure 2-3.** Geometry and boundary conditions implemented in the COMSOL model of immiscible two-phase flow in the BHK vault (Base Case).*

2.2.3 Boundary conditions

Mixed-type (Cauchy) boundary conditions are used to address the arrival of gas to a given boundary (Γ) and its impact on water flow at that boundary

$$\sum_{k=1}^{N} Q_g^k = Q_g = -\rho_g \left\{ \alpha_g^s \left(S_{g,ext} - S_g \right) - \alpha_g^p \left(P_{l,ext} - P_l \right) \right\} \qquad (x,z) \in \Gamma \tag{2-16a}$$

$$\sum_{k=1}^{N} Q_l^k = Q_l = \rho_l \alpha_l^p \left(P_{l,ext} - P_l \right) \qquad (x,z) \in \Gamma \tag{2-16b}$$

Above, $S_{g,ext}$ and $P_{l,ext}$ are external values of the state variables, which in this work are assumed to be equal to the initial values evaluated at the boundary. α_g^s (m/Pa s) and α_g^p (m/Pa s) are mass transfer coefficients for gas flow due to saturation and pressure variations, and α_l^p is a mass transfer coefficient for liquid flow due to pressure variations. These boundary conditions are implemented in Comsol as *weak contribution* to the flow equations. The Cauchy boundary condition specifies that the flow (Q_β, $\beta = l, g$) through that boundary is proportional to the pressure difference between the calculated pressure (P_β) and a prescribed external pressure ($P_{\beta,ext}$). The coefficients of proportionality α_β^p, $\beta = l$, g which are phase-dependent, can be extracted from the following form of Darcy flow for each phase

$$\begin{aligned} Q_\beta = \rho_l k \lambda_\beta \nabla P_\beta &= \rho_l \frac{k\lambda_\beta}{\left(y_{ext} - y \right)} \left(P_{\beta,ext} - P_\beta \right) \\ &= \rho_l \alpha_\beta^p \left(P_{\beta,ext} - P_\beta \right) \qquad \beta = l, g \end{aligned} \tag{2-17a}$$

$$\alpha_\beta^p = \frac{k\lambda_\beta}{\left(y_{ext} - y \right)} \tag{2-17b}$$

In the above equations, k (m^2) is the intrinsic permeability of the rock, y (m) is the position of the boundary in the direction perpendicular to that boundary, and y_{ext} (m) is the respective coordinate at the external position. In terms of the state variables (S_g and P_l) the gas flux reads

$$\begin{aligned} Q_g = \rho_g k \lambda_g \nabla P_g = \rho_g k \lambda_g \left(\nabla P_c + \nabla P_l \right) = \rho_g k \lambda_g \left(-\frac{\partial P_c}{\partial S_l} \nabla S_g + \nabla P_l \right) \\ = -\rho_g \frac{k\lambda_g}{\left(y_{ext} - y \right)} \frac{\partial P_c}{\partial S_l} \left(S_{g,ext} - S_g \right) + \rho_g \frac{k\lambda_g}{\left(y_{ext} - y \right)} \left(P_{l,ext} - P_l \right) \end{aligned} \tag{2-18a}$$

$$Q_g = -\rho_g \left\{ \alpha_g^s \left(S_{g,ext} - S_g \right) - \alpha_g^p \left(P_{l,ext} - P_l \right) \right\} \tag{2-18b}$$

$$\alpha_g^s = \alpha_g^p \frac{\partial P_c}{\partial S_l} \tag{2-18c}$$

The external variables $S_{g,ext}$ and $P_{l,ext}$ are assumed to be equal to the initial values evaluated at the boundary ($S_{g,ext} = 0$ and $P_{l,ext}$ given by Equation 2-15). The distance from the external position to the boundary where the Cauchy condition is imposed, $\Delta y_{ext} = |y_{ext} - y|$, controls the water and gas fluxes. As this distance decreases, the Cauchy condition approaches a Dirichlet condition (prescribed S_g and P_l). Δy_{ext} was tuned such that the gas saturation gradient at the boundary is smooth (no gas accumulation or depletion).

When groundwater flow is horizontal, the flow is induced by imposing a constant water flux q at the lateral boundaries of the domain, as shown in Figure 2-4. The initial pressure distribution is defined as

$$P_{l,ini}(x, y) = P_{atm} - \rho_l g z + \frac{q}{\lambda_l k} \left(x - x_{left} \right) \tag{2-19}$$

where x_{left} is the horizontal coordinate of the left boundary. A Cauchy boundary condition (see Equation 2-16a) is assumed for the gas flow at the right boundary because it is expected that the gas may reach this boundary.

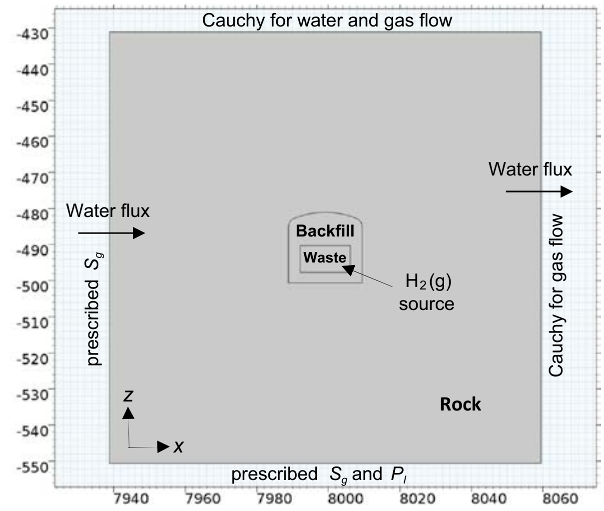

Figure 2-4. *Geometry and boundary conditions implemented in the COMSOL model to simulate H_2(g) generation and migration in the BHK vault with horizontal groundwater flow.*

In the case of vertical downwards groundwater flow, the water flux is induced by a pressure difference. The initial pressure distribution is defined as

$$P_{l,ini}(x,y) = P_{atm} - \rho_l g z + \frac{q}{\lambda_l k}\left(z - z_{bottom}\right) \tag{2-20}$$

where z_{bottom} is the vertical coordinate of the bottom boundary. For low water fluxes (e.g., 2.33×10^{-10} m/s), the gas flows upwards, so Cauchy boundary conditions are imposed at the top boundary (Figure 2-5a). For medium water fluxes (e.g., 1.89×10^{-8} m/s), the gas flows upwards and laterally, so Cauchy boundary conditions are also imposed at the lateral boundaries (Figure 2-5b). Finally, for high water fluxes (e.g., 5.00×10^{-8} m/s), the gas flows downwards, so Cauchy boundary conditions are imposed only at the bottom boundary (Figure 2-5c).

The distance from the external position to the boundary where the Cauchy condition is applied, Δy_{ext}, has been included in Table 4-2 for each simulation case with homogeneous rock. The selected Δy_{ext} values were found by a trial and error procedure. They are optimal in the sense that higher or lower values yield unrealistic results. Very high Δy_{ext} cause a gas accumulation at the boundary, while very low Δy_{ext} are equivalent to prescribing the gas saturation and the liquid pressure. Both extreme situations would result in a very steep gradient of gas saturation when the gas reaches the boundary, which is physically infeasible.

At the remaining boundaries, the liquid pressure and the gas saturation are set to their initial values.

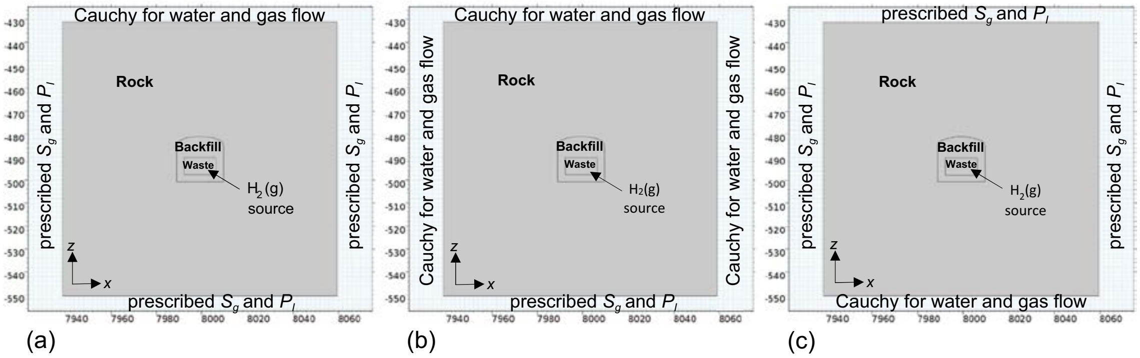

Figure 2-5. *Geometry and boundary conditions implemented in the COMSOL model to simulate H_2(g) generation and migration in the BHK vault with vertical downwards groundwater flow. The vertical water flux is (a) 2.33×10^{-10} m/s, (b) 1.89×10^{-8} m/s and (c) 5.00×10^{-8} m/s.*

2.2.4 Source and sink terms

Hydrogen gas is produced within the waste due to the steel corrosion. This is represented by a gas source term applied over the waste sub-domain Ω_{waste} (see Figure 2-3).

$$Q_g^{H_2}(x,z) = r_{H_2(g)} \qquad (x,z) \in \Omega_{waste} \tag{2-21}$$

where $r_{H2(g)}$ (kg/m^3 s) is the hydrogen generation rate. Water consumption is disregarded so $Q_l^w(x,z) = 0$ in Equations (2-7) and (2-8).

The hydrogen generation rates in the BHK vault can be calculated from the steel corrosion rates and the stoichiometry of associated chemical reactions (Román-Ross et al. 2015). It is assumed that the corrosion of iron by water under anaerobic conditions produces H_2(g) and Fe(II) hydroxide, per the following reaction

$$\mathrm{Fe_{(s)} + 2H_2O = Fe(OH)_{2(s)} + H_{2(g)}} \tag{2-22}$$

$\mathrm{Fe(OH)_{2(s)}}$ is metastable and forms iron oxide over time (Ernst 1969), e.g., magnetite

$$\mathrm{3Fe(OH)_{2(s)} = Fe_3O_4 + H_2 + 2H_2O} \tag{2-23}$$

If magnetite is formed in accordance with the above reactions, 4/3 moles of H_2(g) are formed for every mol of Fe(s) consumed in the corrosion process. For a given a corrosion rate r_c (m/s) the molar hydrogen generation rate $\hat{r}_{H_2(g)}$ (mol/m^2·s) can be calculated as

$$\hat{r}_{H_2(g)} = r_c \frac{\rho_{steel}}{M_{Fe}} w_{Fe,steel} \frac{4}{3} \tag{2-24}$$

where ρ_{steel} (kg/m^3) and $w_{Fe,steel}$ (-) are the steel density and the iron content in the steel, respectively, and M_{Fe} (kg/mol) is the molar weight of Fe. The corresponding hydrogen generation rate $r_{H2(g)}$ is calculated as

$$r_{H_2(g)} = M_{Fe} \frac{A}{V} \hat{r}_{H_2(g)} \tag{2-25}$$

Above, A (m^2) and V (m^3) are the total surface area of steel and the total volume of waste in the BHK vault, respectively. Also, the initial steel (Fe) concentration $c_{Fe,ini}$ (kg/m^3) can be expressed as

$$c_{Fe,ini} = \frac{M_{steel} w_{Fe,steel}}{\phi V} \tag{2-26}$$

where M_{steel} (kg) is the total mass of steel in the BHK vault. The corrosion time t_{corr} (s) is calculated from the concentration and the hydrogen generation rate (Equation 2-25)

$$t_{corr} = \frac{c_{Fe,ini}}{r_{H_2(g)}} \tag{2-27}$$

The parameters required to calculate the hydrogen generation rates in the BHK vault are summarized in Table 2-1. Note that the BHK vault contains both carbon and stainless steel, exhibiting different rates. Anoxic, hyper-alkaline conditions are assumed to prevail, leading to a typical corrosion rate of 0.05 µm/year (Smart and Hoch 2006, Pękala et al. 2018). The hydrogen generation rate used results from adding the rates associated with the corrosion of carbon steel and stainless steel

$$r_{H_2(g)} = \begin{cases} 4.95\times10^{-12}\ \text{kg/m}^3\text{s} & t \le 74920\ \text{yr} \\ 2.67\times10^{-12}\ \text{kg/m}^3\text{s} & 74920\ \text{yr} < t \le 615313\ \text{yr} \\ 0 & t > 615313\ \text{yr} \end{cases} \tag{2-28}$$

Table 2-1. Steel corrosion rate and other properties used to calculate the hydrogen generation rates in the BHK vault.

Parameter	Carbon steel	Stainless steel
r_c, µm/year	0.05	
M_{Fe}, kg/mol	0.055845	
ϕ, m³/m³	0.3	
V, m³	12 254.7	
A, m²	55 000	68 000
ρ_{steel}, kg/m³	7 860	7 930
M_{steel}, kg	1.33×10^{7}	2.02×10^{6}
$w_{Fe,steel}$	0.99	0.68
$c_{Fe,ini}$, kg/m³	3 581.5	373.6
$r_{H2(g)}$, kg/m³-s	2.67×10^{-12}	2.28×10^{-12}
t_{corr}, years	615 313	74 920

2.2.5 Hydraulic and transport properties

The water retention curves of the different materials are assumed to follow the van Genuchten model (van Genuchten 1980)

$$P_c = P_0\left(S_e^{-1/m} - 1\right)^{1/n} \tag{2-29}$$

$$S_e = \frac{S_l - S_{lr}}{1 - S_{lr} - S_{gr}}, \quad m = 1 - \frac{1}{n}$$

Above, S_e is the effective saturation of the liquid phase, P_0 (Pa) a scaling pressure related to the gas entry pressure P_{entry} (Pa), S_{lr} and S_{gr} are the residual saturation of the liquid and gas phase, respectively, and n is a parameter related to the pore size distribution. The relative permeabilities of the liquid and gas phases are also calculated from the van Genuchten model (van Genuchten 1980) as

$$k_{rl} = S_e^{0.5}\left(1 - \left(1 - S_e^{1/m}\right)^m\right)^2 \tag{2-30a}$$

$$k_{rg} = \left(1 - S_e^2\right)\left(1 - S_e\right)^2 \tag{2-30b}$$

The gas entry pressure is often estimated as the pressure at which the relative permeability of the liquid drops below a predetermined value, say 0.9 (Rucker et al. 2005). From Equations (2-29) and (2-30a), $P_{entry} = P_0(1 - 0.9S_{entry}^{-0.5})^{1/m}/[1 - (1 - 0.9S_{entry}^{-0.5})^{1/m}]$, where S_{entry} is the effective saturation at which $k_{rl} = 0.9$. The hydraulic parameters corresponding to each material are shown in Table 2-2. The water retention and permeability functions are displayed in Figure 2-6.

Table 2-2. Hydraulic parameters assumed for the different materials of the BHK vault and the surrounding rock.

Parameter	Waste	Backfill	Rock
Porosity, ϕ	0.3(a)	0.11(a)	4.37×10^{-4}(b)
Permeability, k (m²)	2.0×10^{-14}(a)	1.7×10^{-16}(a)	6.67×10^{-15}(b)
Residual liquid saturation, S_{lr}	0.0	0.0	0.0
Residual gas saturation, S_{gr}	0.0	0.0	0.0
n	2.00(d)	1.78(c)	2.32(e)
Scaling pressure, P_0 (MPa)	0.050(d)	1.677(c)	0.871(e)

(a) SKB (2014).

(b) Values calculated from statistics (see Section 4.1).

(c) Baroghel-Bouny et al. (1999).

(d) In some simulations the water retention curves of the waste are assumed to be equal to the water retention curves of the backfill.

(e) Arithmetic average between values reported by Finsterle and Pruess (1995) and Jarsjö et al. (2001).

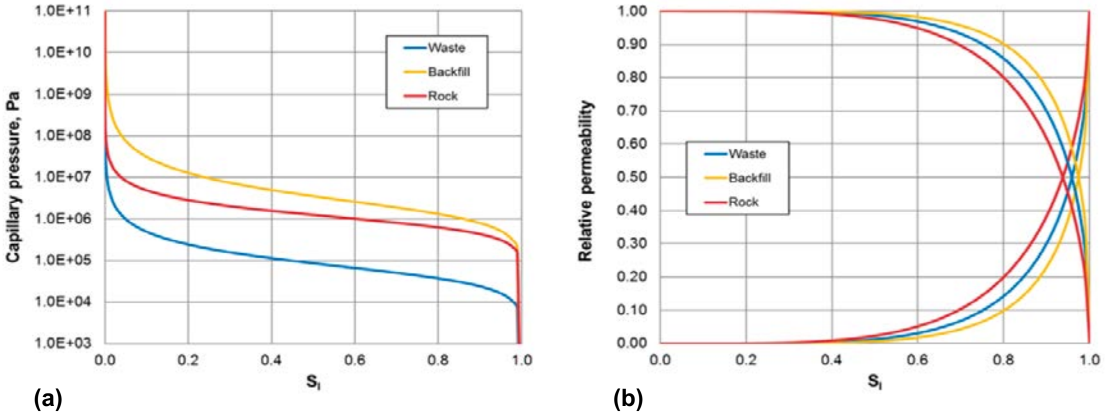

Figure 2-6. *(a) Water retention and (b) relative permeability functions of the different materials in BHK.*

The system is assumed to be isothermal at 14.7 °C, which is the temperature at the depth of the BHK vault (Joyce et al. 2019). The transport parameters of the liquid and gas phases are summarized in Table 2-3.

Table 2-3. Transport parameters for the liquid and gas phases.

Parameter	Value
Liquid density, ρ_l (kg/m^3)	1 003[(a)]
Liquid viscosity, μ_l (Pa-s)	2.0×10^{-3}[(b)]
Gas density, ρ_g (kg/m^3)	Peng-Robinson EOS[(c)] (Equation 2-10)
Gas viscosity μ_g (MPa)	Chung's correlation[(d)] (Equation 2-14)

[(a)] Abarca et al. (2019), assuming a salinity of 0.12 %
[(b)] Joyce et al. (2019)
[(c)] Peng and Robinson (1976)
[(d)] Chung et al. (1988)

2.3 Model with fracture zone

A fracture zone has been added to the model in an alternate representation of the granitic host rock. The fracture zone is conceptualized as an equivalent continuous porous medium (ECPM), with specific permeability, porosity, water retention curve and permeability function. The governing equations (2-7) and (2-8) are also valid for the fracture zone. In this work, an arbitrary fracture zone of 1 m thickness has been introduced, such that it intersects the BHK vault (see Figure 2-7). The sink and source terms explained in 2.2.4 are used in this case as well.

2.3.1 Boundary conditions

The fracture zone directs the fluid flow upwards and to the left. Therefore, Cauchy boundary conditions (Equations 2-17 and 2-18) are also imposed at the left boundary of the domain (see Figure 2-7).

Fracture zones are preferential pathways for fluid flow. Also, flow through fractures zones is faster, especially for high fracture permeabilities. Lower pressures in fracture zones are reached faster than in the rock. For this reason, the external pressure $P_{l,ext}$ at the lateral boundary of the fracture zone is assumed to be lower than in the remaining boundary. This external pressure difference also accounts for the connectivity of the fracture zone with zones away from the BHK vault. The lower $P_{l,ext}$, the higher the fluid flow through the fracture zone (see Equations 2-17a and 2-18b) and the higher the connectivity with distant regions. In this work, $P_{l,ext}$ at the lateral boundary of the fracture zone has been set 5 % lower than the external pressure in the rock. External pressures can be assumed to vary linearly with the hydrostatic pressure. The above is equivalent to an increase of 5.1 % in the water flux through the fracture lateral boundary, compared to the flux calculated with the rock external pressure. Also, this implies a hypothetical connectivity of the fracture with zones that are located 20 m above the depth of the fracture lateral boundary.

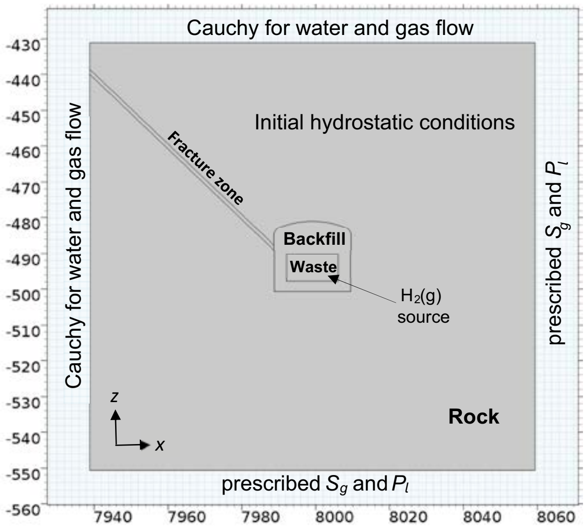

Figure 2-7. *Geometry and boundary conditions implemented in the COMSOL model of immiscible two-phase flow in the BHK vault for the case including a fracture zone.*

2.3.2 Hydraulic properties

The permeability and the water retention curve of the fracture zone are required inputs of the model. Figure 2-8a summarizes the data compiled by Rhén et al. (2008) (see the statistics presented in Appendix 4 of Rhén et al. 2008) on the transmissivity of local minor deformation zones (MDZ) in Laxemar. This transmissivity data has been converted into permeability (Figure 2-8b) by using the values of water density and viscosity shown in Table 2-3, and assuming a fracture zone thickness of 1.0 m.

These statistics are represented as a normal distribution in Figure 2-9. The maximum and minimum permeability of the fracture zone is 2.50×10^{-11} m^2 and 5.70×10^{-17} m^2, respectively, while the average permeability is 9.08×10^{-13} m^2. The probability function shows that 95 % of the permeability data is lower than 6.18×10^{-12} m^2, and 75 % is lower than 3.07×10^{-12} m^2. Also, 40 % of the data is lower than 5.0×10^{-14} m^2.

The fracture zone porosity was assumed constant and equal to 0.01. This value was estimated using the correlation given in Rhén et al. (2008) for kinematic porosity of deformation zones and the coefficients suggested by Hjerne et al. (2010).

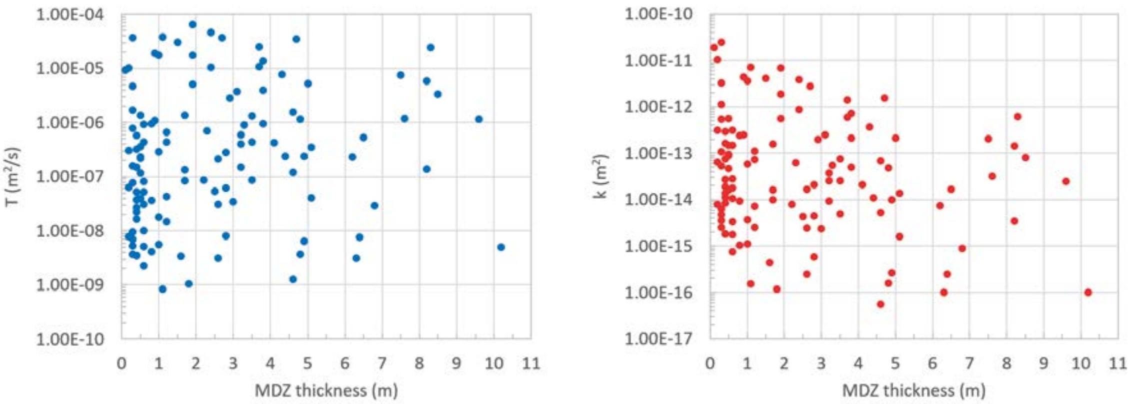

(a) (b)

Figure 2-8. *(a) Statistics of transmissivity of minor deformation zones measured in Laxemar compiled in Rhén et al. (2008) and (b) converted permeability data assuming water density and viscosity shown in Table 2-3.*

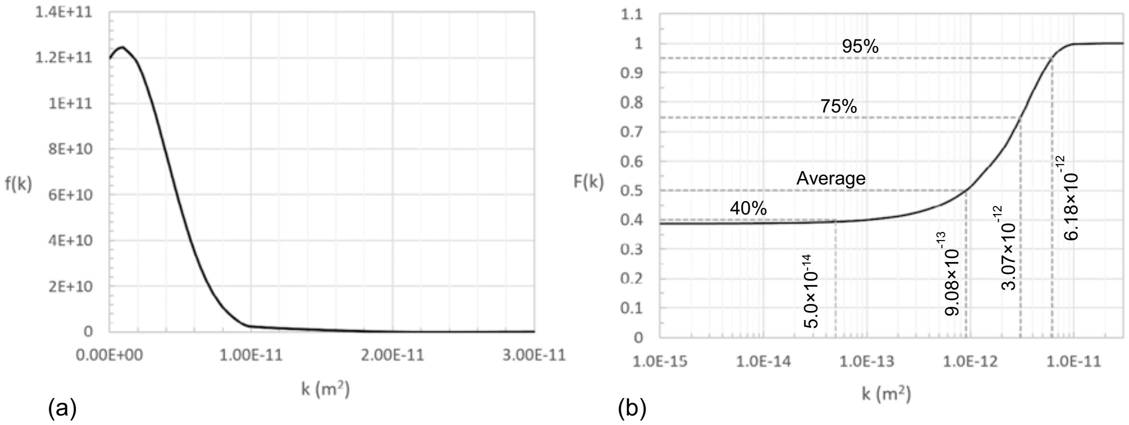

***Figure 2-9.** (a) Probability density function and (b) accumulated probability function of deformation zone permeability, calculated from the statistics found in Rhén et al. (2008) (see Figure 2-8).*

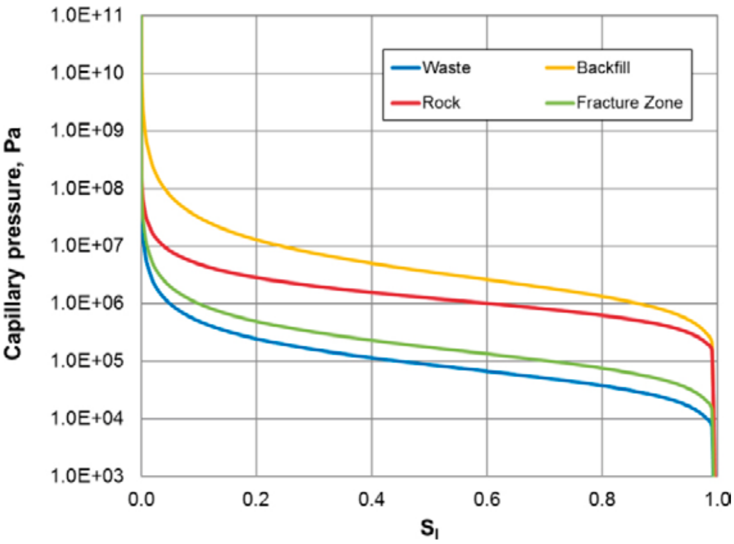

***Figure 2-10.** Water retention curves considered to simulate immiscible two-phase flow in the BHK vault including a fracture zone.*

Given the uncertainty on the hydraulic characterization of fracture zones in Laxemar under two-phase flow conditions, the van Genuchten parameter *n* of the fracture zone is set arbitrarily to 2, while the scaling pressure P_0 is set to 10^5 Pa, which is lower than the scaling pressure assumed for rock and backfill. The rule is that, the lower P_0, the easier for the gas to enter a fracture zone. Also, the water retention curve of the fracture zone can be estimated by scaling the water retention curve of the rock by the Leverett factor, $(T_{rock}/T_{frac})^{1/3}$ (Jarsjö et al. 2001). T_{rock} (m²/s) and T_{frac} (m²/s) are the transmissivities of the rock and fracture zone, respectively. From the statistics of fracture transmissivity, the scaling factor ranges between 0.065 and 0.5. This is consistent with the difference displayed in Figure 2-10 between the red and green lines. Thus, the above parameters of the water retention curve can be considered representative of the fracture zone. Note that increasing P_0 reduces the capillary difference between the fracture and the rock, bringing the system to conditions equivalent to that of the homogeneous host-rock. In the limit, when the water retention curves are the same, fluid flow through the fracture is only driven by the fracture zone permeability. As shown in Figure 2-10, the water retention curve of the fracture zone lies between the water retention curves of the waste and the rock. Because of the above assumptions, the relative permeability of the fracture zone coincides with the relative permeability of the waste (see Equation 2-29 and Figure 2-6b).

3 Numerical implementation

The governing equations described in Chapter 2 have been implemented in COMSOL Multiphysics 5.2a (COMSOL 2015) using the coefficient form of the partial differential equation (PDE) modelling interface

$$\mathbf{e}_\mathbf{a}\frac{\partial^2\mathbf{u}}{\partial t^2}+\mathbf{d}_\mathbf{a}\frac{\partial\mathbf{u}}{\partial t}+\nabla\cdot\left(-\mathbf{c}\nabla\mathbf{u}-\boldsymbol{\alpha}\mathbf{u}+\boldsymbol{\gamma}\right)+\boldsymbol{\beta}\cdot\nabla\mathbf{u}+\mathbf{a}\mathbf{u}=\mathbf{f} \tag{3-1}$$

where $\mathbf{u} = (u_1,\ldots,u_k,\ldots,u_N)^\mathrm{T}$ is a vector of N unknowns, $\mathbf{e}_\mathbf{a}$ the mass coefficient, $\mathbf{d}_\mathbf{a}$ the damping coefficient, $\mathbf{c}$ the diffusion coefficient, $\boldsymbol{\alpha}$ the conservative flux convection coefficient, $\boldsymbol{\beta}$ the convection coefficient, $\mathbf{a}$ the absorption coefficient, γ the conservative flux source term, and $\mathbf{f}$ the source term.

The P-S approach implementation of the homogeneous medium model and the model including a fracture zone is explained in Section 3.1. The spatial and temporal discretization of the models is described in Section 3.2. The two-phase immiscible flow model of and its implementation in COMSOL has been verified using published benchmarks[1].

3.1 Pressure-saturation approach

The pressure-saturation (P-S) approach of two-phase flow is based on Equations (2-7) and (2-8). The state variables are the saturation of the gas phase (S_g) and the liquid pressure (P_l).

The governing equations (2-7) and (2-8) are further developed below to express them in the form of Equation (3-1) for its implementation in COMSOL.

3.1.1 Flow equations

Note that using the definition of capillary pressure (Equation 2-9) the Darcy's flux of gas phase (Equation 2-4) can also be expressed as

$$\begin{aligned}\mathbf{q}_g&=-\mathbf{k}\lambda_g\left(\nabla P_g+\rho_g g\mathbf{z}\right)=-\mathbf{k}\lambda_g\left(\nabla P_l+\nabla P_c+\rho_g g\mathbf{z}\right)\\&=-\mathbf{k}\lambda_g\left(\nabla P_l+\frac{\partial P_c}{\partial S_g}\nabla S_g+\rho_g g\mathbf{z}\right)\end{aligned} \tag{3-2}$$

Substituting Equation (3-2) and the Darcy's flux of the liquid phase (Equation 2-4) into Equations (2-7) and (2-8), produces the following flow equations

$$\phi\rho_g\frac{\partial S_g}{\partial t}+\nabla\cdot\left(-\mathbf{k}\lambda_g\rho_g\nabla P_l-\mathbf{k}\lambda_g\rho_g\frac{\partial P_c}{\partial S_g}\nabla S_g-\mathbf{k}\lambda_g\rho_g^2 g\mathbf{z}\right)+\frac{\partial(\phi\rho_g)}{\partial t}S_g=\sum_{k=1}^{N}Q_g^k \tag{3-3}$$

$$\begin{aligned}&\phi(\rho_g-\rho_l)\frac{\partial S_g}{\partial t}+\nabla\cdot\left(-\mathbf{k}(\lambda_g\rho_g+\lambda_l\rho_l)\nabla P_l-\mathbf{k}\lambda_g\rho_g\frac{\partial P_c}{\partial S_g}\nabla S_g-\mathbf{k}\left(\lambda_g\rho_g^2+\lambda_l\rho_l^2\right)g\mathbf{z}\right)\\&\qquad+\frac{\partial(\phi(\rho_g-\rho_l))}{\partial t}S_g=-\frac{\partial(\phi\rho_l)}{\partial t}+\sum_{k=1}^{N}\left(Q_l^k+Q_g^k\right)\end{aligned} \tag{3-4}$$

---

[1] **Silva O, 2017.** Development of an interface to communicate COMSOL Multiphysics and PhreeqC. The iMaGe – iCP Project. Year 2. SKBdoc 1608934 ver 1.0, Svensk Kärnbränslehantering AB. Internal document.

Comparing Equations (3-3) and (3-4) with (3-1) the unknowns and coefficients for the P-S approach can be identified as

$$\mathbf{u} = \left(S_g, P_l\right)^T \tag{3-5a}$$

$$\mathbf{e_a} = \mathbf{0} \tag{3-5b}$$

$$\mathbf{d_a} = \begin{pmatrix} \phi\rho_g & 0 \\ \phi\left(\rho_g - \rho_l\right) & 0 \end{pmatrix} \tag{3-5c}$$

$$\mathbf{c} = \begin{pmatrix} \lambda_g \rho_g \mathbf{k} \dfrac{\partial P_c}{\partial S_g} & \lambda_g \rho_g \mathbf{k} \\ \lambda_g \rho_g \mathbf{k} \dfrac{\partial P_c}{\partial S_g} & \left(\lambda_g \rho_g + \lambda_l \rho_l\right)\mathbf{k} \end{pmatrix} \tag{3-5d}$$

$$\boldsymbol{\alpha} = \mathbf{0} \tag{3-5e}$$

$$\boldsymbol{\gamma} = \begin{pmatrix} -\lambda_g \rho_g^2 g \mathbf{kz} \\ -\left(\lambda_g \rho_g^2 + \lambda_l \rho_l^2\right) g \mathbf{kz} \end{pmatrix} \tag{3-5f}$$

$$\boldsymbol{\beta} = \mathbf{0} \tag{3-5g}$$

$$\mathbf{a} = \begin{pmatrix} \dfrac{\partial\left(\phi\rho_g\right)}{\partial t} & 0 \\ \dfrac{\partial\left(\phi\left(\rho_g - \rho_l\right)\right)}{\partial t} & 0 \end{pmatrix} \tag{3-5h}$$

$$\mathbf{f} = \begin{pmatrix} \displaystyle\sum_{j=1}^{N} Q_g^j \\ -\dfrac{\partial\left(\phi\rho_l\right)}{\partial t} + \displaystyle\sum_{j=1}^{N}\left(Q_l^j + Q_g^j\right) \end{pmatrix} \tag{3-5i}$$

The partial derivatives of Equations (3-5d), (3-5h) and (3-5i) are calculated internally in COMSOL.

3.2 Model mesh, time-stepping and solver

The carbon steel corrosion time is 615 313 years (see Table 2-1 and Equation 2-28). The simulation time was set at 1 000 000 years to include the 2 steel corrosion regimes, as well as the system evolution once gas generation is stopped.

3.2.1 Model with homogeneous host rock

The geometry of the model with homogeneous host rock is discretized into 15 536 triangular elements. The mesh is illustrated in Figure 3-1. Preliminary test simulations showed that the high contrast of hydraulic properties between the different materials of the vault causes abrupt changes of gas saturation at the interfaces. This negatively impacts numerical convergence. The difference in the hydraulic properties between the waste and backfill is significantly higher than between the backfill and the host-rock (see Table 2-2 and Figure 2-6). For that reason, the mesh refinement in the waste and backfill sub-domains is higher than in the rock.

Time stepping is defined through the Generalized Alpha method with variable steps taken by the solver starting from an initial step of 10^{-10} yr. The direct solver PARDISO is used with the Newton-Raphson method with a constant damping factor of 1.0, a relative tolerance of 10^{-7} and the maximum number of iterations set to 10. The absolute tolerance was set at10^{-3}.

Equations (3-3) and (3-4) (and equivalently, Equations 3-1 and 3-5) are solved in a coupled way with a Segregated Solver, using the constant Newton-Raphson method updating the Jacobian at all iterations.

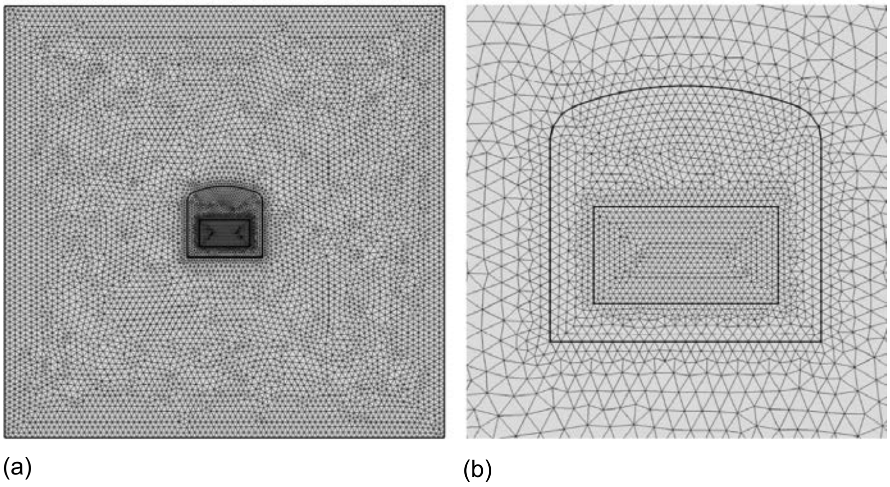
(a) (b)

Figure 3-1. (a) Numerical mesh of the full modelling domain and (b) a zoom in around the vault.

In COMSOL, the absolute and relative tolerances control the error in each integration step. The above solver settings produced accurate solutions for the combination of hydraulic parameters (see Section 2.2.5) and spatial meshes considered. If the contrast of hydraulic properties between different materials is higher or finer meshes are required, accurate solutions can be obtained by reducing the absolute tolerance.

3.2.2 Model with fracture zone

The geometry of the model including a fracture zone intersecting BHK is discretized into 58 004 triangular elements (see Figure 3-2).

Implicit Backwards Differentiation Formula (BDF, with maximum order of interpolating polynomial adjustable from 1, i.e. backward Euler, to 2) is used for time stepping. Steps taken by the solver are variable with an initial step of 10^{-10} yr. The direct solver MUMPS with a memory allocation factor of 2 is used with the Newton-Raphson method, with a constant damping factor of 1.0, a relative tolerance of 10^{-7} and a maximum number of iterations set to 10. An absolute tolerance of 10^{-5} was considered because of the finer mesh and the added contrast of hydraulic properties caused by the inclusion of the fracture zone.

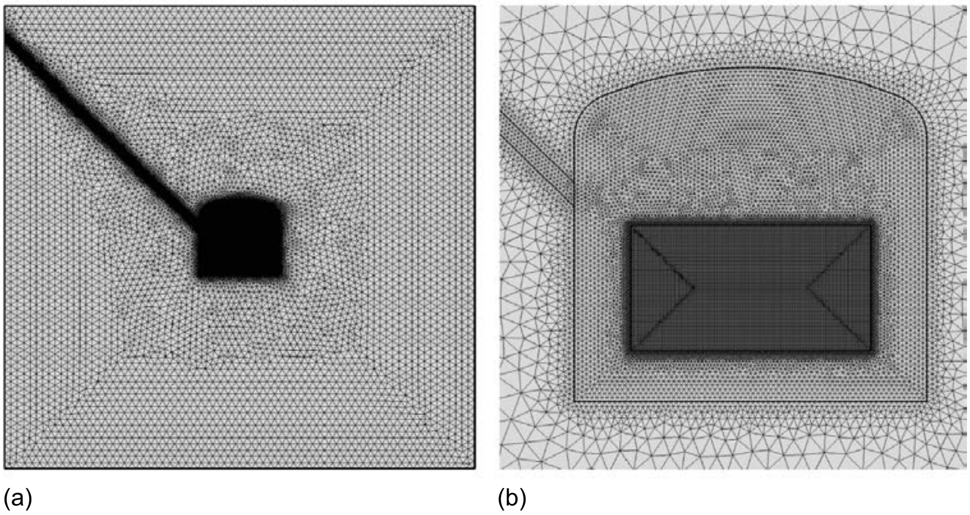
(a) (b)

Figure 3-2. (a) Numerical mesh of the full modelling domain and (b) a zoom in around the vault.

4 Results and discussion

The immiscible two-phase flow model is used to simulate several cases of hydrogen generation and migration. First, the rock surrounding the BHK vault is considered as a homogeneous porous medium. Different combinations of groundwater conditions and material properties are studied. The main results of these simulations are described and discussed in Section 4.1. Thereafter, the host rock is assumed to include a fracture zone, which is conceptualized as an ECPM. A series of sensitivity simulations varying the permeability of the fracture zone is performed, and the results are presented in Section 4.2.

The analysis of results is based on the evolution of the following variables:

- Gas saturation and liquid pressure distributions.
- Gas and liquid velocity fields.
- Gas pressure at specific locations in and around the BHK vault.
- Average gas pressure ($\overline{p_g}$) and average gas overpressure ($\overline{\Delta p_g}$) in the BHK vault, calculated as

$$\overline{p_g}(t) = \frac{1}{V_{BHK}} \int_{V_{BHK}} p_g(t) dV \tag{4-1a}$$

$$\overline{\Delta p_g}(t) = \overline{p_g}(t) - \overline{p_g}(0) \tag{4-1b}$$

In (4-1a), V_{BHK} (m^3) is the volume of the BHK vault.

- Inflow ($Q_{\beta,in}$) and outflow ($Q_{\beta,out}$) rates (m^3/s) of water and gas to/from the BHK vault and waste compartment, given by

$$Q_{\beta,in} = \int_{\Sigma, \mathbf{q}_\beta \cdot \mathbf{n} \geq 0} \mathbf{q}_\beta \cdot \mathbf{n} dS \tag{4-2a}$$

$$Q_{\beta,out} = \int_{\Sigma, \mathbf{q}_\beta \cdot \mathbf{n} < 0} \mathbf{q}_\beta \cdot \mathbf{n} dS \tag{4-2b}$$

In Equations (4-2a) and (4-2b), Σ is the surface of the BHK vault or the waste compartment, **n** is the unit vector normal to that surface, and $\beta = l, g$.

4.1 Homogeneous host rock

As explained in Section 1.2, three groundwater flow conditions are simulated when the host rock is assumed to be homogeneous. The first one, which is selected as the Base Case, considers hydrostatic conditions. The second and third conditions are for horizontal and vertical downwards groundwater flow. Each flow case is simulated using equal or different water retention curves of the waste and the backfill (see Equation 2-29, Table 2-2 and Figure 2-6a). Moreover, for each groundwater flow condition and combination of material properties, three groundwater flux magnitudes are explored. This leads to 14 simulation cases (see Table 1-1 and Table 4-2).

The hydraulic properties of the rock were estimated as follows. First, groundwater flux, porosity and permeability of the rock were obtained from the regional geohydrology model of SFL (Joyce et al. 2019). These properties were calculated in a box of 500 m × 500 m × 180 m ($7\,750 \leq x \leq 8\,250$; $7\,000 \leq y \leq 7\,500$; $-580 \leq z \leq -400$) enclosing the 2D domain used in the present simulations. Histograms of the obtained porosity and groundwater flux magnitude are shown in Figure 4-1. Histograms of the components of the permeability tensor are shown in Figure 4-2. They provide an idea of the heterogeneity of the regional hydrogeological system of SFL (Joyce et al. 2019). The minimum, maximum and average values of these hydraulic properties are shown in Table 4-1. In the current model, the permeability is assumed to be an isotropic tensor. The permeability values shown in Table 4-1 were calculated as the arithmetic mean of the components of the rock permeability tensor ($k = (k_x + k_y + k_z)/3$, see Figure 4-2). Also, in all the simulations performed in this work, the rock porosity and permeability were set at $\phi = 4.37 \times 10^{-4}$ and $k = 6.67 \times 10^{-15}$ m^2, respectively (Table 2-2).

These values are slightly lower than the average values presented in Table 4-1, but may represent better the hydraulic properties in the very NF of the BHK vault.

Two of the simulated groundwater fluxes are in the range predicted by the regional geohydrology model (Joyce et al. 2019; see Table 4-1). A flux of 2.33×10^{-10} m³/m² s, slightly lower than the average measured flux, was selected to simulate "low water flow" conditions. The maximum measured flux (1.89×10^{-8} m³/m² s) was considered to simulate "medium water flow" conditions. Note that in the horizontal and vertical downwards groundwater flow the groundwater flux must be high enough to overcome hydrostatic conditions and buoyancy forces that drive the gas upwards. For that reason, a third groundwater flux of 5.00×10^{-8} m³/m² s was selected to simulate "high water flow" conditions. This relatively large flux allows for evaluation of hypothetical cases where high pressures are developed in BHK due to downward vertical water flow.

Table 4-1. Minimum, maximum and average values of rock porosity, permeability and flux magnitude derived from the regional geohydrology model (Joyce et al. 2019).

Parameter	Minimum	Maximum	Average
Flux magnitude, q (m³/m² s)	5.02×10^{-18}	1.89×10^{-8}	3.07×10^{-10}
Porosity, ϕ	3.20×10^{-5}	1.59×10^{-2}	6.24×10^{-4}
Permeability, k (m²)	5.00×10^{-18}	2.65×10^{-12}	1.33×10^{-14}

Also, note that for low flow conditions, the evolution of the system is very similar to that found for hydrostatic conditions. For that reason, only the results obtained for medium and high flow conditions are presented in figures and compared to the results corresponding to hydrostatic conditions. The results obtained for low flow conditions are included in the Appendix A.

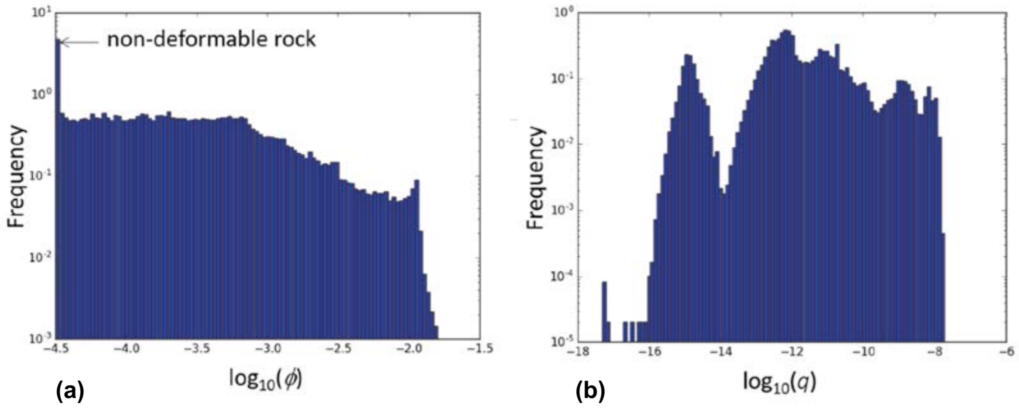

Figure 4-1. Histograms of (a) rock porosity and (b) groundwater flux magnitude calculated with ConnectFlow (Amec Foster Wheeler 2015) and the regional geohydrology model of SFL (Joyce et al. 2019).

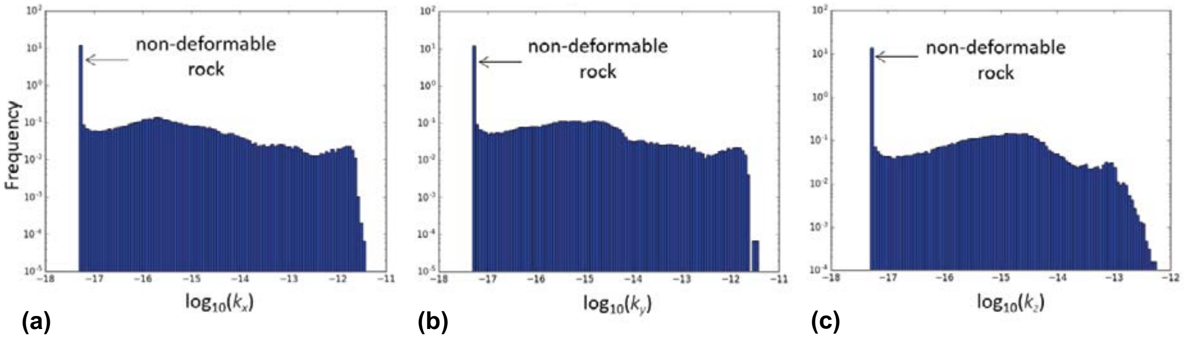

Figure 4-2. Histograms of rock permeability in the (a) x lateral, (b) y lateral and (c) z vertical directions obtained with ConnectFlow (Amec Foster Wheeler 2015) and the regional geohydrology model of SFL (Joyce et al. 2019).

Table 4-2. Cases to study hydrogen generation and migration around BHK with homogeneous rock.

Case #	Groundwater flow conditions	Waste and backfill retention curves*	Water flux (m^3/m^2 s)*	Cauchy condition, Δy_{ext} (m)	
				Vertical boundary	Lateral boundary
1	Hydrostatic	Same**	-	10.77	-
2	Hydrostatic	Different**	-	10.77	-
3	Low horizontal flow	Same	2.33×10^{-10}	10.77	3.63
4	Medium horizontal flow	Same	1.89×10^{-8}	4.31	3.63
5	High horizontal flow	Same	5.00×10^{-8}	10.77	2.82
6	Low horizontal flow	Different	2.33×10^{-10}	10.77	3.63
7	Medium horizontal flow	Different	1.89×10^{-8}	4.31	3.63
8	High horizontal flow	Different	5.00×10^{-8}	10.77	2.82
9	Low vertical*** flow	Same	2.33×10^{-10}	10.77	-
10	Medium vertical flow	Same	1.89×10^{-8}	10.77	3.63
11	High vertical flow	Same	5.00×10^{-8}	13.76	-
12	Low vertical flow	Different	2.33×10^{-10}	10.77	-
13	Medium vertical flow	Different	1.89×10^{-8}	10.77	3.63
14	High vertical flow	Different	5.00×10^{-8}	13.76	-

* Porosity and water retention curve parameters of the rock and vault materials are given in Table 2-2.

** "Same" and "different" mean that the water retention curves of the waste and backfill are assumed to be the same and different, respectively.

*** Groundwater vertical flow is downwards in cases 9 to 14.

4.1.1 Hydrostatic conditions

Figure 4-3 shows the liquid pressure distributions obtained after 1 000 years in Case 1 and Case 2 (see Table 4-2). The initial liquid pressure distribution is independent from the water retention curve because the system is water saturated. As the gas is generated and released from the vault, it could affect the groundwater pressure field. The distribution of gas within the vault depends on the water retention curves of the different materials, as explained later. If the gas generation rates would be high enough, a contrast of water retention properties could affect the liquid pressure, especially within and around the BHK vault. However, the results show that the difference in the water retention curves between the waste and the backfill does not impact the groundwater pressure field. This is because the simulated hydrogen generation rates (see Table 2-1 and Equation 2-28) cause relatively small gas saturations (see, e.g., Figure 4-7). These gas saturations are not sufficiently high to have an appreciable impact on the water pressure field. Thus, water flow is close to quasi-stationary throughout the entire simulation.

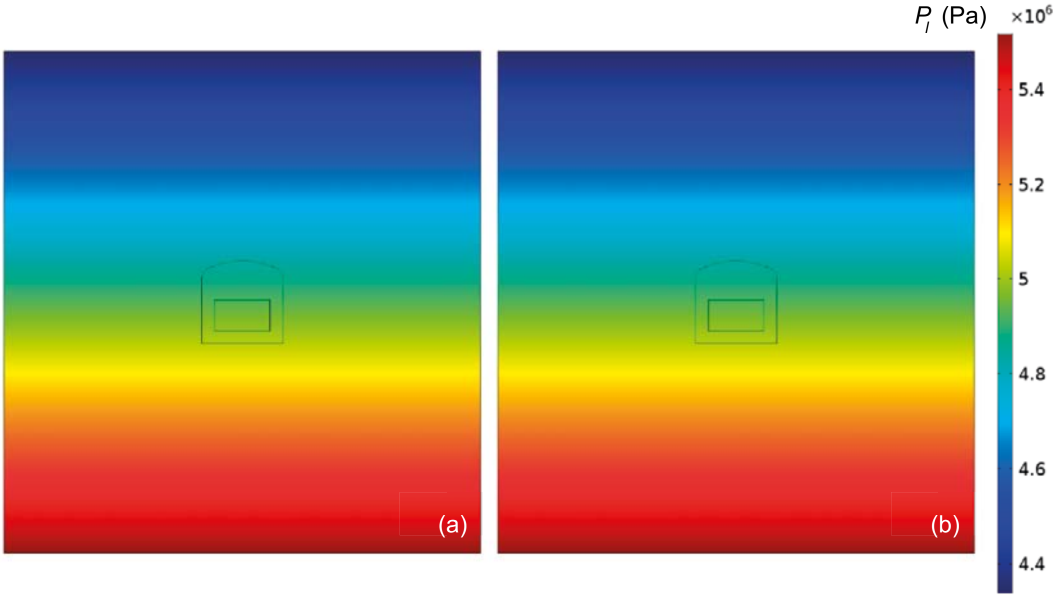

Figure 4-3. Water pressure distribution obtained under hydrostatic conditions at 1 000 years for: (a) Case 1 and (b) Case 2.

The evolution of the gas saturation distribution is shown in Figure 4-4 through Figure 4-9. During the first 100 years, the gas generated in the waste evolves within the BHK vault. After that time the gas reaching the rock starts to migrate upwards due to buoyancy and the relatively high rock permeability (see Table 4-1). In the backfill above the waste compartment hydrogen gas continues flowing to the top at lower velocities than the gas velocities in the surrounding rock (see Figure 4-10). After a period that ranges between 130 and 3 000 years the gas has spread almost through the entire vault (see Figure 4-6 and Figure 4-7). The maximum saturation of gas is about 1.8 % (see, e.g., top in Figure 4-7) and 2.3 % when the waste and backfill have different water retention curves (see, e.g., bottom in Figure 4-7). A steady-state flow is reached after approximately 500 years, due to the relatively high rock permeability.

When the water retention curves of the backfill and the waste are the same the gas produced in the waste distributes uniformly within the vault (see, e.g., Figure 4-8 at *t* = 74 900 years). In contrast, when the water retention curves of the waste and backfill are different, the gas accumulates in the top backfill. Also, this difference in the water retention curves causes a faster gas release (see, e.g., Figure 4-5 at *t* = 100 years).

Both carbon and stainless steel corrosion proceed during the first 74 920 years. After this time, the hydrogen generation rate reduces to the corresponding value of carbon steel corrosion (see Equation 2-28 and Table 2-1). This reduces the gas pressures in the vault and the gas saturation decreases accordingly (compare the gas saturation distributions at 1 000 and 615 000 years shown in Figure 4-7 and Figure 4-8, respectively).

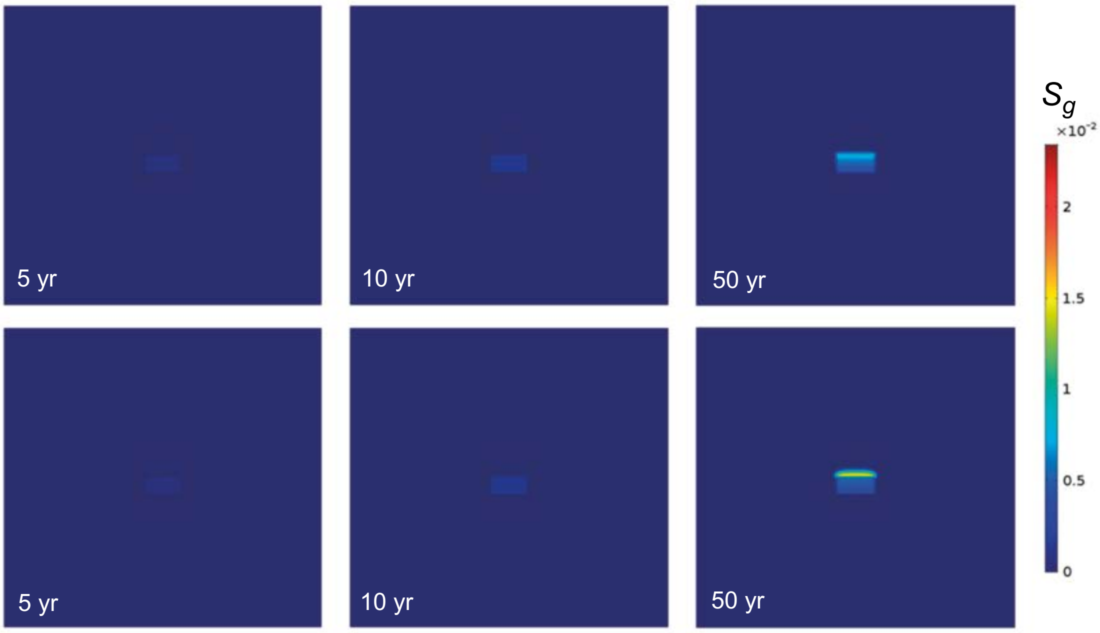

Figure 4-4. *Gas saturation at 5, 10 and 50 years for (top) Case 1 and (bottom) Case 2.*

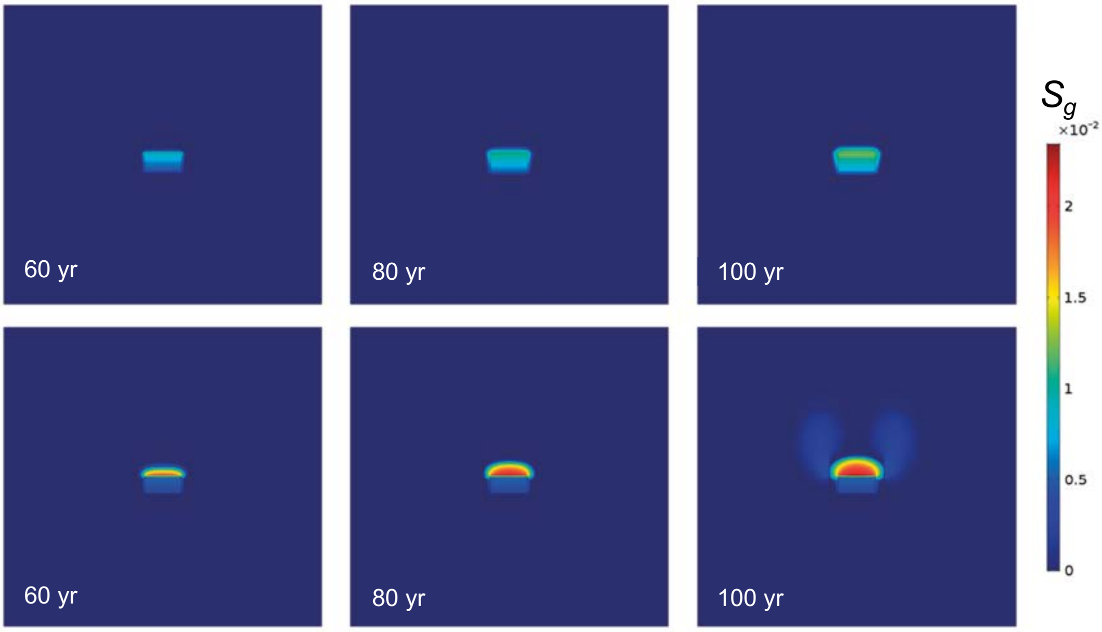

Figure 4-5. *Gas saturation at 60, 80 and 100 years for (top) Case 1 and (bottom) Case 2.*

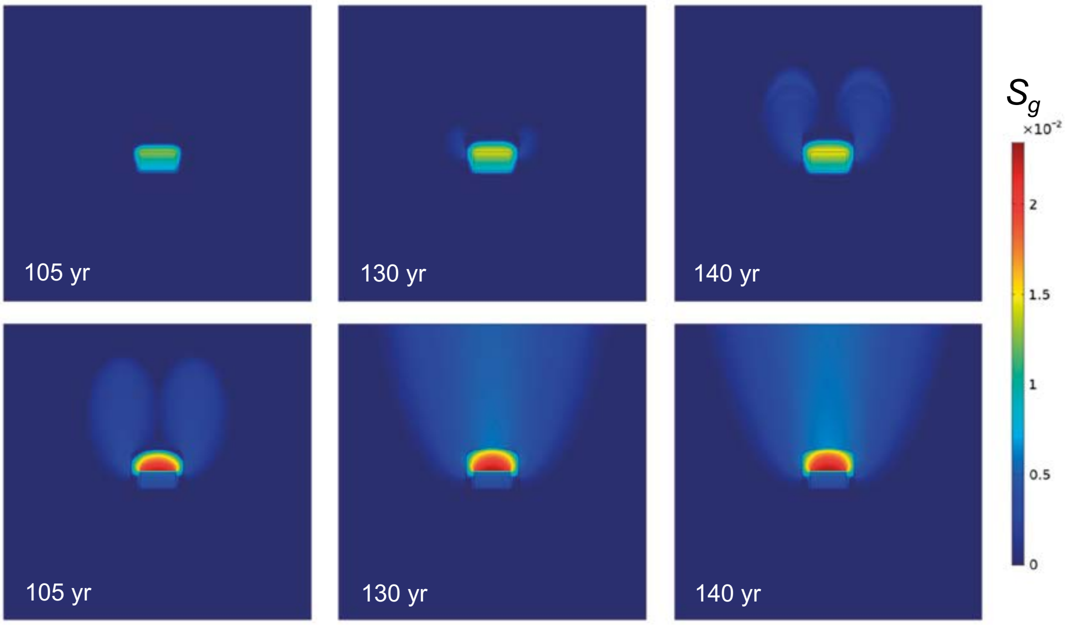

Figure 4-6. *Gas saturation at 105, 130 and 140 years for (top) Case1 and (bottom) Case 2.*

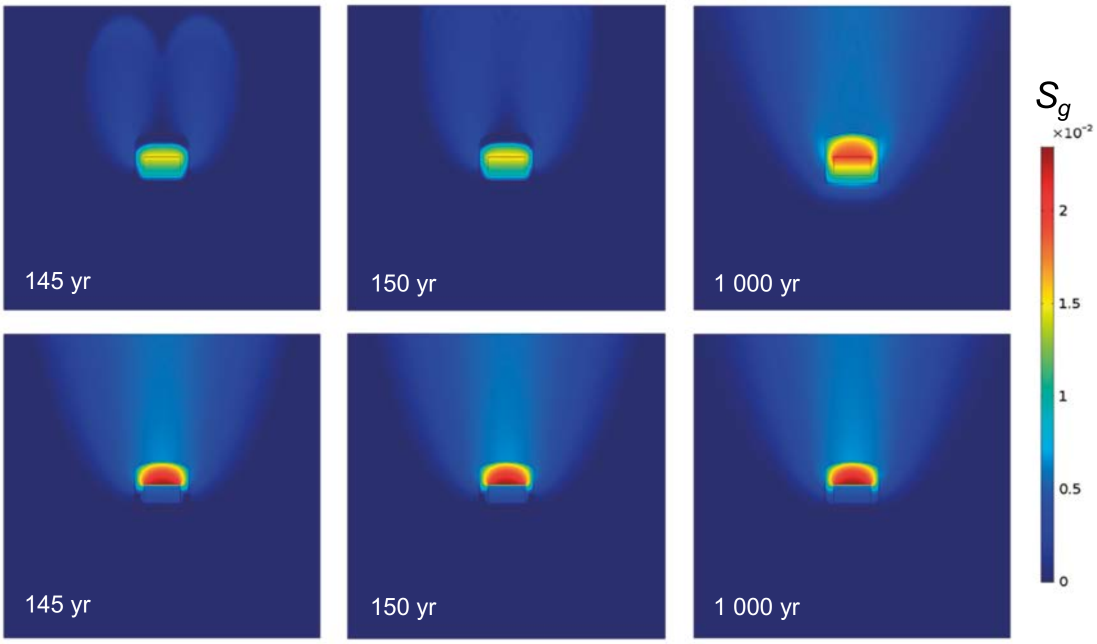

Figure 4-7. *Gas saturation at 145, 150 and 1 000 years for (top) Case 1 and (bottom) Case 2.*

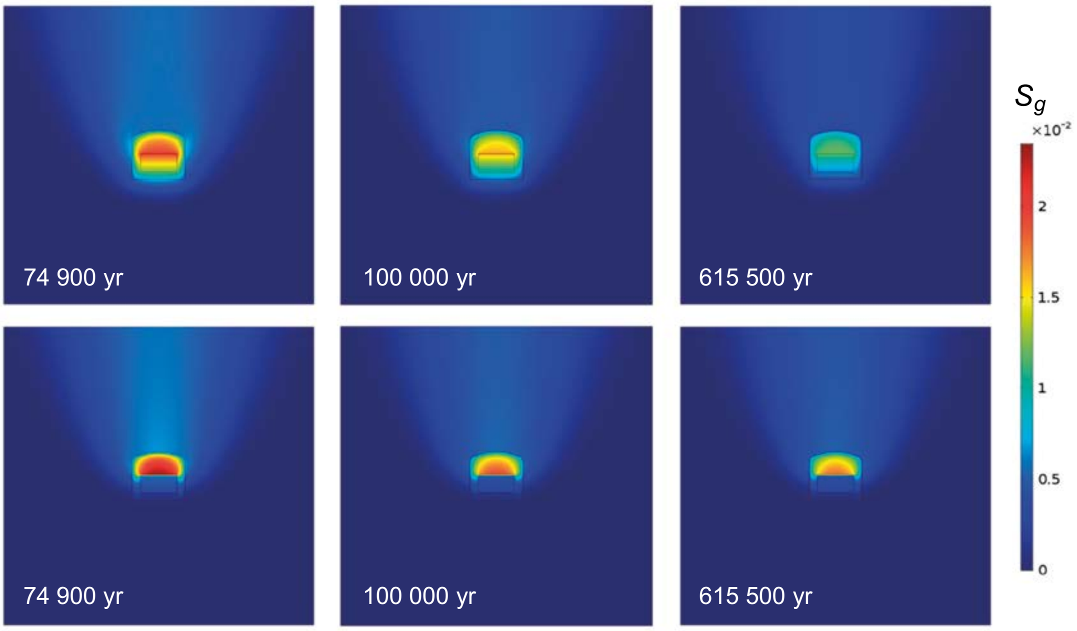

Figure 4-8. *Gas saturation at 74 900, 100 000 and 615 500 years for (top) Case 1 and (b) Case 2.*

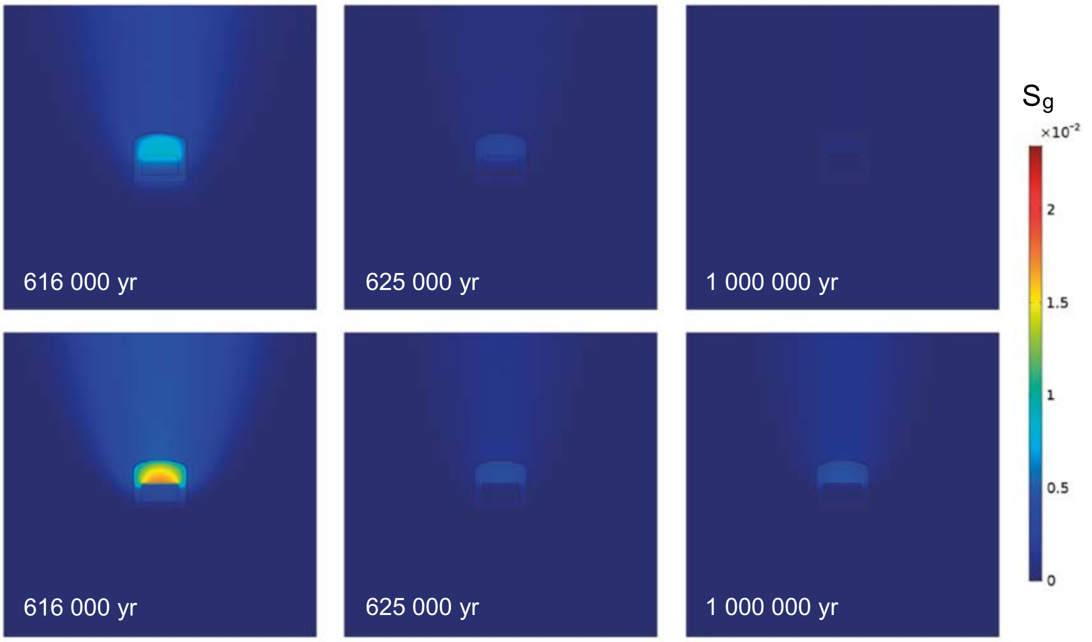

Figure 4-9. *Gas saturation at 616 000, 625 000 and 1 000 000 years for (top) Case 1 and (bottom) Case 2.*

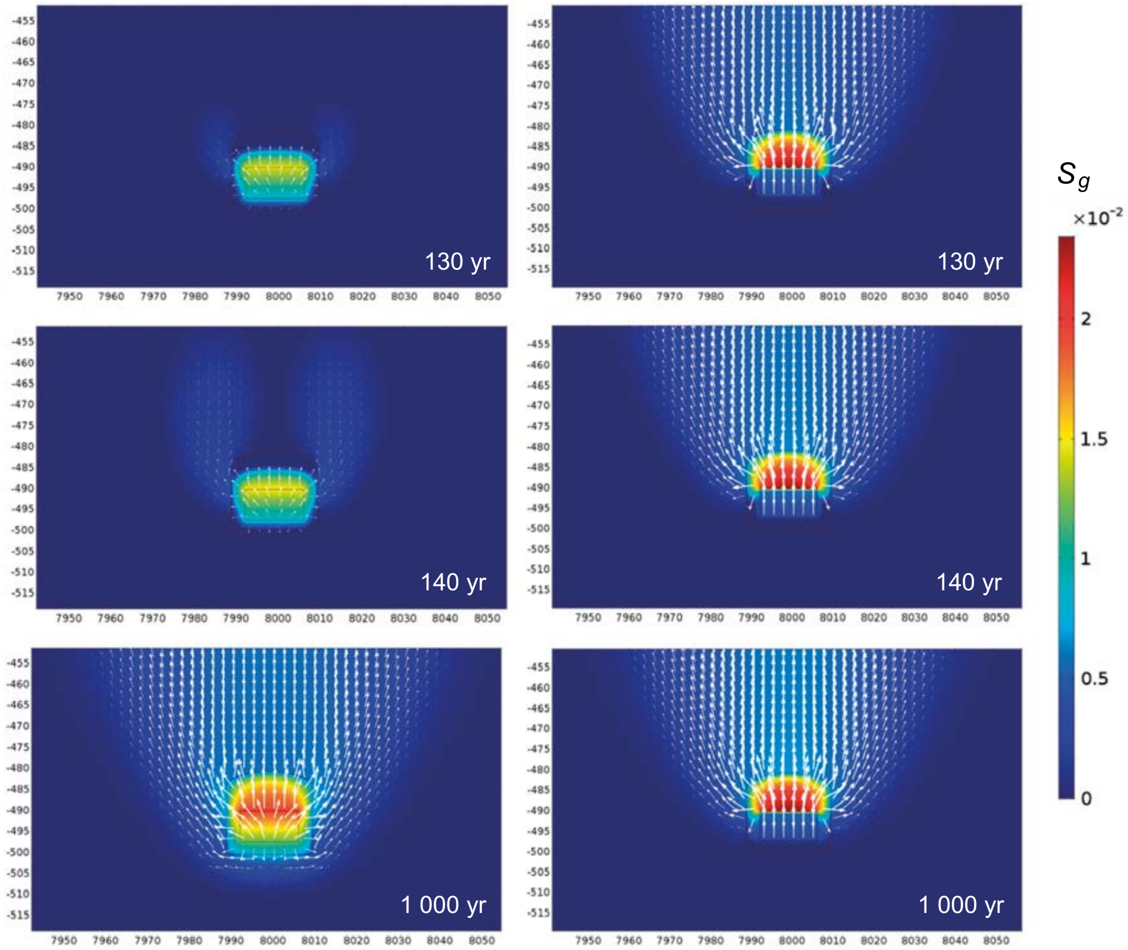

Figure 4-10. *Gas saturation and Darcy flux vector of the gas phase (white arrows) around the BHK vault at 130, 140 and 1 000 years for (left) Case 1 and (right) Case 2.*

Figure 4-11a shows the evolution of the computed gas pressure at 6 observation points. These plots reflect mainly the hydrogen generation rates due to the corrosion of two types of steel. They also show the effect of the hydrogen migration through and around the BHK vault on local gas pressures. Note that because of the relatively high release of hydrogen from the vault and relatively high permeabilities of the waste and rock, the pressure increase around the BHK vault is about 1.5 to 2.5 bar and stabilizes at a plateau value. Once the stainless steel is completely corroded, the gas pressure decreases in response to the reduced gas generation rate.

The average gas pressure in the BHK vault in each case is shown in Figure 4-11b. Case 1 results in gas pressures and overpressures that are higher than in Case 2. In the latter, however, the pressures can be significantly higher locally, especially in the top of the backfill (compare red and cyan lines in Figure 4-11a). In the very long term, there is a small amount of gas retained in this part of the vault (see Figure 4-9 at *t* = 1 000 000 years).

Finally, the maximum gas overpressure is on the order of 1.5 to 2.4 bar, and is reached when both stainless and carbon steel corrode (Figure 4-12). After the complete corrosion of stainless steel, the overpressure decreases by approximately 0.2 bar. When corrosion stops, the overpressure decreases significantly, approaching 0.2 bar after 1 000 000 years.

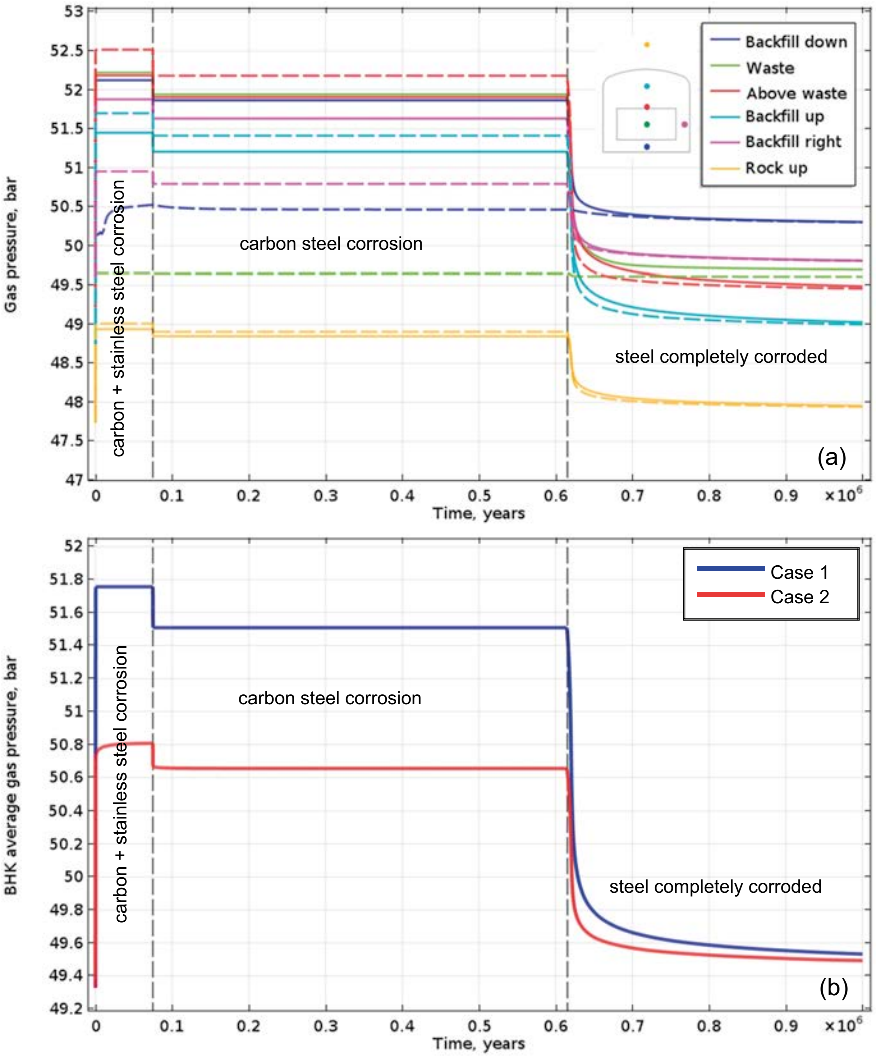

Figure 4-11. *Evolution of (a) the gas pressure at 6 observation points distributed in and around the BHK vault (solid lines for Case 1, dashed lines for Case 2) and (b) the average gas pressure in the BHK.*

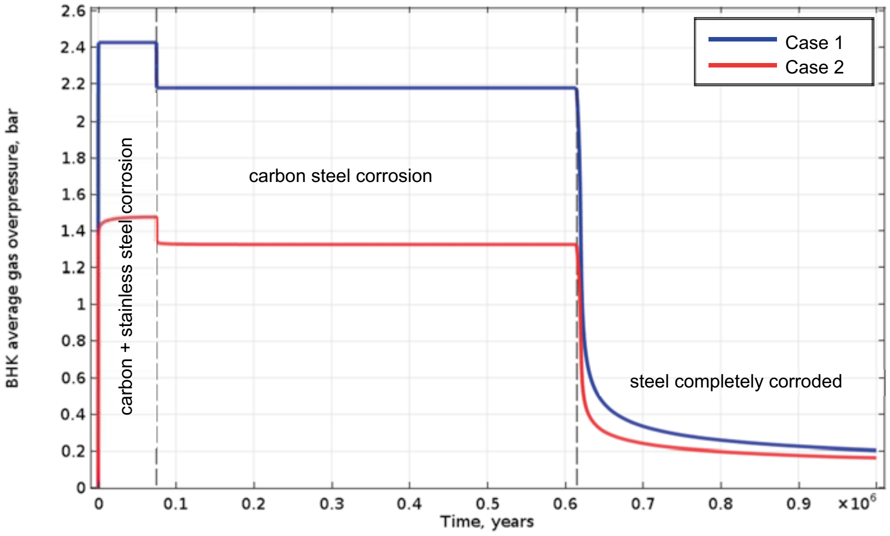

***Figure 4-12.** Evolution of the average overpressure in the BHK vault caused by gas generation.*

4.1.2 Horizontal flow

The second groundwater flow condition considers horizontal flow. The distribution of the liquid pressure and the Darcy velocity fields obtained after 1 000 years are shown in Figure 4-13. When the horizontal flow is small, the gravitational forces dominate over the pressure gradient. As a consequence, the system is near hydrostatic conditions (compare Figure 4-13a and Figure A-1a, or Figure 4-13e and Figure A-1b). Images (a) through (c) in Figure 4-13 show the computed results when the water retention curves of the waste and backfill are the same. Images (d) through (f) in Figure 4-13 show the computed results when the water retention curves are different. No major differences are observed.

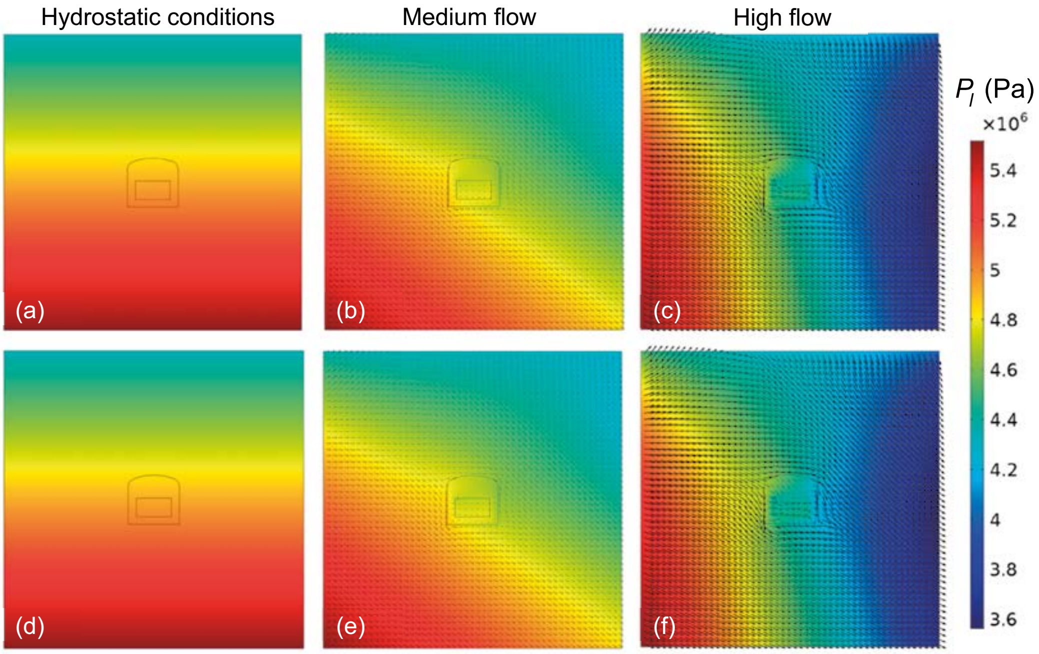

***Figure 4-13.** Water pressure distribution and groundwater Darcy flux vector obtained at 1 000 years for horizontal groundwater flow, when the water retention curves of the waste and the backfill are (top) the same and (bottom) different: (a) Case 1, (b) Case 4, (c) Case 5, (d) Case 2, (e) Case 7, (f) Case 8.*

Figure 4-14 to Figure 4-17 show the evolution of the gas saturation. During the first 100 years and for low groundwater flow, the gas generated in the waste evolves within the BHK vault. Groundwater flow causes the gas to move horizontally. Compared to the hydrostatic field (Cases 1 and 2) gas reaches the right-side wall of the vault relatively early and the top of the backfill relatively late. For medium and high groundwater flow conditions the gas mainly accumulates in the top-right part of the vault. Analogously to the hydrostatic field, within the top of the backfill, gas flows upwards at a velocity lower than the gas velocities developed in the surrounding rock (see Figure 4-18). The reason for this is that the rock permeability is slightly higher than the permeability of the backfill (see Table 4-1). Thus, gas fills the vault at later times, in this case after 1 000 years for low and medium flow conditions. For high groundwater flow the gas does not fill the vault completely. The internal gas pressures of the vault also dissipate quickly. However, the reduction of gas buoyancy forces due to high horizontal groundwater flow lead to higher gas saturations within the vault. This effect is pronounced when the water retention curves of the waste and the backfill are different (see, e.g., Figure 4-15 and Figure 4-16). The maximum gas saturation is about 3.5 % for high flow conditions (Figure 4-16f). The reduction of the gas production rate decreases the gas pressures in the vault. This in turn leads to a decrease in the gas saturation after 74 920 years (compare the gas saturation distributions at 1 000 and 615 500 years shown in Figure 4-16 and Figure 4-17).

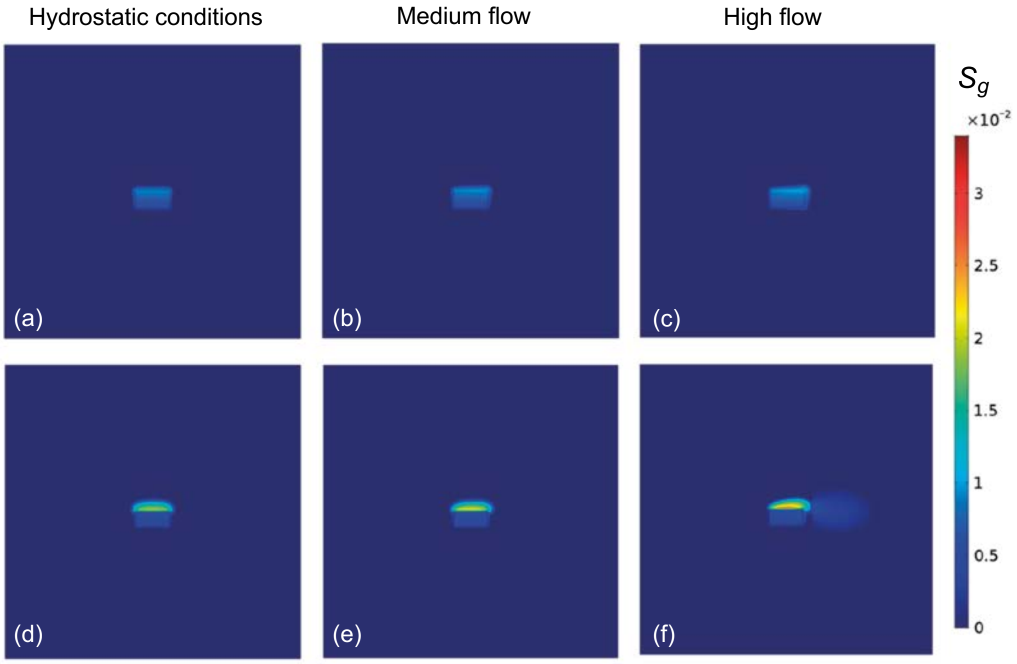

***Figure 4-14.** Gas saturation distribution obtained at 65 years for horizontal groundwater flow, when the water retention curves of the waste and the backfill are (top) the same and (bottom) different: (a) Case 1, (b) Case 4, (c) Case 5, (d) Case 2, (e) Case 7, (f) Case8.*

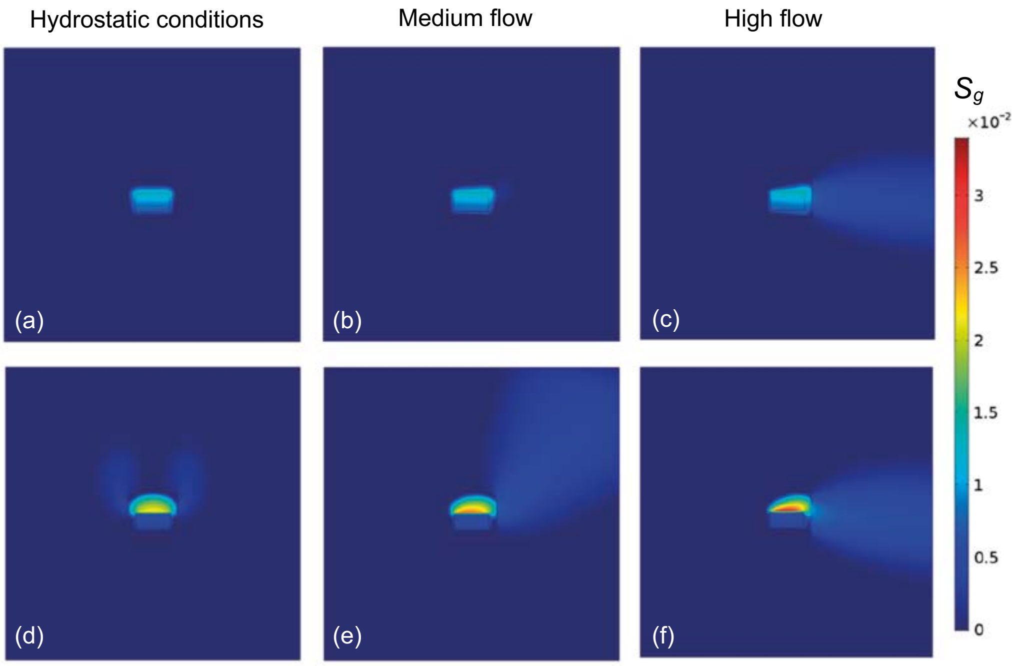

__Figure 4-15.__ Gas saturation distribution obtained at 100 years for horizontal groundwater flow, when the water retention curves of the waste and the backfill are (top) the same and (bottom) different: (a) Case1, (b) Case 4, (c) Case 5, (d) Case 2, (e) Case 7, (f) Case 8.

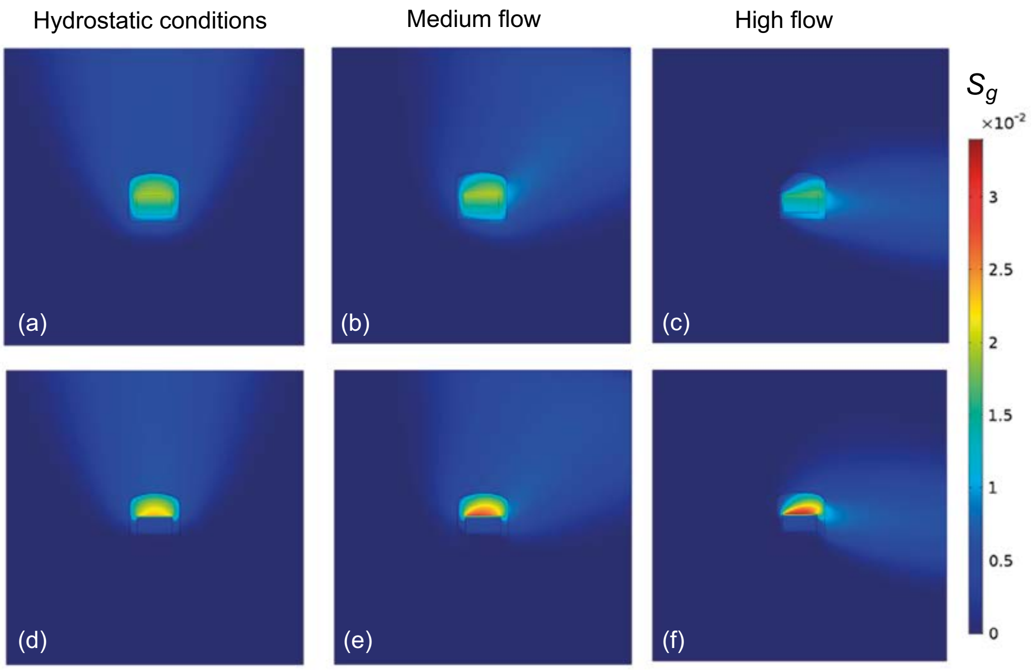

__Figure 4-16.__ Gas saturation distribution obtained at 1 000 years for horizontal groundwater flow, when the water retention curves of the waste and the backfill are (top) the same and (bottom) different: (a) Case 1, (b) Case 4, (c) Case 5, (d) Case 2, (e) Case 7, (f) Case 8.

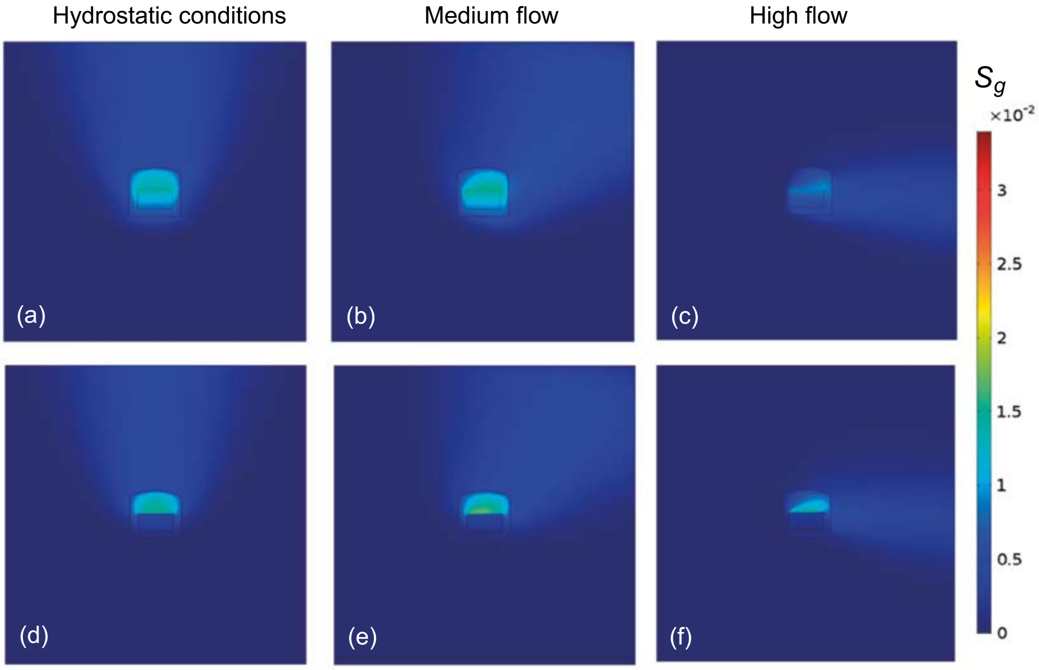

***Figure 4-17.** Gas saturation distribution obtained at 615 500 years for horizontal groundwater flow, when the water retention curves of the waste and the backfill are (top) the same and (bottom) different: (a) Case 1, (b) Case 4, (c) Case 5, (d) Case 2, (e) Case 7, (f) Case 8.*

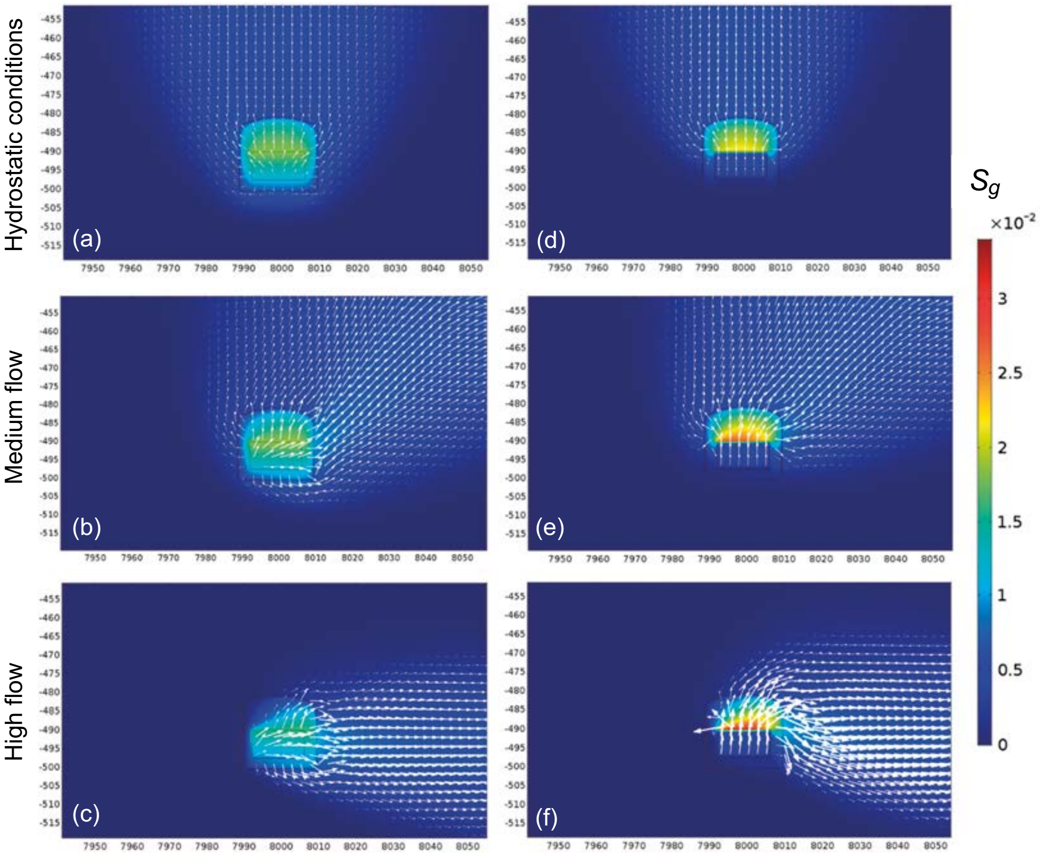

***Figure 4-18.** Gas saturation and Darcy flux vector of the gas phase (white arrows) around the BHK vault at 74 900 years for horizontal groundwater flow, when the water retention curves of the waste and the backfill are (left) the same and (right) different: (a) Case 1, (b) Case 4, (c) Case 5, (d) Case 2, (e) Case 7, (f) Case 8.*

Horizontal groundwater flow also increases the gas release, especially for high water flow. For medium groundwater flow the gas flows laterally upwards (see Figure 4-15b and e, Figure 4-16b and e, Figure 4-18b and e). For high water flow conditions, the gas flow becomes nearly horizontal. The gas flow even has a downward component, (see Figure 4-15c and f, Figure 4-16c and f, Figure 4-18c and f) due to the water pressure distribution (Figure 4-13c and f).

As in the hydrostatic case (Case 2), different water retention curves for the waste and the backfill induce a faster release of gas from the vault. It can be concluded that under horizontal groundwater flow conditions, buoyancy and capillary forces act in the same direction, contributing to a more efficient gas release.

As shown in Figure 4-19 for Case 8, the groundwater flow field is not affected by gas generation in the BHK vault. For low groundwater flow the pressure field is like the pressure field obtained under hydrostatic conditions (compare Figure 4-13a and d with Figure A-1a and b, respectively). Consequently, there is no significant effect on the gas release and the overpressure is not affected. In contrast, for medium and high flow conditions, horizontal fluxes disturb the gas buoyancy, driving gas to the right and away from the vault. This reduces the average gas pressure in the vault. As shown in Figure 4-20, a maximum pressure decrease of about 2 bar is computed for medium flow conditions, compared the hydrostatic situation. Meanwhile, a difference of 5.3 bars is found for high flow conditions. Note that the water flux ratio $5.00 \times 10^{-8}/1.89 \times 10^{-8} \approx 2.65$, is consistent with the corresponding pressure reduction ratio, which is $5.3/2 \approx 2.65$. Moreover, the gas overpressure in the BHK vault decreases as the groundwater flux increases (Figure 4-21). However, overpressures are not affected significantly by the groundwater flux, especially when the water retention curves of the waste and the backfill are different (Figure 4-21b).

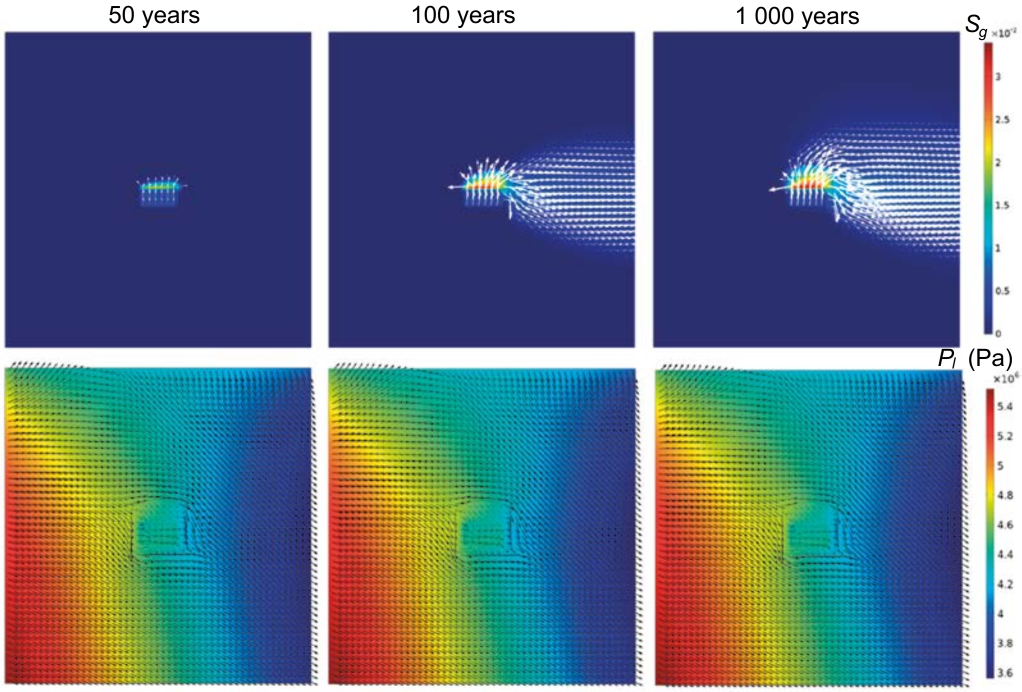

Figure 4-19. *Impact of gas production and migration on groundwater flow for high horizontal groundwater flow, when the water retention curves of the waste and the backfill are different (Case 8): (top) S_g and $\mathbf{q}_g$, (bottom) P_l and $\mathbf{q}_l$ at 50 years, 100 years and 1 000 years.*

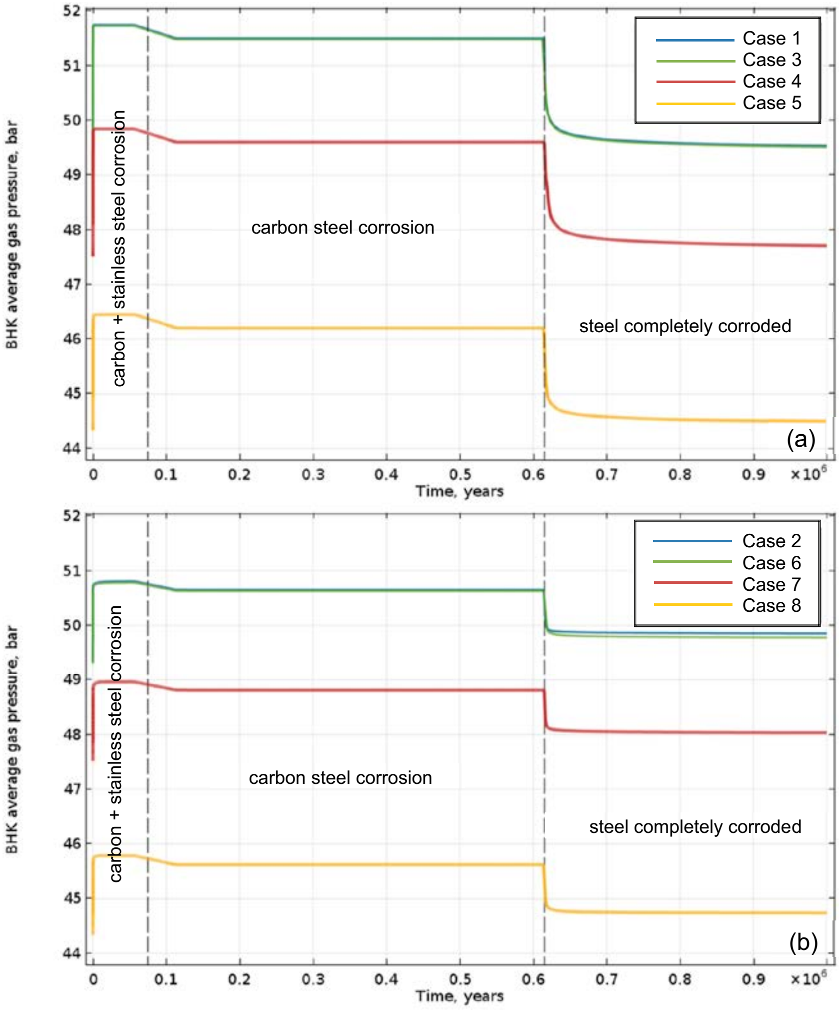

Figure 4-20. *Evolution of the average gas pressure under horizontal groundwater flow when the water retention curves of the waste and backfill: (a) are the same (Cases 3, 4 5) and (b) different (Cases 6, 7, 8), compared to hydrostatic flow conditions (Cases 1 and 2).*

Finally, Figure 4-21 suggests that capillary forces contribute to reduce the overpressure in 1.0 bar during the gas generation period. However, in the long-term capillarity has a detrimental effect, as the overpressure is about 0.25 bar higher than when the waste and backfill have the same water retention curve. As with hydrostatic conditions (Case 2), this higher overpressure is due to the gas being trapped in the top of the backfill for longer periods.

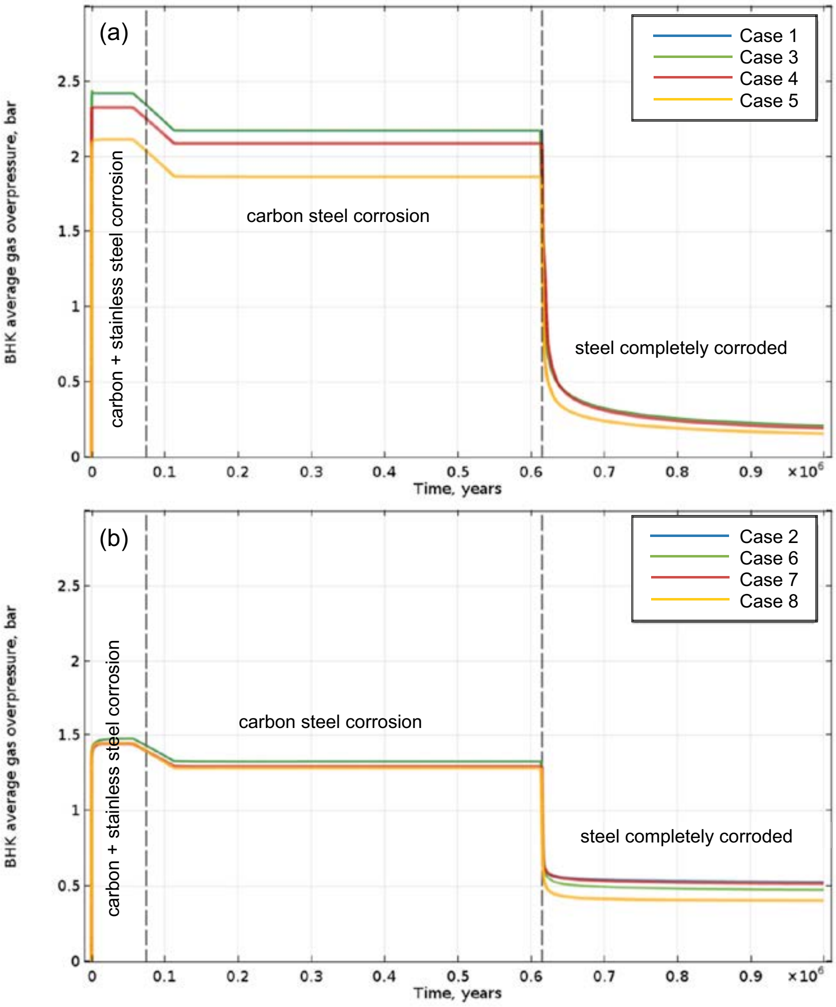

Figure 4-21. *Evolution of the average overpressure under horizontal groundwater flow when the water retention curves of the waste and backfill: (a) are the same (Cases 3, 4, 5) and (b) different (Cases 6, 7, 8), compared to hydrostatic flow conditions (Cases 1 and 2).*

4.1.3 Vertical downwards flow

The third groundwater flow condition considers vertical downward groundwater flow. Like in the horizontal flow condition, for low groundwater flow gravity dominates over the pressure gradient. Thus, the vault and the near-field are very close to hydrostatic conditions (compare Figure 4-22a and Figure A-4b, or Figure 4-22d and Figure A-4b). The distributions of liquid pressure and Darcy's flux fields obtained after 1 000 years are shown in Figure 4-22. Again, these results show that assuming different water retention curves for the waste and the backfill has no appreciable impact on the water flow. This is due to the low hydrogen production rates, which lead to gas saturations below 3.5 % in the entire system. Note that for this gas saturation, the relative permeability of water is close to 1.0 (see Figure 2-6b).

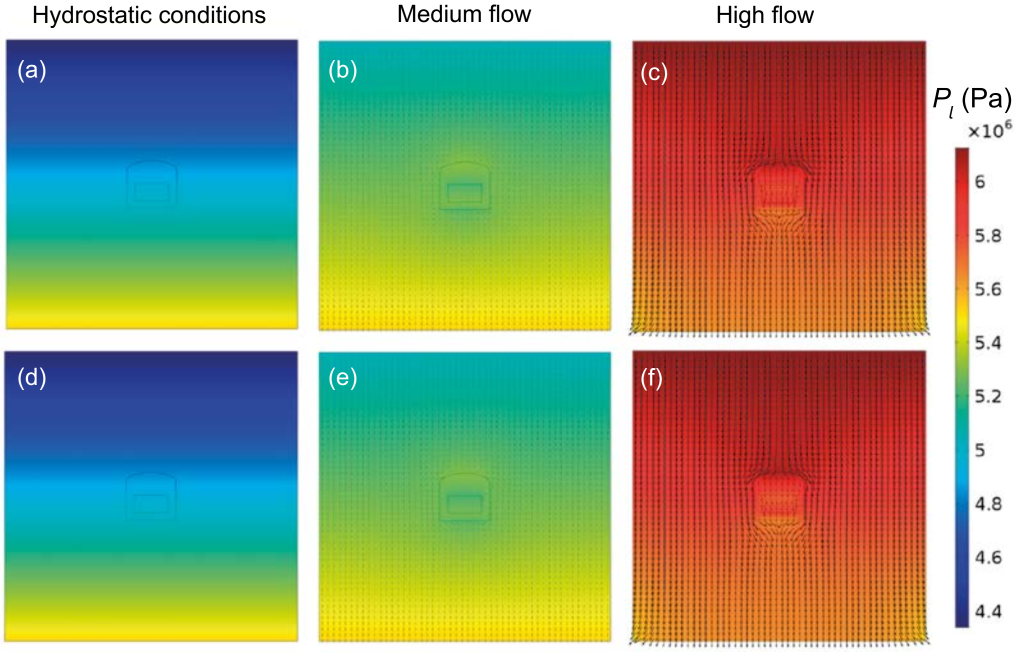

***Figure 4-22.** Water pressure distribution and groundwater Darcy flux vector obtained at 1 000 years for vertical downwards groundwater flow, when the water retention curves of the waste and the backfill are (top) the same and (bottom) different: (a) Case 1, (b) Case 10, (c) Case 11, (d) Case 2, (e) Case 13, (f) Case 14.*

The evolution of gas saturation is shown in Figure 4-23 to Figure 4-26. For low flow conditions, the gas flow behavior is similar to the one computed under hydrostatic conditions -compare, e.g., Figure 4-25a and Figure A-5 (bottom, 1 000 years). However, after complete corrosion of the steel in the waste, some differences are established between both cases. Figure 4-26 suggests that, for low water flow, and when the water retention curves of waste and backfill are different, the capillarity contributes to overcome gravity and more gas is released (compare Figure 4-26d and bottom of Figure A-5 at 615 500 years). In contrast, capillary forces are reduced when the water retention curves of the waste and the backfill are the same. The downward flow of water then traps more gas in the vault (compare Figure 4-26a and top of Figure A-5 at 615 500 years).

This delay in the gas buoyancy is also found during the steel corrosion period for medium flow conditions. The gas flow is substantially delayed when the water retention curves of the waste and the backfill are the same, as shown in Figure 4-24. After 100 years, the gas crossing the interface between the bottom of the vault and the surrounding rock is driven downwards by the groundwater flow. Although the gas produced within the waste compartment covers the whole BHK vault after 1 000 years, gas spreads laterally (see, e.g., Figure 4-25b and e). For high flow conditions the gas buoyancy is completely counteracted by the downwards flow of water. Consequently, the gas released from the vault migrates to the bottom of the rock domain (Figure 4-24c and f, Figure 4-25c and f). This dominance of groundwater flow over gas buoyancy contributes to maintain gas pressures relatively higher than those obtained under other groundwater flow conditions, as it is commented later.

The rapid dissipation of internal gas pressures in the vault limits the gas saturation increase to a maximum value of about 3.5 %. This saturation is obtained when the water retention curves of the waste and the backfill are different (see Figure 4-24f and Figure 4-25f). The gas pressures that develop in and around the vault are also notably higher under these conditions (compare Figure 4-20 and Figure 4-29). This is because the produced gas is forced by the water flow to stay below the top of the vault. Again, because of the reduction in the hydrogen generation rate after 74 920 years, the gas saturation decreases (compare the gas saturation distributions at 1 000 and 615 500 years shown in Figure 4-25 and Figure 4-26).

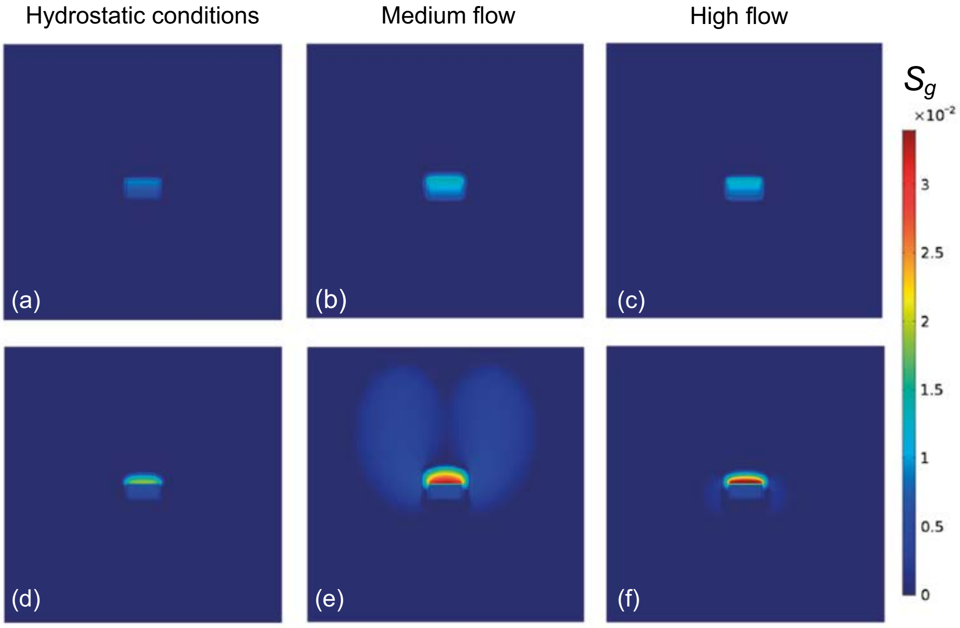

***Figure 4-23.** Gas saturation distribution obtained at 65 years for vertical downwards groundwater flow, when the water retention curves of the waste and the backfill are (top) the same and (bottom) different: (a) Case 1, (b) Case 10, (c) Case 11, (d) Case 2, (e) Case 13, (f) Case 14.*

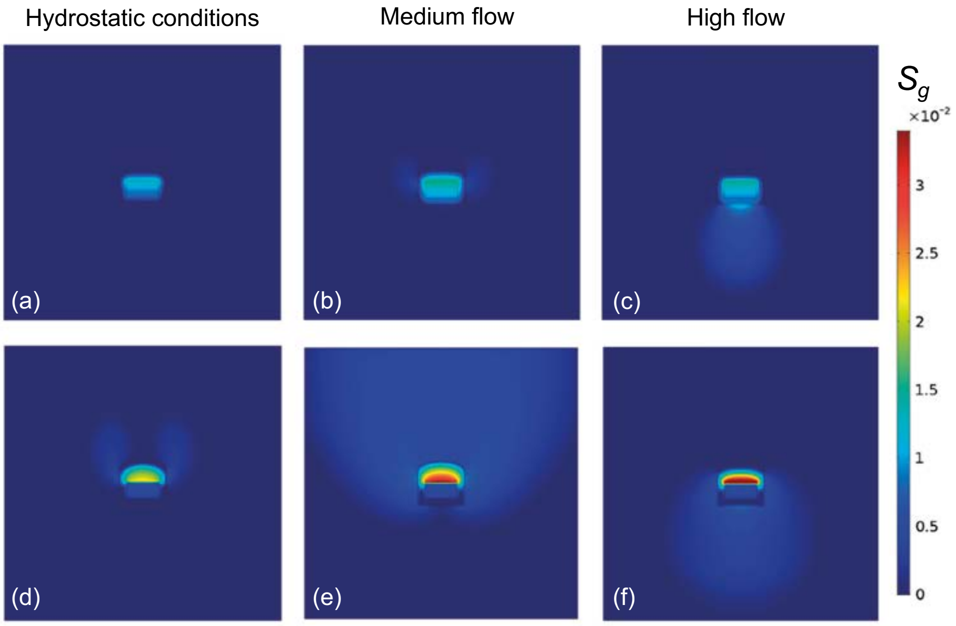

***Figure 4-24.** Gas saturation distribution obtained at 100 years for vertical downwards groundwater flow, when the water retention curves of the waste and the backfill are (top) the same and (bottom) different: (a) Case 1, (b) Case 10, (c) Case 11, (d) Case 2, (e) Case 13, (f) Case 14.*

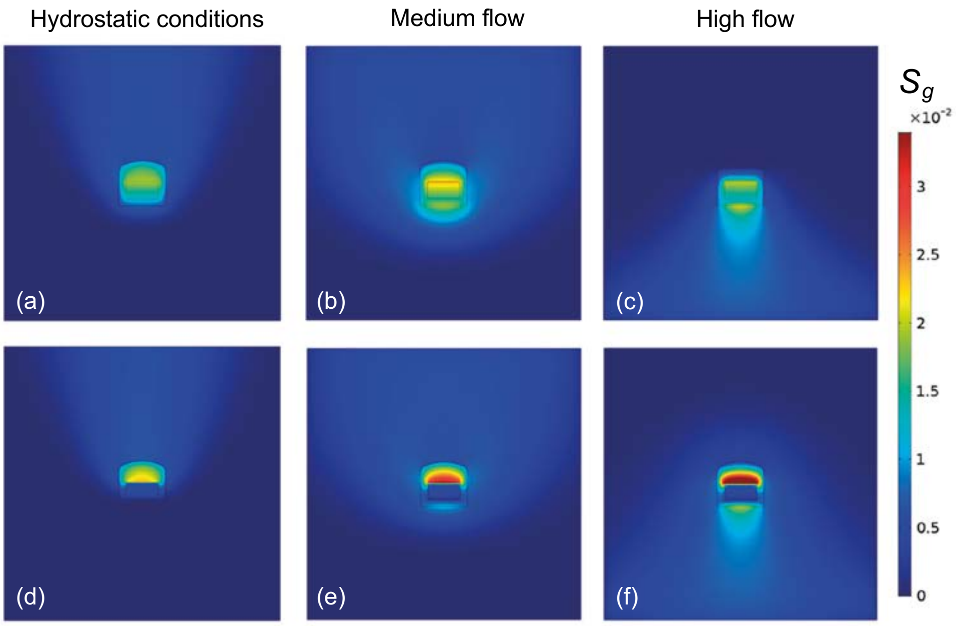

***Figure 4-25.** Gas saturation distribution obtained at 1 000 years for vertical downwards groundwater flow, when the water retention curves of the waste and the backfill are (top) the same and (bottom) different: (a) Case 1, (b) Case 10, (c) Case 11, (d) Case 2, (e) Case 13, (f) Case 14.*

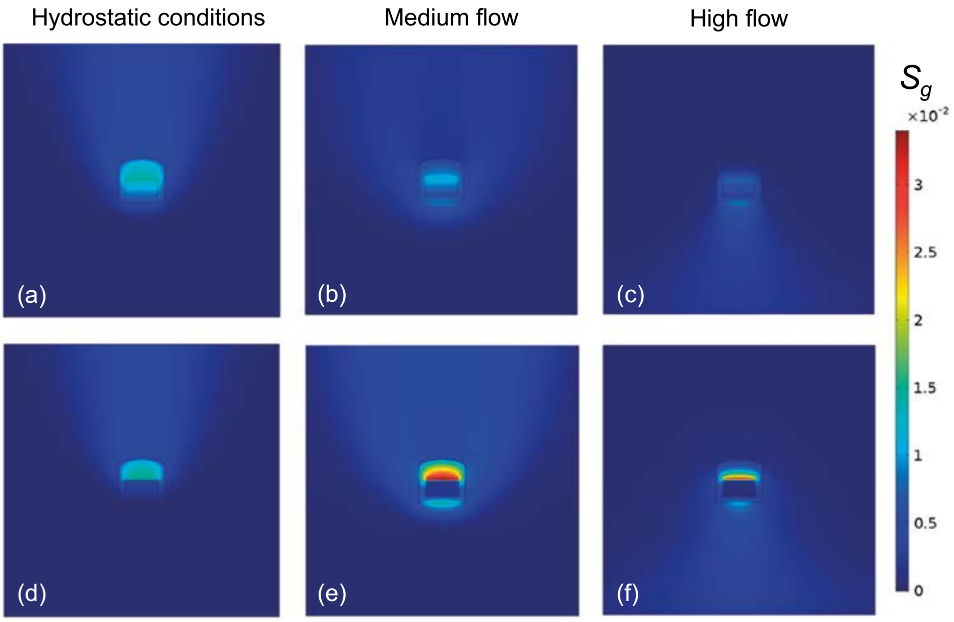

***Figure 4-26.** Gas saturation distribution obtained at 615 500 years for vertical downwards groundwater flow, when the water retention curves of the waste and the backfill are (top) the same and (bottom) different: (a) Case 1, (b) Case 10, (c) Case 11, (d) Case 2, (e) Case 13, (f) Case 14.*

The gas pressures developing in the vault under vertical flow are considerably higher than under hydrostatic or horizontal groundwater flow conditions. This is because the gas accumulated at the top of the backfill is pushed downwards by the flow of water. These counter current flows developed around the vault contribute to increase the internal gas pressure as well as the gas pressures in the surrounding rock. This situation is depicted in Figure 4-27 and Figure 4-28 where the Darcy fluxes of the gas and liquid phases are represented by white and black arrows, respectively. The effect of assuming different water retention curves for waste and backfill on gas flow becomes clear when comparing Figure 4-27b and Figure 4-27e (medium flow conditions). Comparing Figure 4-27c and Figure 4-27f demonstrates that high groundwater flow conditions control the flow of gas.

The water flow field is nearly unaffected by gas generation and migration. Figure 4-28 shows the evolution of the pressure and Darcy's flux fields of liquid during the first 1 000 years obtained in Case 14 (high water flow and different water retention curves in the waste and the backfill).

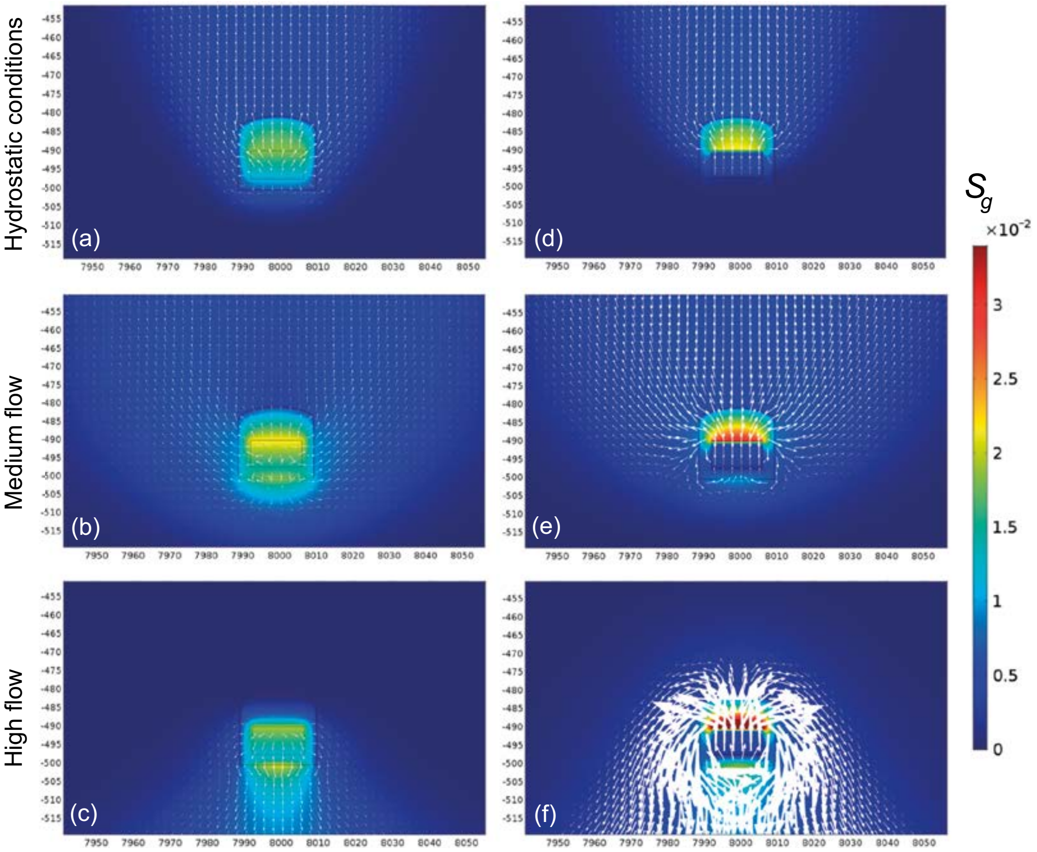

Figure 4-27. *Gas saturation and Darcy flux vector of the gas phase (white arrows) around the BHK vault at 74 900 years for vertical downwards water flow, when the water retention curves of the waste and the backfill are (top) the same and (bottom) different: (a) Case 1, (b) Case 10, (c) Case 11, (d) Case 2, (e) Case 13, (f) Case 14.*

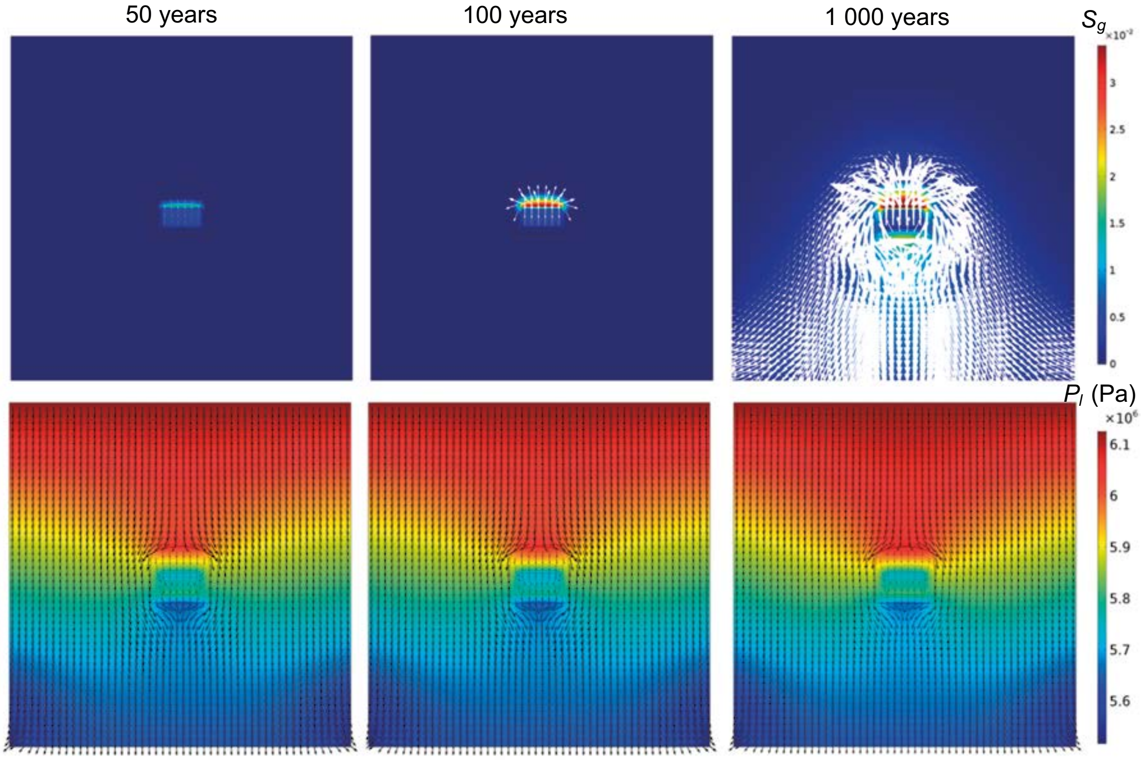

Figure 4-28. *Impact of gas production and migration on groundwater flow under high vertical downwards groundwater flow, when the water retention curves of the waste and the backfill are different (Case 14): (top) S_g and $\mathbf{q}_g$, (bottom) P_l and $\mathbf{q}_l$ at 50 years, 100 years and 1 000 years.*

The downward groundwater flow increases the pressure in the vault. The buoyancy and capillary forces act in opposite direction. This can cause overpressures to increase or decrease depending on the magnitude of the groundwater fluxes and the water retention properties of the vault materials. In general, the higher the groundwater flow, the higher the gas pressure increase. A maximum pressure increase of 3.0 bar over the hydrostatic situation is obtained for medium flow conditions (Case 10, see Figure 4-29). Figure 4-29 shows that such an increase is about 9 bar for high groundwater flow conditions.

Low water flow conditions do not affect the gas release from the BHK vault and migration through the host-rock (Cases 9 and 12). In contrast, for medium water flow and the case where the backfill and the waste have the same water retention curve (Case 10), more gas is retained within the vault. This leads to an increase in the overpressure in this case (see Figure 4-30a, red line). For high water flow conditions (Case 11), the gas produced in the vault is also driven downwards. When the water retention curves of the backfill and waste are the same, a significant amount of gas is dragged downwards by the groundwater flow. This causes a decrease of the BHK vault overpressure (see Figure 4-30a, yellow line). This does not occur when the backfill and the waste have different water retention curves (Figure 4-30b). The high amount of gas accumulated in the top of the backfill is pushed down and is kept there, as the capillary flux competes with the gravity forces. Therefore, downward flow causes overpressure to decrease, but capillary forces keep the overpressure high when a contrast of water retention properties exists.

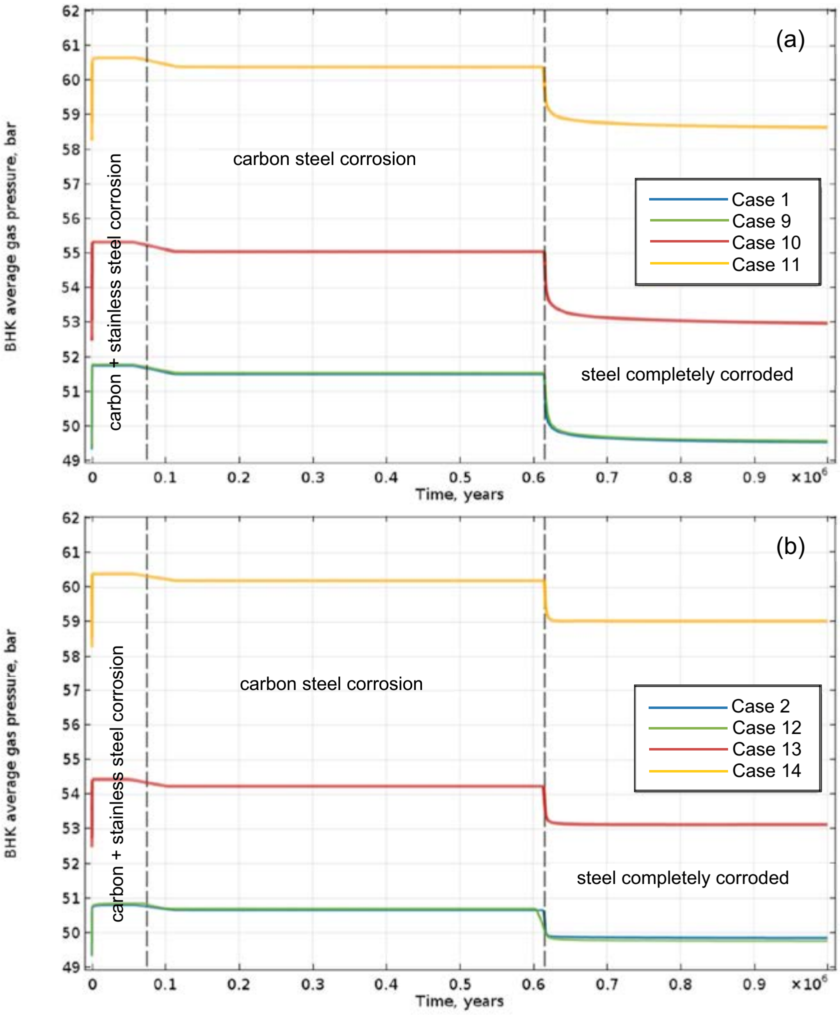

Figure 4-29. *Evolution of the average gas pressure under vertical downwards groundwater flow conditions when the water retention curves of the waste and backfill: (a) are the same (Cases 9, 10, 11) and (b) different (Cases 12, 13, 14), compared to hydrostatic flow conditions (Cases 1 and 2).*

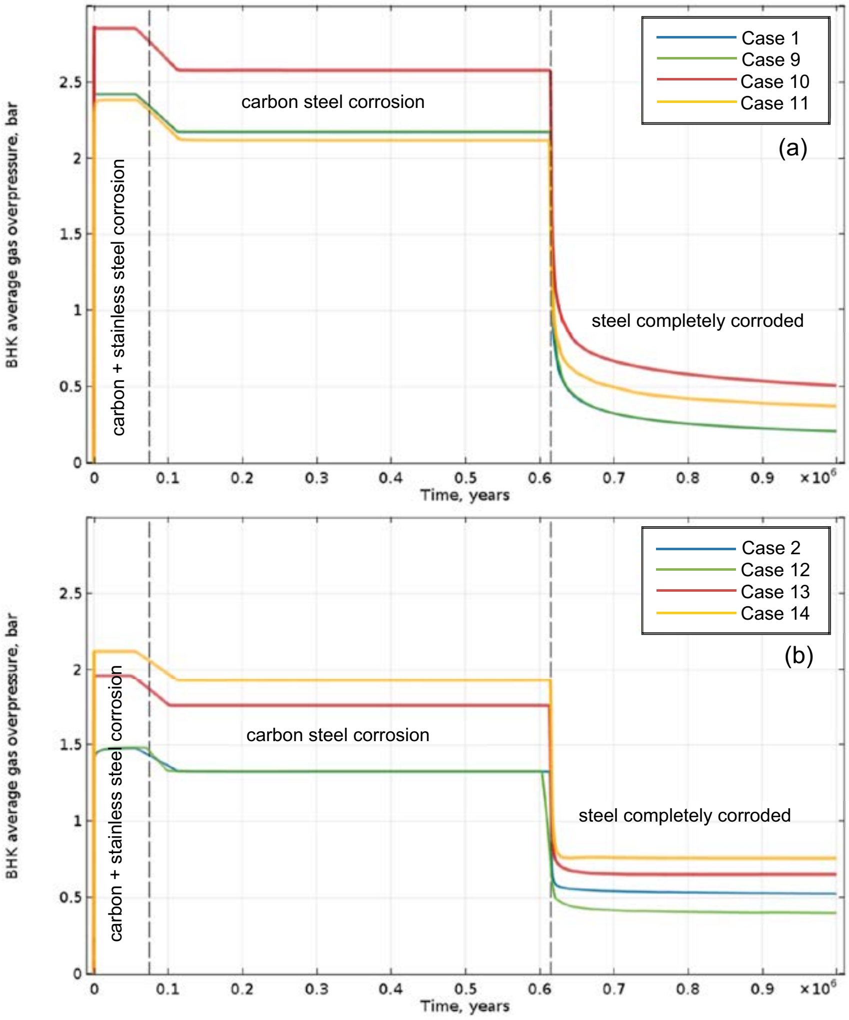

Figure 4-30. *Evolution of the average overpressure under vertical downwards groundwater flow conditions when the water retention curves of the waste and backfill: (a) are the same (Cases 9, 10, 11) and (b) different (Cases 12, 13, 14), compared to hydrostatic flow conditions (Cases 1 and 2).*

4.1.4 Inflow and outflow rates

Table 4-3 summarizes the volumetric inflow and outflow rates to/from the BHK vault and the waste compartment (see Equation 4-2) obtained at 5 different times for each simulation case performed considering homogeneous rock. Note that these flowrates do not represent the actual magnitude of the fluxes (full scale of the vault), as they have been calculated assuming a vault thickness of 1.0 m. Therefore, they are used here only for comparison purposes.

Table 4-3. Volumetric inflow and outflow rates (m^3/year) of water (Q_l) and gas (Q_g) to/from the BHK vault and the waste compartment, simulated considering homogeneous rock.

		BHK vault			Waste compartment		
	Time, years	$Q_{l,in}$	$Q_{l,out}$	$Q_{g,out}$	$Q_{l,in}$	$Q_{l,out}$	$Q_{g,out}$
Case 1	0	0	0	0	0	0	0
	1000	0	0	3.87e−03	0	0	3.50e−03
	74900	0	0	3.21e−03	0	0	2.89e−03
	615000	0	0	2.10e−03	0	0	1.89e−03
	1000000	0	0	1.39e−08	0	0	4.58e−09
Case 2	0	0	0	0	0	0	0
	1000	0	0	3.87e−03	0	0	3.60e−03
	74900	0	0	3.21e−03	0	0	2.98e−03
	615000	0	0	8.86e−04	0	0	6.23e−04
	1000000	0	0	1.25e−05	0	0	1.20e−05
Case 3	0	8.69e−02	8.69e−02	0	1.33e−02	1.33e−02	0
	1000	7.82e−02	7.68e−02	3.95e−03	8.65e−03	8.63e−03	3.55e−03
	74900	7.85e−02	7.72e−02	3.21e−03	8.74e−03	8.76e−03	2.91e−03
	615000	8.08e−02	7.93e−02	4.72e−04	9.74e−03	9.68e−03	3.16e−04
	1000000	8.58e−02	8.45e−02	1.37e−08	1.23e−02	1.24e−02	4.64e−09
Case 4	0	6.78	6.78	0	1.04	1.04	0
	1000	6.19	6.07	4.08e−03	6.97e−01	7.07e−01	3.58e−03
	74900	6.21	6.10	3.35e−03	7.05e−01	7.16e−01	2.95e−03
	615000	6.26	6.15	2.19e−03	7.23e−01	7.34e−01	1.92e−03
	1000000	6.77	6.66	1.55e−08	9.90e−01	1.00	5.27e−09
Case 5	0	18.5	18.5	0	2.78	2.78	0
	1000	16.8	16.5	4.70e−03	1.94	2.02	3.74e−03
	74900	16.9	16.5	3.89e−03	1.96	2.04	3.10e−03
	615000	17.2	16.9	1.25e−03	2.09	2.17	9.00e−04
	1000000	18.5	18.2	1.47e−08	2.66	2.69	6.23e−09
Case 6	0	8.69e−02	8.69e−02	0	1.33e−02	1.33e−02	0
		7.99e−02	7.89e−02	3.87e−03	1.01e−02	1.01e−02	3.61e−03
	74900	7.97e−02	7.86e−02	3.20e−03	1.00e−02	1.00e−02	2.99e−03
	615000	8.07e−02	7.95e−02	1.31e−03	1.03e−02	1.04e−02	1.09e−03
	1000000	8.45e−02	8.32e−02	7.13e−06	1.20e−02	1.22e−02	6.85e−06
Case 7	0	6.78	6.78	0	1.04	1.04	0
	1000	6.28	6.19	4.04e−03	8.14e−01	8.22e−01	3.85e−03
	74900	6.29	6.19	3.35e−03	8.07e−01	8.13e−01	3.19e−03
	615000	6.34	6.24	2.19e−03	8.21e−01	8.28e−01	2.09e−03
	1000000	6.67	6.57	1.72e−05	9.65e−01	9.81e−01	1.66e−05
Case 8	0	18.5	18.5	0	2.78	2.78	0
	1000	16.8	16.5	4.79e−03	2.20	2.29	3.82e−03
	74900	16.8	16.5	3.97e−03	2.19	2.27	3.15e−03
	615000	17.2	16.9	1.07e−03	2.28	2.37	6.44e−04
	1000000	18.1	17.8	1.55e−05	2.58	2.66	1.17e−05

		BHK vault			**Waste compartment**		
	Time, years	**$Q_{l,in}$**	**$Q_{l,out}$**	**$Q_{g,out}$**	**$Q_{l,in}$**	**$Q_{l,out}$**	**$Q_{g,out}$**
Case 9	0	8.62e−02	8.62e−02	0	1.16e−02	1.16e−02	0
	1 000	8.19e−02	8.28e−02	3.90e−03	7.71e−03	7.93e−03	3.51e−03
	74 900	8.20e−02	8.30e−02	3.20e−03	7.78e−03	8.03e−03	2.89e−03
	615 000	8.25e−02	8.35e−02	1.43e−03	8.13e−03	8.36e−03	1.18e−03
	1 000 000	8.53e−02	8.64e−02	1.39e−08	1.07e−02	1.12e−02	4.64e−09
Case 10	0	6.99	6.99	0	9.27e−01	9.27e−01	0
	1 000	6.67	6.71	2.96e−03	6.18e−01	6.53e−01	3.24e−03
	74 900	6.68	6.72	2.39e−03	6.24e−01	6.59e−01	2.65e−03
	615 000	6.70	6.75	1.57e−03	6.36e−01	6.71e−01	1.73e−03
	1 000 000	6.88	6.96	4.82e−08	8.10e−01	8.62e−01	6.94e−09
Case 11	0	18.2	18.2	0	2.48	2.48	0
	1 000	16.2	16.1	2.95e−03	1.58	1.64	2.92e−03
	74 900	16.2	16.0	2.42e−03	1.58	1.64	2.47e−03
	615 000	16.7	16.6	2.62e−04	1.75	1.80	3.79e−04
	1 000 000	17.9	17.9	2.35e−08	2.22	2.30	1.60e−08
Case 12	0	8.29e−02	8.29e−02	0	1.19e−02	1.19e−02	0
	1 000	8.24e−02	8.21e−02	3.86e−03	9.20e−03	9.28e−03	3.60e−03
	74 900	8.17e−02	8.12e−02	3.54e−03	8.95e−03	9.08e−03	3.30e−03
	615 000	8.23e−02	8.17e−02	6.51e−05	9.98e−03	1.04e−02	2.75e−05
	1 000 000	8.30e−02	8.23e−02	2.37e−06	1.07e−02	1.11e−02	2.26e−06
Case 13	0	6.73	6.73	0	9.52e−01	9.52e−01	0
	1 000	6.56	6.48	3.61e−03	6.85e−01	7.36e−01	4.13e−03
	74 900	6.57	6.49	2.72e−03	6.94e−01	7.43e−01	3.12e−03
	615 000	6.60	6.53	5.89e−04	7.27e−01	7.77e−01	5.04e−04
	1 000 000	6.69	6.62	4.87e−06	8.14e−01	8.52e−01	7.04e−06
Case 14	0	18.2	18.2	0	2.48	2.48	0
	1 000	15.6	15.4	3.89e−03	1.49	1.62	5.01e−03
	74 900	15.6	15.5	3.22e−03	1.51	1.64	4.14e−03
	615 000	15.8	15.7	2.11e−03	1.55	1.68	2.78e−03
	1 000 000	17.4	17.3	8.71e−06	1.98	2.03	5.58e−06

Overall, the variations in the BHK vault hydraulics are small. In general, the water inflow and outflow rates to/from the vault and the waste decreases during the stainless-steel corrosion period. Gas outflow from the vault increases in this period. Moreover, the relative difference between the in and out water flowrates in the vault is less than 2 %. In contrast, the effect of gas generation on the waste hydraulics increases as the groundwater flux increases. For high horizontal water flow (Cases 5 and 8), the maximum difference between the in and out water flowrates in the waste is about 4 %. For vertical downwards water flow, the maximum difference is less than 5 %, 7 % and 9 % for low (Cases 9 and 12), medium (Cases 10 and 13) and high (Case 14) groundwater flow, respectively. In all the cases, the initial state of the system is almost completely recovered in the very long term (compare the initial flowrates with the flowrates at $t = 1\,000\,000$ years).

4.2 Host rock including a fracture zone

In the following set of simulation cases a 1 m thick fracture zone of relatively high permeability has been added to the rock domain. The fracture zone intersects the BHK vault as shown in Figure 2-7. Like the rock, the fracture zone is modelled as an ECPM. The same governing equations for immiscible two-phase flow apply to the fracture zone, the rock and the vault. The model geometry is shown in Figure 2-7, showing the fracture zone intersecting obliquely with the vault at the top of the backfill.

The results obtained from different simulations performed to study the effect of this single fracture zone on gas release, are presented in this section.

4.2.1 Results

Given the statistics presented in Sub-Section 2.3.2, seven values of fracture zone permeability were used for individual simulation cases, as listed in Table 4-4.

In all these simulations cases, a contrast of water retention properties between the waste and the backfill is considered, with the values specified in Table 2-2. Moreover, the distance Δy_{ext} used to calculate the Cauchy coefficients (Equation 2-17b) is 10.77 m at the top boundary and 0.24 m at the left boundary.

The results of the simulations are presented here as a sensitivity analysis, considering the permeability of the fracture zone. They are compared with the Base Case scenario where the rock is considered as a homogeneous medium (Case 2).

Table 4-4. Cases to study hydrogen generation and migration around BHK with a rock including a fracture zone.

Case #	Fracture zone transmissivity[a] (m^2/s)	Fracture zone permeability[b] (m^2)	Description[c]
15	3.93×10^{-8}	8.00×10^{-15}	close to rock
16	2.46×10^{-7}	5.00×10^{-14}	< 40 %
17	4.92×10^{-7}	1.00×10^{-13}	intermediate value
18	4.46×10^{-6}	9.08×10^{-13}	average
19	1.51×10^{-5}	3.07×10^{-12}	< 75 %
20	3.04×10^{-5}	6.18×10^{-12}	< 95 %
21	1.23×10^{-4}	2.5×10^{-11}	maximum

[a] Rhén et al. (2008).

[b] Calculated using the transmissivity data, the values water density and viscosity shown in Table 2-3, and assuming a fracture zone thickness of 1.0 m.

[c] Statistics presented in Sub-Section 2.3.2.

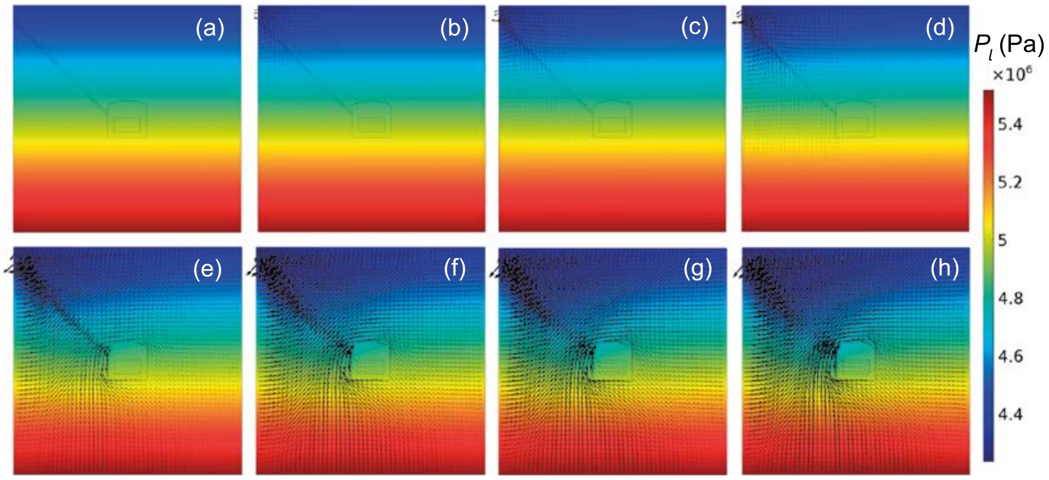

***Figure 4-31.** Water pressure distribution and groundwater Darcy flux vector obtained at 1 000 years for different permeabilities of the fracture zone: (a) Case 2 (homogeneous rock), (b) Case 15, (c) Case 16, (d) Case 17, (e) Case 18, (f) Case 19, (g) Case 20, (h) Case 21.*

The distribution of liquid pressure and the Darcy's fluxes of the liquid phase obtained after 1 000 years are shown in Figure 4-31. Results show that as the permeability of the facture zone increases, the system around the fracture close to the vault is depressurized. Note that as the permeability of the fracture zone is reduced, the liquid pressure distribution approaches the distribution obtained in the homogeneous rock case (compare Figure 4-31b and Figure 4-31a). Also, for fracture zone permeabilities lower than the average value (Case 18), the water that is just above the fracture zone flows upward and parallel to the fracture (Figure 4-31b, c and d; Figure 4-32a). As the permeability increases, the direction of the water flux changes to be perpendicular to the fracture (Figure 4-31f, g and h; Figure 4-32b). Moreover, the flow within the vault, which for low permeabilities is directed upwards in the backfill, increases and changes to follow a more horizontal orientation (compare Figure 4-31b and Figure 4-31h). This suggests that as the permeability of the fracture zone increases, more gas and water should be extracted from the vault. However, the gas saturation within the fracture zone also should decrease to some extent, in response to the water contribution coming from the rock. This can be seen by inspecting Figure 4-33 to Figure 4-36, which show the evolution of the gas saturation distribution. During the first 90 years, gas flows in the direction of the fracture zone (Figure 4-33). The water flow into the fracture zone and its effect on gas release is apparent for fracture zone permeabilities higher than 3.07×10^{-12} m^2 (Cases 19, 20 and 21). In these cases, the gas reaches the left lateral boundary after 90 years, lowering the gas saturation above the fracture zone as the permeability increases (compare Figure 4-33f with Figure 4-33h).

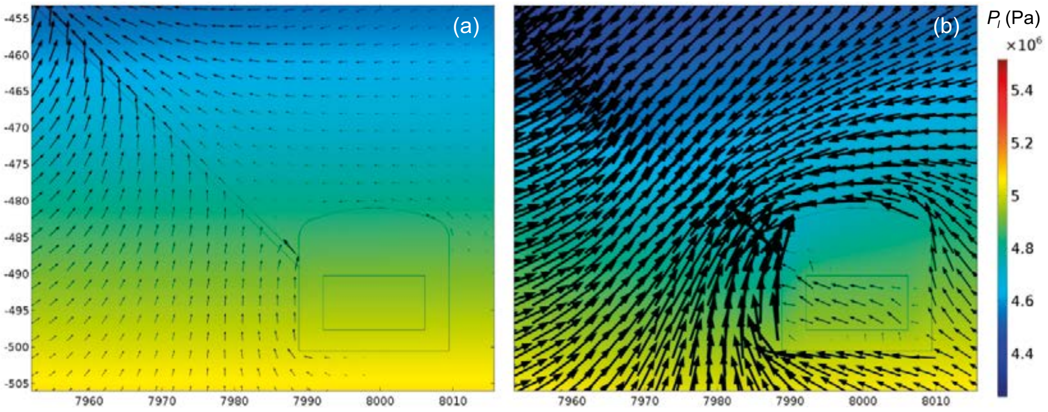

Figure 4-32. *Water pressure distribution and groundwater Darcy flux vector around the BHK vault obtained at 1 000 years for (a) Case 17 and (b) Case 20.*

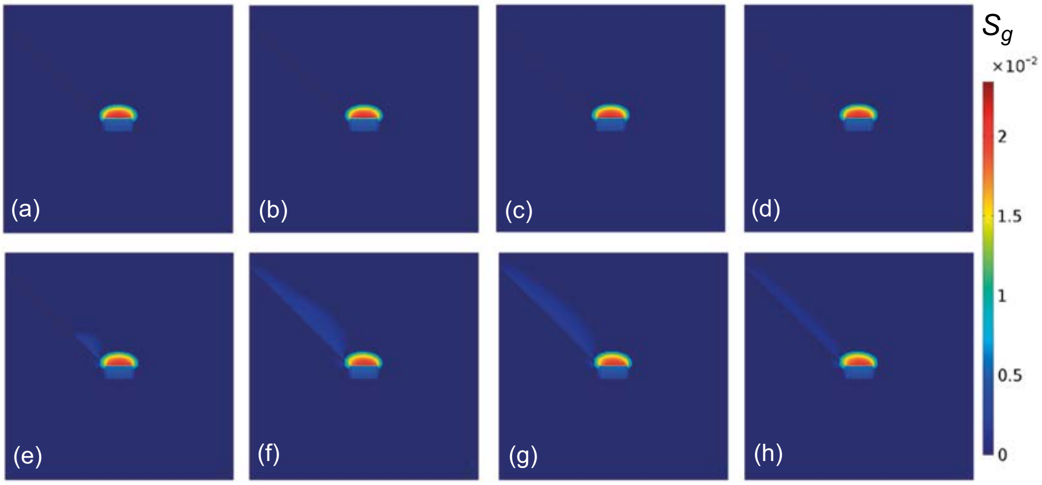

Figure 4-33. *Gas saturation obtained at 90 years for different permeabilities of the fracture zone: (a) Case 2 (homogeneous rock), (b) Case 15, (c) Case 16, (d) Case 17, (e) Case 18, (f) Case 19, (g) Case 20, (h) Case 21.*

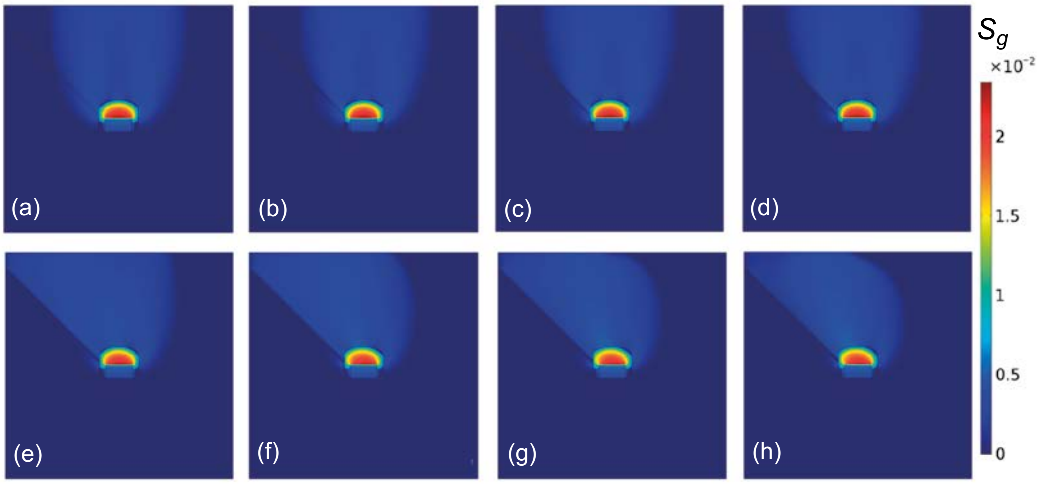

***Figure 4-34.** Gas saturation obtained at 115 years for different permeabilities of the fracture zone: (a) Case 2 (homogeneous rock), (b) Case 15, (c) Case 16, (d) Case 17, (e) Case 18, (f) Case 19, (g) Case 20, (h) Case 21.*

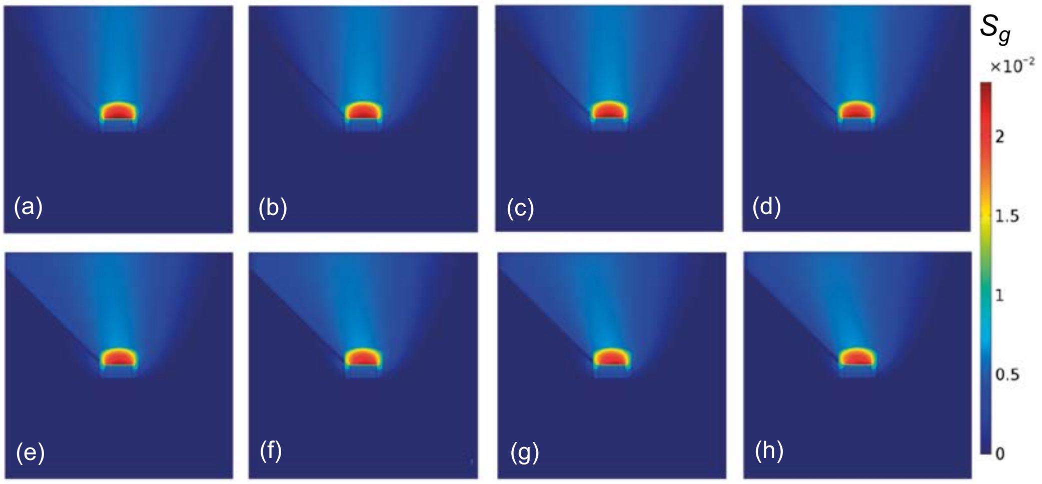

***Figure 4-35.** Gas saturation obtained at 1 000 years for different permeabilities of the fracture zone: (a) Case 2 (homogeneous rock), (b) Case 15, (c) Case 16, (d) Case 17, (e) Case 18, (f) Case 19, (g) Case 20, (h) Case 21.*

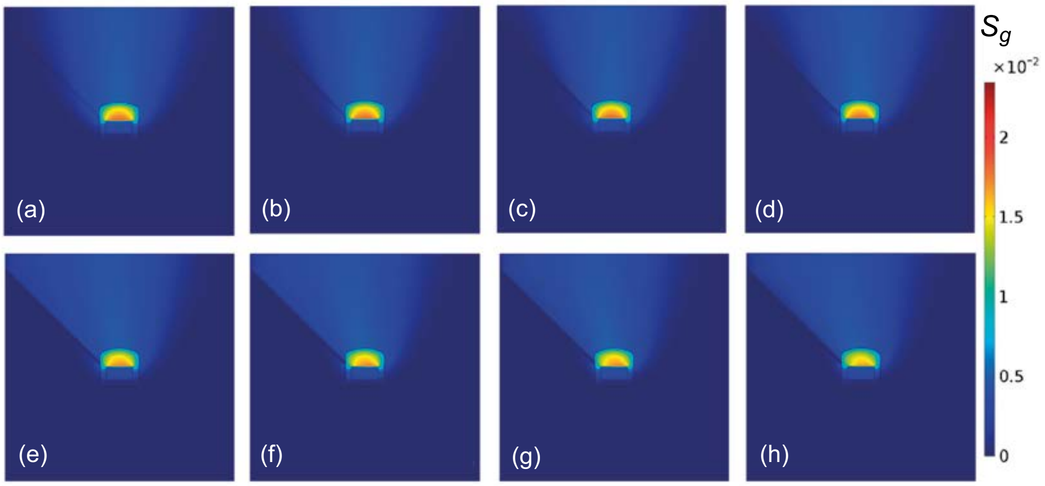

***Figure 4-36.** Gas saturation obtained at 616 000 years for different permeabilities of the fracture zone: (a) Case 2 (homogeneous rock), (b) Case 15, (c) Case 16, (d) Case 17, (e) Case 18, (f) Case 19, (g) Case 20, (h) Case 21.*

Figure 4-37 and Figure 4-38 show the effect of fracture zone permeability on the gas saturation and Darcy flux vector obtained at 90 and 1 000 years, respectively. In the short term, for permeabilities higher than 3.07×10^{-12} m^2, gas flows following the direction of the fracture zone (Figure 4-37f, g and h). In the mid-term (100 to 1 000 years), and for permeabilities lower than 10^{-13} m^2 (Cases 15, 16 and 17), the buoyancy forces are dominant. Gas tends to float above the vault and the gas flow through the fracture is minor (see Figure 4-34 and Figure 4-35). After 1 000 years, for permeabilities higher than 3.07×10^{-12} m^2, the gas that is just above the fracture zone flows parallel to the fracture zone (see Figure 4-38f, g and h).

In Case 2 (homogeneous host rock), gas accumulates in the top of the backfill. This causes a local increase in pressure, leading to a long-term retention of gas in this part of the vault. When a fracture zone intercepts the vault less gas accumulates in the backfill above the waste (e.g., compare Figure 4-35c and Figure 4-35h). Figure 4-39 shows the gas saturation and the Darcy flux vector of gas within the vault obtained at 1 000 years in Case 16 and Case 21. This figure shows that when the fracture permeability is higher than the average value, high gas fluxes follow the orientation of the fracture (Figure 4-39 bottom right). The enhanced gas release from the vault reduces the gas saturation above the waste compartment (Figure 4-39 top right).

Because of the increased release of gas and water, the presence of the fracture zone helps to decrease the pressure within and around the BHK vault. The initial pressure distribution is affected by the fracture zone, compared to the hydrostatic conditions set in the homogeneous rock scenario (compare, for instance, the pressure distributions at 1 000 years shown in Figure 4-31). This perturbation in the initial pressure field is more important as the permeability of the fracture zone becomes higher. The overpressure due to gas production within the vault is reduced as the permeability of the fracture zone increases. Also, because the relatively low gas generation rates, the pressure increase within the BHK vault is not very high. The effect of the fracture zone permeability on the average gas pressure within the BHK vault is shown in Figure 4-40. The results show that the pressure in the vault is reduced as the permeability of the fracture zone is increased.

The average gas pressure curves display different rates of reduction after the consumption of each steel type. This is because the gas generation is driven by different steel corrosion regimes. Initially, both stainless and carbon steel corrode and produce hydrogen gas. The gas leaving the vault is immediately replaced by gas generated by steel corrosion. When the stainless steel is consumed, gas keeps being generated from carbon steel corrosion. After the carbon steel is consumed the gas generation stops. The gas pressures within the vault start to decrease progressively as the gas leaves the vault, approaching the initial pressures in the long-term. The rate of this decrease depends on the hydraulic contrast between the rock, fracture and vault materials. It is worth noting that hydrogen dissolution in the groundwater would reduce gas pressures faster than shown in Figure 4-40.

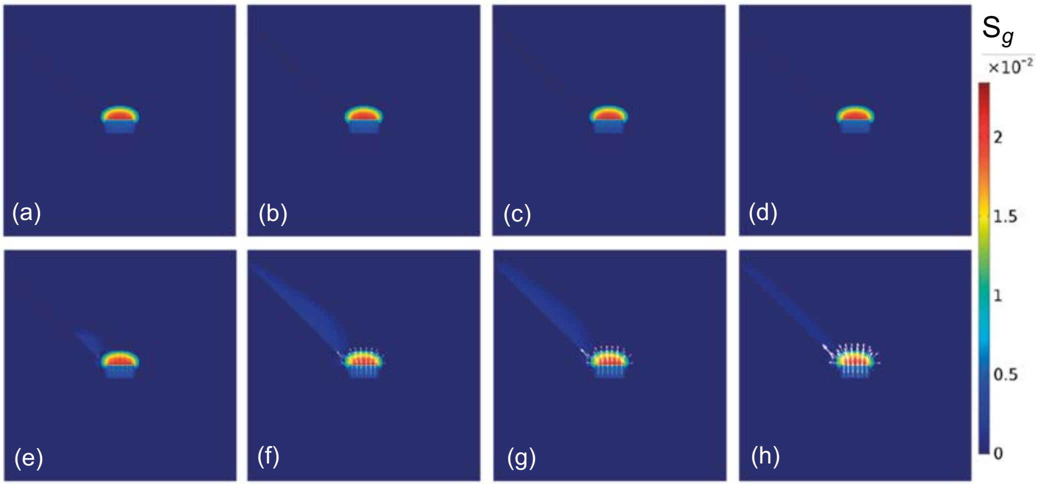

Figure 4-37. *Gas saturation and Darcy flux vector of the gas phase (white arrows) around the BHK vault at 90 years for different permeabilities of the fracture zone: (a) Case 2 (homogeneous rock), (b) Case 15, (c) Case 16, (d) Case 17, (e) Case 18, (f) Case 19, (g) Case 20, (h) Case 21.*

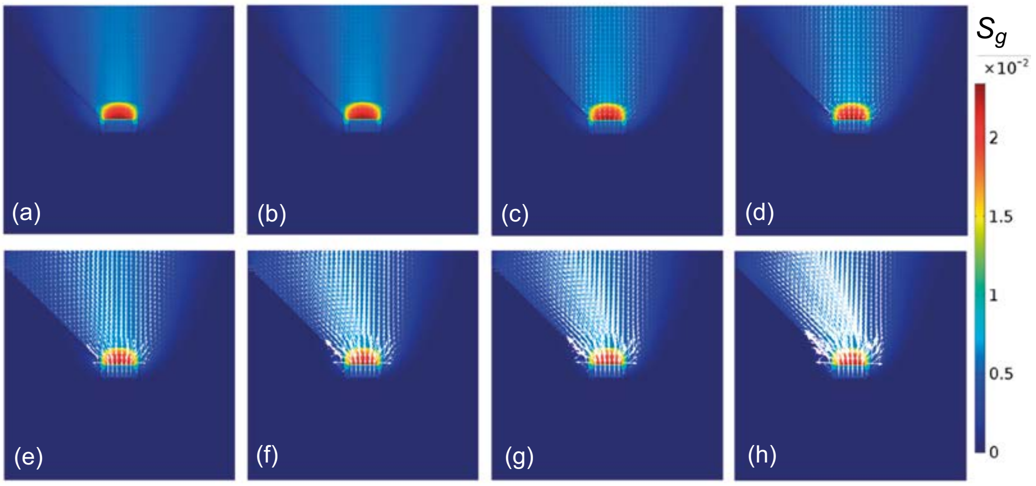

Figure 4-38. *Gas saturation and Darcy flux vector of the gas phase (white arrows) around the BHK vault at 1 000 years for different permeabilities of the fracture zone: (a) Case 2 (homogeneous rock), (b) Case 15, (c) Case 16, (d) Case 17, (e) Case 18, (f) Case 19, (g) Case 20, (h) Case 21.*

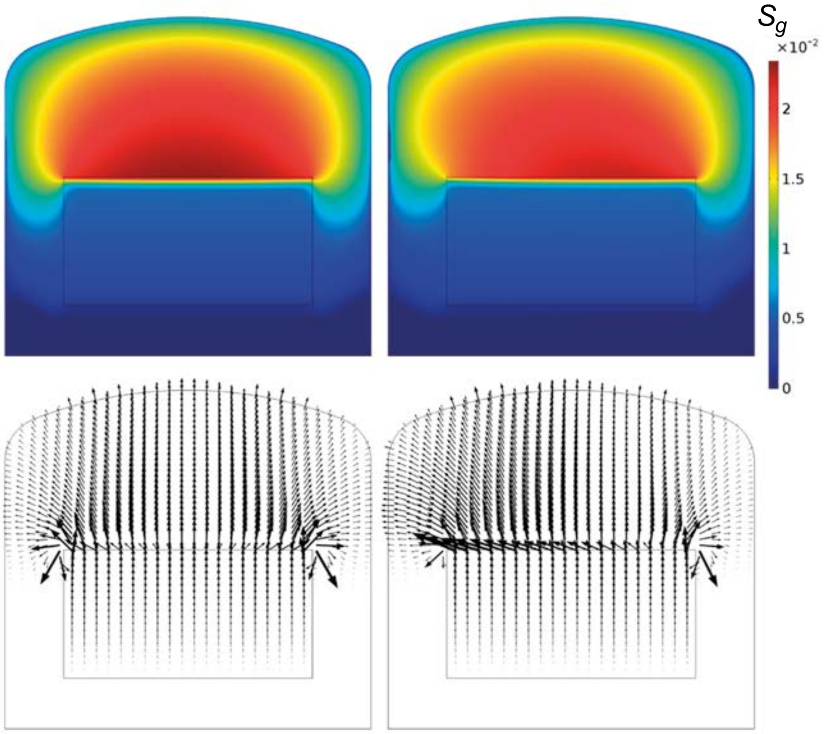

Figure 4-39. *Gas saturation (top) and Darcy flux vector of gas phase (bottom) within the BHK vault obtained at 1 000 years in: (left) Case 16, (right) Case 21.*

Another interesting indicator is the difference between the average pressure in the vault obtained in Cases 15 to 21 and the average pressure obtained in Case 2 (homogeneous rock). This pressure reduction is depicted in Figure 4-41 for 3 different times. The curves in Figure 4-40 are nearly parallel, meaning that the pressure reduction is kept constant during the whole simulation time. However, as the permeability of the fracture zone increases, the pressure reduction decreases (increases in magnitude). Note that the gas pressure in the vault is reduced by about 0.3 bar compared to Base Case 2, for an average permeability of the fracture zone (Case 18). The maximum pressure reduction is about 0.8 bar obtained when the fracture zone permeability is 2.50×10^{-11} m^2 (Case 21).

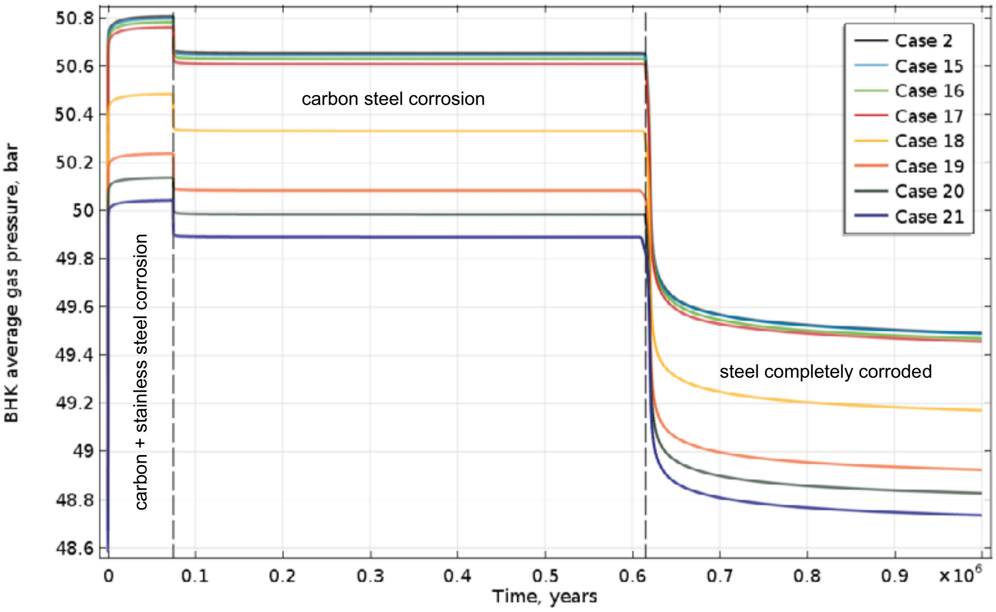

Figure 4-40. Effect of the fracture zone permeability on the evolution of the average gas pressure in the BHK vault.

It is worth noting that Figure 4-41 shows a clear permeability threshold of 10^{-13} m^2. Below this value (Cases 15, 16 and 17) the gas buoyancy above the vault dominates over the gas flow through the fracture (see Figure 4-34 and Figure 4-35). Thus, the pressure reduction due to the influence of the fracture zone is minor. On the other hand, for Cases 18, 19, 20 and 21, as the fracture zone permeability increases, the flow of water and gas through the fracture increases as well (see Figure 4-31, Figure 4-37 and Figure 4-38). The pressure reduction increases accordingly. Moreover, Figure 4-41 suggests that there is a limit of about 1.0 bar or less in the pressure reduction caused by highly conductive fracture zones.

4.2.2 Inflow and outflow rates

Table 4-5 summarizes the volumetric inflow and outflow rates to/from the BHK vault and the waste compartment obtained at four different times for Cases 15 to 21. The homogeneous rock case was also added as reference (Base Case 2). As was the case for values in Table 4-3, these flowrates were calculated assuming a vault thickness of 1.0 m, and they are used here only for comparison purposes.

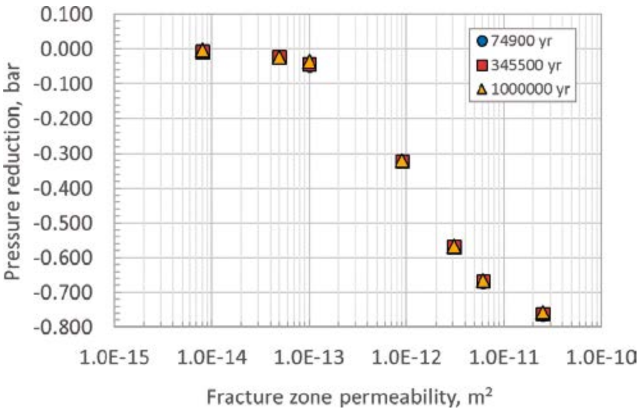

Figure 4-41. Impact of fracture zone permeability on the pressure reduction respect to the homogeneous rock case (Case 2).

It can be observed that all the inflow and outflow rates are directly proportional to the permeability of the fracture zone. This is a preferential pathway for fluid flow. Accordingly, during the gas generation period gas outflow rates are higher than the corresponding gas outflow rates obtained in a host-rock without a fracture (Case 2). This leads to lower amounts of gas within the vault after the steel corrosion has finished. Consequently, after 615 000 years, the gas outflow rates obtained in a system including a fracture zone are lower than the gas outflow rates in a host-rock without a fracture. Also, the fracture causes that water outflow rates from the vault are higher than water inflow rates from the vault. The maximum relative difference is about 5.1 % (Case 21). The corresponding maximum difference between the in and out water flowrates in the waste is about 1.5 %.

Table 4-5. Inflow and outflow rates (m^3/year) of water (Q_l) and gas (Q_g) to/from the BHK vault and the waste compartment, simulated including a fracture zone that intersects the BHK vault.

		BHK vault			Waste compartment		
	Time, years	$Q_{l,in}$	$Q_{l,out}$	$Q_{g,out}$	$Q_{l,in}$	$Q_{l,out}$	$Q_{g,out}$
Case 2	0	0	0	0	0	0	0
	1 000	0	0	3.87e−03	0	0	3.60e−03
	74 900	0	0	3.21e−03	0	0	2.98e−03
	615 000	0	0	8.86e−04	0	0	6.23e−04
	1 000 000	0	0	1.25e−05	0	0	1.20e−05
Case 15	0	3.03e−02	3.03e−02	0	4.72e−03	4.72e−03	0
	1 000	2.80e−02	2.78e−02	3.92e−03	3.73e−03	3.72e−03	3.99e−03
	74 900	2.77e−02	2.76e−02	3.93e−03	3.65e−03	3.63e−03	3.99e−03
	615 000	2.83e−02	2.81e−02	2.05e−03	3.80e−03	3.78e−03	2.08e−03
	1 000 000	3.06e−02	3.05e−02	1.04e−08	4.81e−03	4.75e−03	3.76e−09
Case 16	0	7.81e−02	7.81e−02	0	1.32e−02	1.32e−02	0
	1 000	7.00e−02	7.08e−02	3.89e−03	1.01e−02	1.01e−02	3.98e−03
	74 900	6.96e−02	7.04e−02	3.89e−03	9.93e−03	9.88e−03	3.98e−03
	615 000	7.08e−02	7.16e−02	2.01e−03	1.03e−02	1.02e−02	2.06e−03
	1 000 000	7.70e−02	7.80e−02	8.58e−09	1.30e−02	1.28e−02	2.61e−09
Case 17	0	1.62e−01	1.62e−01	0	2.63e−02	2.63e−02	0
	1 000	1.41e−01	1.45e−01	3.88e−03	1.99e−02	1.98e−02	3.98e−03
	74 900	1.40e−01	1.44e−01	3.88e−03	1.95e−02	1.94e−02	3.98e−03
	615 000	1.44e−01	1.47e−01	2.03e−03	2.03e−02	2.02e−02	2.08e−03
	1 000 000	1.58e−01	1.62e−01	1.08e−08	2.55e−02	2.52e−02	3.45e−09
Case 18	0	1.76	1.76	0	2.32e−01	2.32e−01	0
	1 000	1.46	1.53	3.95e−03	1.67e−01	1.66e−01	3.94e−03
	74 900	1.48	1.55	2.76e−03	1.69e−01	1.68e−01	2.66e−03
	615 000	1.50	1.57	1.83e−03	1.73e−01	1.72e−01	1.82e−03
	1 000 000	1.69	1.77	1.03e−08	2.23e−01	2.20e−01	2.96e−09
Case 19	0	3.28	3.28	0	4.18e−01	4.18e−01	0
	1 000	2.76	2.90	4.03e−03	3.06e−01	3.04e−01	3.91e−03
	74 900	2.75	2.89	4.03e−03	3.02e−01	3.00e−01	3.91e−03
	615 000	2.81	2.95	1.93e−03	3.14e−01	3.12e−01	1.88e−03
	1 000 000	3.15	3.31	1.00e−08	4.03e−01	3.96e−01	2.62e−09
Case 20	0	3.89	3.89	0	4.92e−01	4.92e−01	0
	1 000	3.30	3.46	4.06e−03	3.62e−01	3.60e−01	3.90e−03
	74 900	3.28	3.45	4.06e−03	3.58e−01	3.56e−01	3.91e−03
	615 000	3.34	3.51	2.09e−03	3.71e−01	3.68e−01	2.01e−03
	1 000 000	3.74	3.93	1.00e−08	4.74e−01	4.67e−01	2.56e−09
Case 21	0	4.48	4.48	0	5.63e−01	5.63e−01	0
	1 000	3.81	4.00	4.09e−03	4.16e−01	4.14e−01	3.90e−03
	74 900	3.84	4.03	2.53e−03	4.22e−01	4.19e−01	2.31e−03
	615 000	3.88	4.07	1.66e−03	4.30e−01	4.28e−01	1.59e−03
	1 000 000	4.30	4.52	1.04e−08	5.43e−01	5.34e−01	2.62e−09

5 Conclusions

A conceptual and numerical model has been developed for simulating hydrogen production and release from the BHK waste and multiphase flow through the near-field. The model has been implemented in COMSOL Multiphysics 5.2a and accounts for immiscible two-phase flow through porous media, considering hydrogen generation due to steel corrosion.

A total of 21 simulation cases were run encompassing several combinations of groundwater flow conditions, water retention curves, and permeability of a fracture zone intersecting the BHK vault. The simulation time was 1 000 000 years in all cases. This simulation time accounts for different gas generation regimes depending on the corrosion times of stainless and carbon steel. The dissipation of gas pressures and the subsequent buoyancy of the gas phase expected to occur after the complete corrosion of steel has also been simulated.

It was found that gas migration depends on groundwater flow conditions and the presence of fracture zones intersecting the BHK vault.

Under hydrostatic conditions, the gas overpressure is in the order of 1.5 to 2.4 bar, which is reached during the corrosion of both stainless and carbon steel. After the complete corrosion of stainless-steel, the overpressure decreases about 0.2 bar. After complete corrosion, the overpressure decreases significantly, until the initial conditions are almost recovered completely.

The results also reveal that the interaction between capillary and buoyancy forces depends on the groundwater flow conditions and the water retention properties of the vault materials. The simulated water fluxes were in the range of measurements. Also, a larger water flux of 5.00×10^{-8} m^3/m^2 s was considered to evaluate hypothetical cases where high pressures are developed due to downward vertical water flow. For groundwater flows below 10^{-8} m^3/m^2 s, gas buoyancy is the main driving force of gas flow. For flows in the order of 10^{-8} m^3/m^2 s or higher, however, the gas flow is also affected by groundwater flow direction and capillary forces. When different water retention curves are applied to the waste and backfill materials, gas tends to accumulate in the top backfill and is released faster. This is because the waste has a higher entry pressure. Using uniform water retention properties in the vault results in higher average gas pressures than when the water retention properties are different. However, a contrast of water retention properties can lead to higher local pressures, especially in the top backfill.

The horizontal groundwater flow decreases the average gas pressure in the vault. A maximum pressure decrease of about 2 bar with respect the hydrostatic situation has been calculated. This pressure decrease corresponds to the maximum measured groundwater flux (1.89×10^{-8} m^3/m^2 s). Consequently, the overpressure decreases as the groundwater flow increases. The vertical downwards groundwater flow increases the pressure in the vault. Under these conditions, the buoyancy and capillary forces act in opposite direction. The overpressures are lower when the water retention curves of the backfill and waste are the same, and higher when they are different. Note that groundwater flow affects the gas pressure in the vault, but the overpressure is similar for all the groundwater flow cases, ranging from 1.5 to 2.5 bar.

Some key questions are answered below:

a) What are the pressures affecting BHK vault materials?

Overall, the simulated internal gas pressures are below 61 bars during the whole simulation time. Note that this pressure is obtained under high vertical downwards groundwater flow conditions ($q = 5.0 \times 10^{-8}$ m^3/m^2 s), which is the worst case considered in the present study. In practice, the maximum measured groundwater flux is about 1.89×10^{-8} m^3/m^2 s, for which the maximum pressure in the BHK vault is in the order of 55 bar. The corresponding gas overpressures with respect to the initial hydrostatic conditions are about 10 and 5 bars, respectively. Moreover, these overpressures could be lower as gas miscibility was not considered in the present study. A model considering poroelasticity and one-way coupling between multiphase flow and mechanics is presented in Appendix B. Preliminary simulations show that the effect of gas generation on the mechanical behaviour of the BHK vault is negligible. The displacements caused by gas generation are in the order of a few microns. This is because of the low level of gas saturation, which leads to an equivalent pore pressure that is very similar to the initial liquid pressure. This suggests that the BHK vault can withstand internal gas pressures below 61 bars. Of course, this situation could be completely different if the actual steel corrosion rates were higher (see answer to question d).

b) What is the effect of gas production and migration on the water saturation conditions of the near field?

   The simulations described in Section 4.1 indicate that, due to the low hydrogen generation rates, under hydrostatic conditions gas production does not affect the water pressure field, and water flow is quasi-stationary through the entire simulation time. Also, under low horizontal and vertical downwards groundwater flow conditions, the system evolves similarly to the behavior found for hydrostatic conditions. Interestingly, the water inflow rates to the BHK vault presented in Table 4-3 suggest that there is a maximum difference of about 14 % with respect to the initial conditions obtained at the end of the stainless-steel corrosion period (74 900 years). This is found for high vertical downwards water flow ($q = 5.0 \times 10^{-8}$ m^3/m^2 s). In practice, water fluxes lower than 1.89×10^{-8} m^3/m^2 s can be expected, for which the effect of gas production and migration on the water entering the vault is reduced to about 10 %. In addition, the maximum gas saturations are developed within the vault and they are lower than 3.5 % (see answer to question d).

c) How will gas production and migration affect the hydraulic behavior of the concrete barriers?

   This depends strongly on the groundwater flow conditions, especially on the magnitude of the groundwater flux. It can be concluded that gas generation in the vault has a small impact on the hydraulic behavior of the concrete barriers. The hydraulics of the vault changes only for high water flow conditions during the first 1 000 years. This is the transient period during which the gas pressure increases until reaching its maximum (quasi-steady state). In contrast, gas generation impacts the hydraulics of the waste, which also depends on the groundwater flux. Especially for vertical downwards water flow, as the groundwater flux increases the difference between the inflow and outflow water rates in the waste increases. Nevertheless, in the long term the initial state of the vault is almost recovered.

d) Could the evolution of a gas phase affect the assumption of fully saturated conditions for radionuclide transport analysis?

   The simulations show that the maximum gas saturations that could be expected are about 3.5 %. This suggests that the conditions of the repository are close to full saturation all the time. Of course, this conclusion is strongly linked to the selected corrosion rates, which have been kept constant in all the simulations performed in this study.

e) What is the effect of fracture zones on the gas release and the overpressures developed in the BHK vault?

   A fracture zone intersecting the BHK vault is a preferential pathway for gas release, causing a reduction of the gas pressures within the vault. As expected, the inflow and outflow rates to/from the vault and the waste compartment are proportional to the fracture zone permeability (Table 4-5). The pressure reduction curve displays a transition between two distinct regimes. For fracture zone permeabilities equal or lower than 10^{-13} m^2, the buoyancy forces are dominant. Consequently, gas flows mainly upwards above the vault and the fracture. Accordingly, the impact of the fracture zone on the pressure reduction is minor. The pressure reduction starts to be noticeable for fracture zone permeabilities higher than 10^{-13} m^2. As expected, the higher the permeability, the higher the flow of water and gas through the fracture zone, and the higher the pressure reduction. A maximum pressure reduction of about 1.0 bar with respect to the case of homogeneous rock can be expected, if a fracture zone with a permeability above 2.50×10^{-11} m^2 intersects the vault.

References

SKB's (Svensk Kärnbränslehantering AB) publications can be found at www.skb.com/publications. SKBdoc documents will be submitted upon request to document@skb.se.

Abarca E, Sampietro D, Molinero J, von Schenck H, 2019. Modelling of the near-field hydrogeology – temperate climate conditions. Report for the safety evaluation SE-SFL. SKB R-19-03, Svensk Kärnbränslehantering AB.

Amec Foster Wheeler, 2015. ConnectFlow version 11.2. Harwell, UK: Amec Foster Wheeler Nuclear UK Limited**.**

Baroghel-Bouny V, Mainguy M, Lassabatere T, Coussy O, 1999. Characterization and identification of equilibrium and transfer moisture properties for ordinary and high-performance cementitious materials. Cement and Concrete Research 29, 1225–1238.

Bary B, Bournazel J-P, Bourdarot E, 2000. Poro-damage approach applied to hydro-fracture analysis of concrete. Journal of Engineering Mechanics 126, 937–943.

Bear J, Bachmat Y, 1990. Introduction to modeling of transport phenomena in porous media. Dordrecht: Kluwer.

Brooks R H, Corey A T C, 1964. Hydraulic properties of porous media. Hydrology Papers 3. Fort Collins: Colorado State University.

Chung T H, Ajlan M, Lee L L, Starling K S, 1988. Generalized multiparameter correlation for nonpolar and polar fluid transport properties. Industrial & Engineering Chemistry Research 27, 671–679.

COMSOL, 2015. Comsol Multiphysics v 5.2a. Stockholm: COMSOL AB.

Coussy O, Dangla P, Lassabatère T, Baroghel-Bouny V, 2004. The equivalent pore pressure and the swelling and shrinkage of cement-based materials. Materials and Structures 37, 15–20.

Cuomo M, Nicolosi A, 2006. A poroplastic model for hygro-chemo-mechanical damage of concrete. EURO-C (Computational modelling of concrete structures Conference), Mayrhofen, Austria, 533–542. Available at: https://hal.archives-ouvertes.fr/file/index/docid/874433/filename/A_poroplastic_model_for_hygro-chemo-mechanical_damage_of_concrete.pdf

Elfwing M, Evins L Z, Gontier M, Grahm P, Mårtensson P, Tunbrant S, 2013. SFL concept study. Main report. SKB TR-13-14, Svensk Kärnbränslehantering AB.

Ernst W G, 1969. Earth materials. Englewood Cliffs, NJ: Prentice-Hall.

Fall M, Nasir O, Nguyen T S, 2014. A coupled hydro-mechanical model for simulation of gas migration in host sedimentary rocks for nuclear waste repositories. Engineering Geology 176, 24–44.

Finsterle S, Pruess K, 1995. Solving the estimation-identification problem in two-phase flow modeling. Water Resources Research 31, 913–924.

Gawin D, Pesavento F, Schrefler B A, 2006. Hygro-thermo-chemo-mechanical modelling of concrete at early ages and beyond. Part II: Shrinkage and creep of concrete. International Journal for Numerical Methods in Engineering 67, 332–363.

Hakami E, Fredriksson A, Lanaro F, Wrafter J, 2008. Rock mechanics Laxemar. Site descriptive modelling, SDM-Site Laxemar. SKB R-08-57, Svensk Kärnbränslehantering AB.

Hjerne C, Nordqvist R, Harrström J, 2010. Compilation and analyses of results from cross-hole tracer tests with conservative tracers. SKB R-09-28, Svensk Kärnbränslehantering AB.

Idiart A, Laviña M, Coene E, 2019. Hydro-chemo-mechanical modelling of concrete degradation issues in SFL. SKB R-19-12, Svensk Kärnbränslehantering AB.

Jarsjö J, Destouni G, Gale J, 2001. Groundwater degassing and two-phase flow in fractured rock: Summary of results and conclusions achieved during the period 1994–2000. SKB TR-01-13, Svensk Kärnbränslehantering AB.

Joyce S, Appleyard P, Hartley L, Tsitsopoulos V, Woollard H, Marsic N, Sidborn M, Crawford J, 2019. Groundwater flow and reactive transport modelling of temperate conditions. Report for the safety evaluation SE-SFL. SKB R-19-02, Svensk Kärnbränslehantering AB.

Lewis R W, Schrefler B A, 1998. The finite element method in the static and dynamic deformation and consolidation of porous media. Chichester: Wiley.

Nickalls R W D, 1993. A new approach to solving the cubic: Cardan's solution revealed. The Mathematical Gazette 77, 354–359.

Nuth M, Laloui L, 2008. Effective stress concept in unsaturated soils: Clarification and validation of a unified framework. International Journal for Numerical and Analytical Methods in Geomechanics 32, 771–801.

NWMO, 2011. Long-term geomechanical stability analysis. NWMO DGR-TR-2011-17, Nuclear Waste Management Organization, Canada.

Pękala M, Olmeda J, Grivè M, Bruno J, 2018. Assessment of Redox State and its impact on the solubility and speciation of selected radionuclides in the SFL repository. SKBdoc 1533627 ver 1.0, Svensk Kärnbränslehantering AB.

Peng D-Y, Robinson D B, 1976. A new two-constant equation of state. Industrial and Engineering Chemistry Fundamentals 15, 59–64.

Reid R C, Prausnitz J M, Sherwood T K, 1977. The properties of gases and liquids. 3rd ed. NewYork: McGraw-Hill.

Rhén I, Forsmark T, Hartley L, Jackson P, Roberts D, Swan D, Gylling B, 2008. Hydrogeological conceptualisation and parameterisation. Site descriptive modelling SDM-Site Laxemar. SKB R-08-78, Svensk Kärnbränslehantering AB.

Román-Ross G, Idiart A, Grandia F, Silva O, Duro L, 2015. Evaluation of a gas experiment – Phase I. ENSI Technical Report, ENSI, Switzerland.

Rossi C, Nimmo J R, 1994. Modeling of soil water retention from saturation to oven dryness. Water Resources Research 30, 701–708.

Rucker D F, Warrick A W, Ferré T P A, 2005. Parameter equivalence for the Gardner and van Genuchten soil hydraulic conductivity functions for steady vertical flow with inclusions. Advances in Water Resources 28, 689–699.

Sander R, 2015. Compilation of Henry's law constants (version 4.0) for water as solvent. Atmospheric Chemistry and Physics 15, 4399–4981.

Schrefler B A, Simoni L, Majorana C E, 1989. A general model for the mechanics of saturated-unsaturated porous materials. Materials and Structures 22, 323–334.

Silva O, Grifoll J, 2007a. Non-passive transport of volatile organic compounds in the unsaturated zone. Advances in Water Resources 30, 794–807.

Silva O, Grifoll J, 2007b. A soil-water retention function that includes the hyper-dry region through the BET adsorption isotherm. Water Resources Research 43. doi:10.1029/2006WR005325

SKB, 2014. Data report for the safety assessment SR-PSU. SKB TR-14-10, Svensk Kärnbränslehantering AB.

Smart N, Hoch A R, 2006. A survey of steel and zircaloy corrosion data for use in the SMOGG gas generation model. Serco report SA/ENV-0841, Serco, UK.

Ulm F-J, Constantinides G, Heukamp F H, 2004. Is concrete a poromechanics material? – A multiscale investigation of poroelastic properties. Materials and Structures 37, 43–58.

van Genuchten M T, 1980. A closed-form equation for predicting the hydraulic conductivity of unsaturated flow. Soil Science Society American Journal 44, 892–898.

Vidstrand P, Rhén I, 2011. On the role of model depth and hydraulic properties for groundwater flow modelling during glacial climate conditions. SKB R-10-74, Svensk Kärnbränslehantering AB.

Vidstrand P, Rhén I, Zugec N, 2010. Groundwater flow modelling of periods with periglacial and glacial climate conditions – Laxemar. SKB R-09-25, Svensk Kärnbränslehantering AB.

Results for low flow conditions

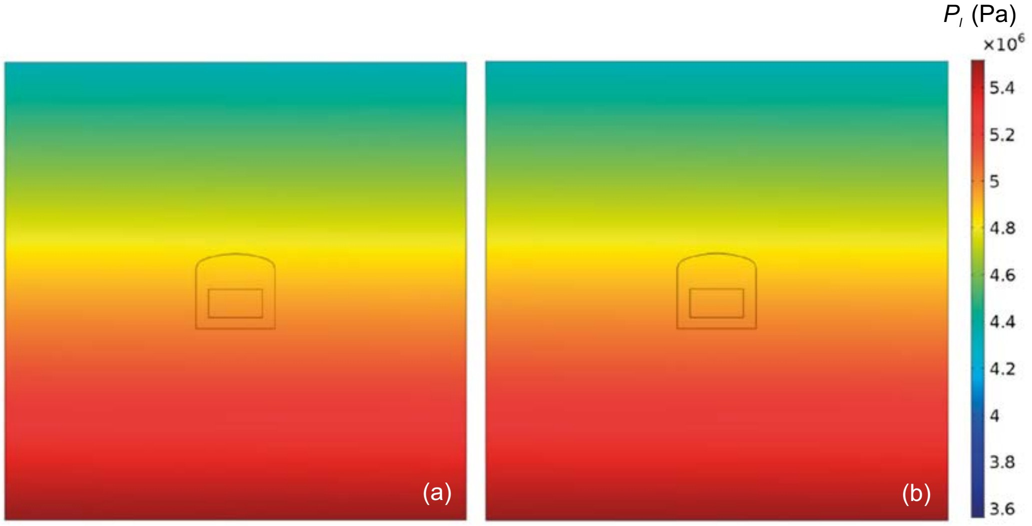

Figure A-1. *Water pressure distribution obtained at 1 000 years for horizontal low flow: (a) Case 3 (b) Case 6.*

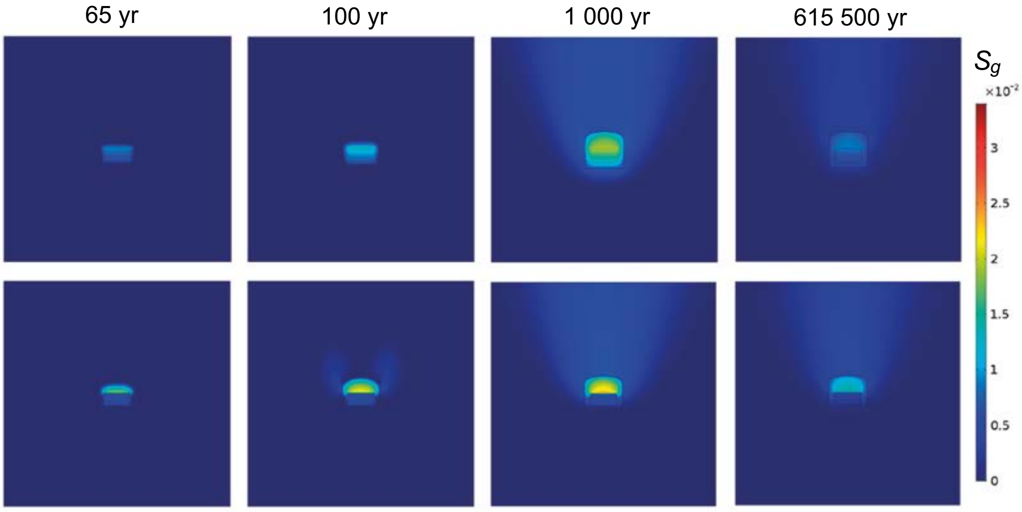

Figure A-2. *Evolution of the gas saturation distribution for horizontal low flow: (top) Case 3, (bottom) Case 6.*

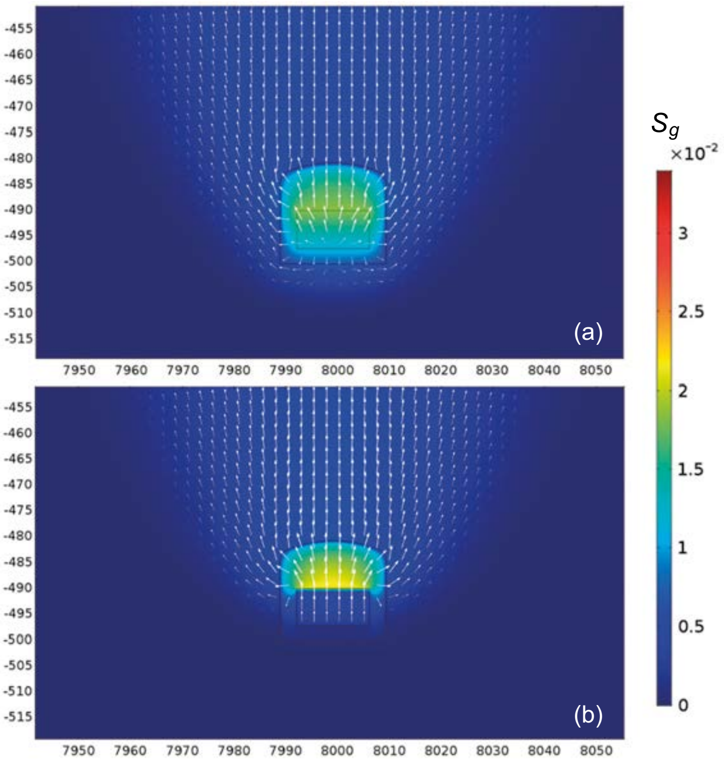

***Figure A-3.** Gas saturation and Darcy flux vector of the gas phase (white arrows) around the BHK vault at 74 900 years for horizontal low flow: (a) Case 3, (b) Case 6.*

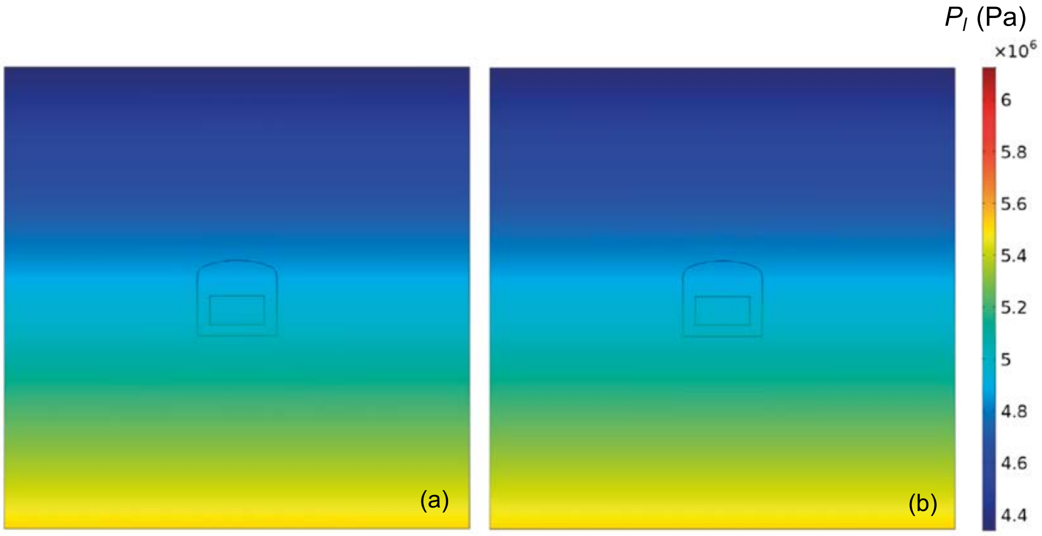

***Figure A-4.** Water pressure distribution obtained at 1 000 years for vertical low flow: (a) Case 9 (b) Case 12.*

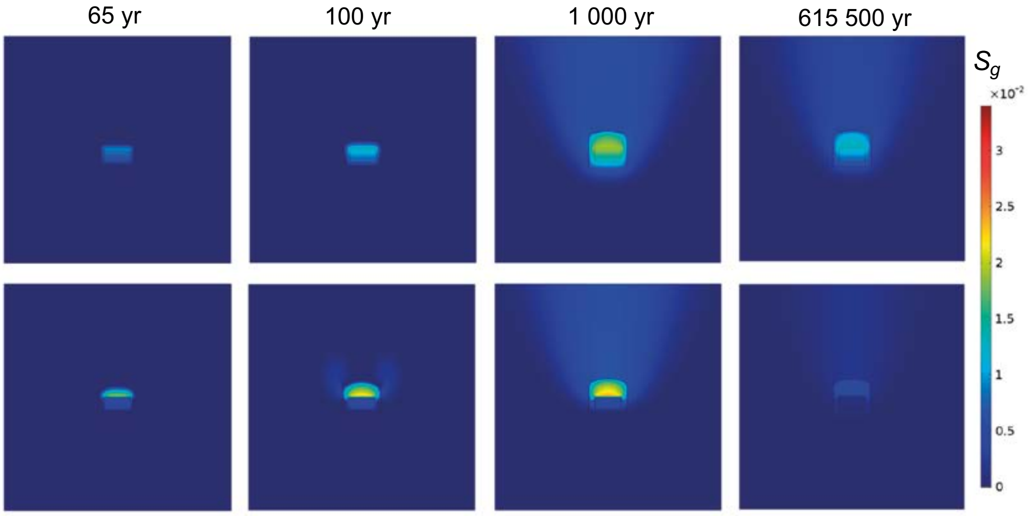

Figure A-5. *Evolution of the gas saturation distribution for vertical low flow: (top) Case 9, (bottom) Case 12.*

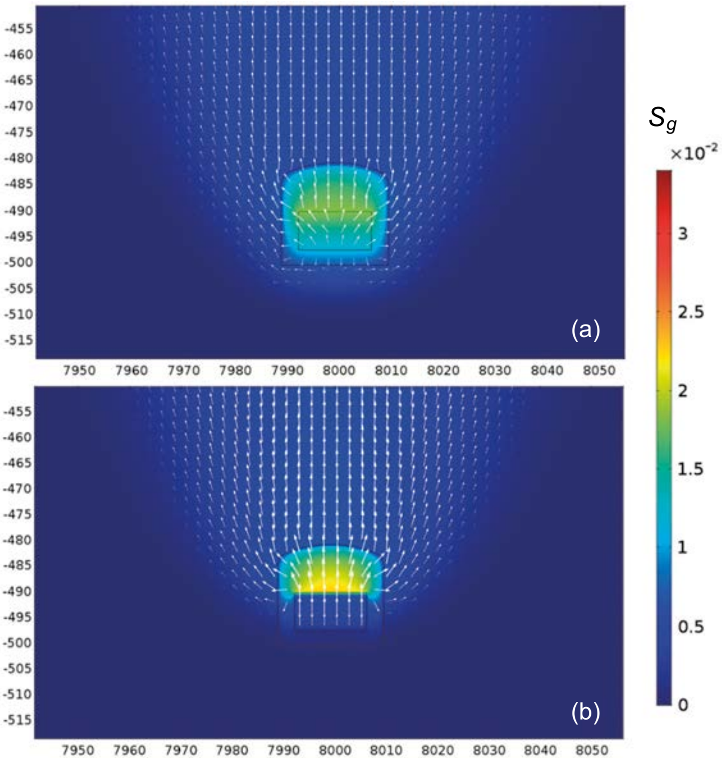

Figure A-6. *Gas saturation and Darcy flux vector of the gas phase (white arrows) around the BHK vault at 74 900 years for vertical low flow: (a) Case 9, (b) Case 12.*

Appendix B

Effect of gas generation on the mechanical stability of the BHK vault

A potentially important aspect of the generation and transport of gas within the BHK vault is the effect of gas overpressures on the mechanical stability of the system. This appendix presents preliminary results of numerical simulations implemented in COMSOL that quantify these effects. A numerical model of the BHK vault based on poroelasticity theory and considering a one-way coupling between multiphase flow and mechanics has been developed. To that end, the liquid and gas pressures and saturations simulated in the multiphase flow problem (Equations 2-7 and 2-8) have been used to calculate an equivalent pore pressure, P_p.

The estimation of an equivalent pore pressure for multiphase systems is non-trivial, especially for cementitious materials (Coussy et al. 2004, Gawin et al. 2006, Nuth and Laloui 2008). However, as a first approximation, the following simple expression can be used to calculate the equivalent pore pressure (see e.g. Lewis and Schrefler 1998, NWMO 2011, Fall et al. 2014)

$$P_p = S_l P_l + S_g P_g \tag{B-1}$$

The equivalent pore pressure serves as input to the mechanical analysis, which in the poroelasticity framework takes the form:

$$\boldsymbol{\sigma} = \boldsymbol{\sigma}' - b P_p \mathbf{I} \tag{B-2}$$

where $\boldsymbol{\sigma}'$ (MPa) is the effective stress tensor, $\boldsymbol{\sigma}$ (MPa) is the total stress tensor, b (-) is the Biot's coefficient, and $\mathbf{I}$ (-) is the second order identity tensor. The above equation is based on the convention of tensile stresses being positive in the stress tensor. The Biot's coefficient ($0 < b < 1$) is introduced to account for the different values of bulk modulus for solid phase (grain) and the skeleton, K_s (MPa) and K_T (MPa), respectively (e.g. Schrefler et al. 1989)

$$b = 1 - \frac{K_T}{K_S} \tag{B-3}$$

This coefficient quantifies the degree of coupling between changes in pore pressure and mechanical deformations. For soil-like (soft) materials, this coefficient is usually equal 1.0, which maximizes the level of coupling. Typical values for concrete are close to 0.5 (Ulm et al. 2004, Cuomo and Nicolosi 2006), although several authors indicate that this value is probably much lower, between 0.15 and 0.35 (Bary et al. 2000, Gawin et al. 2006). In the present setup, a Biot's coefficient of 0.5 is used for both the concrete structures (backfill and waste) and the host-rock. All other linear elastic parameters are identical to those considered in Idiart et al. (2019).

The model developed in this appendix is based on two existing models:

- The multiphase flow model presented in this report, corresponding to Case 14, in which vertical downwards gas flow is induced and gas pressures are the largest (see Sub-Section 4.1.3).
- the hydro-chemo-mechanical model of the BHK vault presented by Idiart et al. (2019).

Only the mechanical model of the base case presented by Idiart et al. (2019) is retained here. No chemical degradation of the concrete barrier is considered, while the flow field is input from the multiphase flow model. Moreover, no mechanical damage model is considered in the simulation. Instead, linear poroelasticity is assumed. Because of the one-way coupling approach, the deformations from the mechanical model do not impact the multiphase flow analysis. The results obtained with this hydro-mechanical model should therefore be regarded as a first approximation of the effect of gas pressure on the mechanical stability of the BHK vault.

The pore overpressure (ΔP_p), defined as the temporal change in the equivalent pore pressure with respect to the initial conditions, is calculated as

$$\Delta P_p = P_p(t) - P_l(0) \tag{B-4}$$

The details of the mechanical setup of the model can be found in Idiart et al. (2019). The geometry and boundary conditions (in-situ stresses) are shown in Figure B-1. Depth dependent horizontal in-situ stresses at Laxemar as estimated by Hakami et al. (2008) are imposed at the left and right boundaries Also, a vertical stress corresponding to repository depth is imposed on the top boundary. The bottom-left vertex is fixed (zero displacements), while a roller boundary condition is imposed on the bottom boundary (zero vertical displacements). The active loads in the model include the in-situ stresses, the self-weight of the structure, and the pore pressure.

Figure B-2 shows the gas saturation and pressure distributions obtained after 10 000 years. This time is chosen because during this period the gas pressures are at their maximum. As can be observed, although the maximum gas pressure reached within the backfill is about 6.26 MPa, the gas saturation does not exceed 3.5 %. As a result, the equivalent pore pressure (Equation B-1) is very similar to the initial water pressure in the entire domain. This is also shown in Figure B-3, which presents the pore overpressure distribution after 10 000 years calculated according to Equation B-4. The simulated pore overpressures represent changes below 1 % of the initial water pressure field.

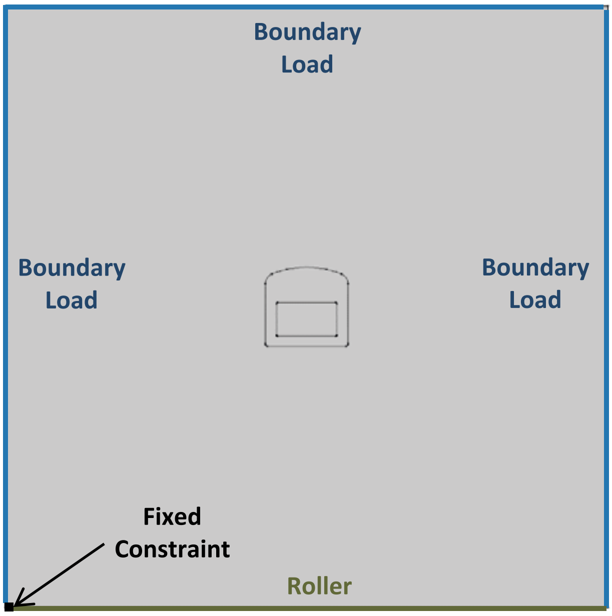

Figure B-1. *Boundary conditions considered in the mechanical analysis.*

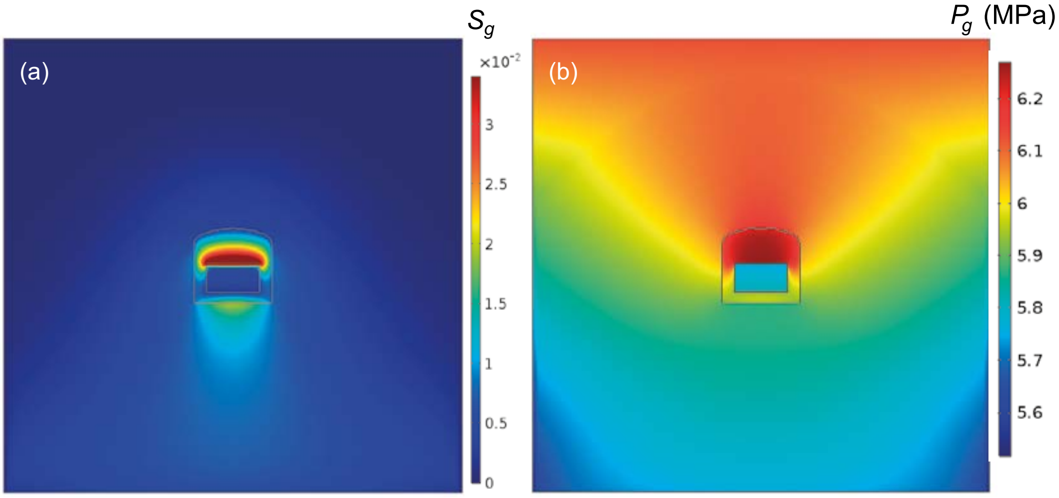

Figure B-2. *Gas (a) saturation and (b) pressure distributions obtained at 10 000 years for high vertical downwards groundwater flow (Case 14).*

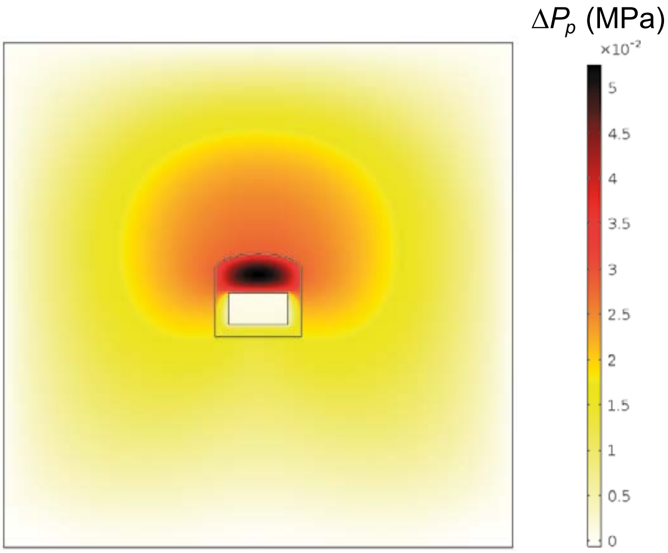

Figure B-3. *Pore overpressure obtained at 10 000 years for high vertical downwards groundwater flow (Case 14).*

Due to the small pore overpressures, the impact of gas generation on the mechanical behaviour of the system is not significant. Figure B-4 and Figure B-5 show the effect of pore overpressures on the stresses and displacements, respectively. The initial first principal stress (σ_1^0) field, which in COMSOL corresponds to the least compressive stress (positive values for tensile stresses) is shown in Figure B-4a. The corresponding difference with respect to the initial condition ($\Delta\sigma_1 = \sigma_1 - \sigma_1^0$), induced by gas generation and migration after 10 000 years, is shown in Figure B-4b. As can be observed, the differences are lower than 0.025 MPa. Positive values of the difference represent a decrease of the compressive stresses. In other words, gas generation causes a reduction of the compressive stresses and an increase of the tensile stresses acting on the solid structure. The difference between the first principal stress and its initial value appears too small to affect the mechanical stability of the BHK vault. Figure B-5a shows the ratio between σ_1 obtained after 10 000 years and σ_1^0. It can be observed that differences in the stress field after 10 000 years with respect to the initial state are smaller than ~3 %, except at two points where this difference is 9 %.

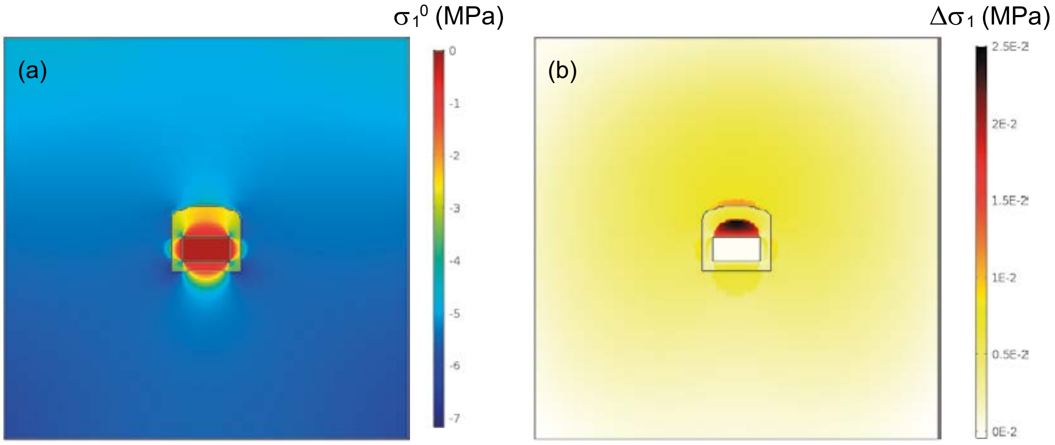

Figure B-4. *Results of poromechanical simulation: (a) initial distribution of first principal stress (σ_1^0) and (b) corresponding difference with respect to the initial condition after 10 000 years.*

The above is upheld by the displacements evolution displayed by the system. Figure B-5b shows the difference ($\Delta u = u - u^0$) between the total displacement field (u) obtained at 10 000 years and the initial displacements field (u^0). The differences are in the order of few microns. Negative values in the top right of the model domain represent a situation where the pore overpressure induces a decompression of the rock.

From this preliminary study, it may be concluded that the effect of gas generation on the mechanical behaviour of the BHK vault is negligible. This is a consequence of the small gas saturations predicted by the model, which lead to an equivalent pore pressure that is very similar to the initial liquid pressure.

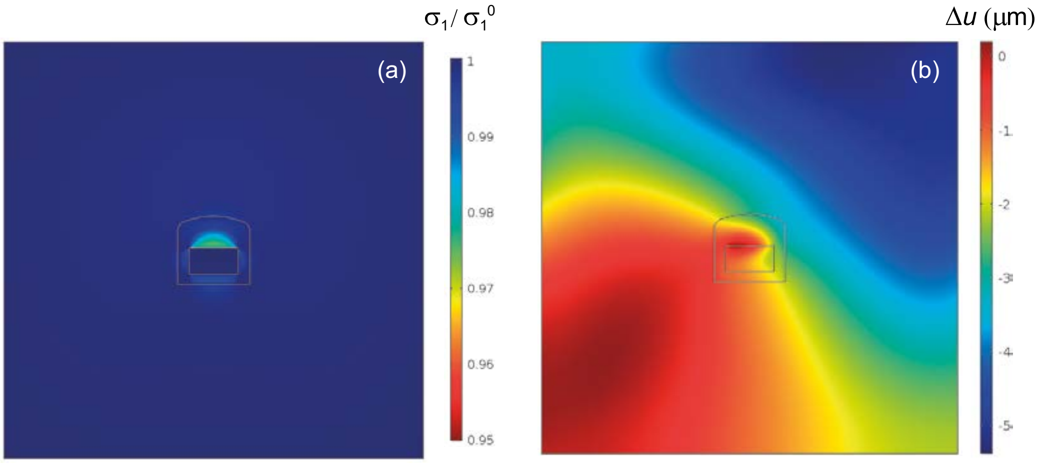

Figure B-5. *Results of poromechanical simulation: (a) ratio between first principal stresses after 10 000 years and their initial distribution (σ_1/σ_1^0), (b) distribution of the difference between the total displacement field obtained after 10 000 years and the initial displacements field.*